KOBELCO TECHNOLOGY REVIEW

No. 31 JAN. 2013

Feature-I : Excavators & Cranes
Feature-II : Aluminum and Copper Technology

Contents

Feature-I Excavators & Cranes

Feature-II Aluminum and Copper Technology

A Multi-purpose Demolition Machine with Interchangeable Attachments

Koichiro NIWATA

Special Equipment Department, Global Engineering Center (GEC), KOBELCO CONSTRUCTION MACHINERY CO., LTD.

A hydraulic excavator operates various actuators and uses them not only for digging, but also for various other jobs. Demolition of buildings is a typical application of an excavator. A variety of attachments have been developed for a wide working range from high to middle elevations as well as for foundations. Conventionally, however, it has been necessary to have an excavator for each specific attachment, and the users had to cover all costs to keep various excavators with different attachments. To solve such a problem, we have developed a series of multi-purpose demolition machines. Each machine has a main boom on which different kinds of attachments can be installed. This article includes descriptions and illustrations explaining the usefulness of the multi-purpose excavators that have been developed.

Introduction

Recent demolition sites in urban areas are more restricted in their passageways and spaces, which often causes difficulties in using large machines, or an increased number of machines, to shorten construction periods. Demolition jobs are conducted in various ways: some are conducted from the ground level and others from the rooftops of buildings. In the case of roof-mounted demolition, it may be difficult to bring in a large crane. In such a case, the limited lifting capacity allows only the use of smaller demolition machines. Thus, the work environment for demolition has become increasingly restricted.

On the other hand, an increasing number of demolition contractors are using rental equipment. Demolition machines are made with a variety of specifications. Owning various machines of different classes not only increases the need for parking space, but also leads to less utilization of the machines, decreasing the return on investment and causing a burden.

To solve these problems, we have developed multi-purpose demolition machines, as outlined in this paper.

1. Aims and features of multi-purpose demolition machines

KOBELCO CONSTRUCTION MACHINERY CO., LTD. has a line-up of demolition machines, including multi-purpose machines with special specifications (**Fig. 1**). A multi-purpose machine comprises a main body and a main boom attached to it; the main boom is adapted to receive several kinds of attachments. **Fig. 2** is a conceptual diagram. The main boom has two pin-joints near its tip, which allows the mounting and dismounting of an attachment such as a separate boom and extra-long attachment. This multi-purpose demolition machine has one base machine and performs various tasks, which not only increases its utilization, but also decreases the initial purchase cost, as well as parking space and maintenance costs. Originally, multi-purpose machines were built mainly as large machines; however, the demand for smaller products has increased. Now, the multi-purpose concept has been extended to smaller machines, including small to mid-sized hydraulic excavators of the 13 to 26 tonne classes.

Fig. 1 Base machine of SK235SR

Ultra long attachment   Separate boom   Backhoe
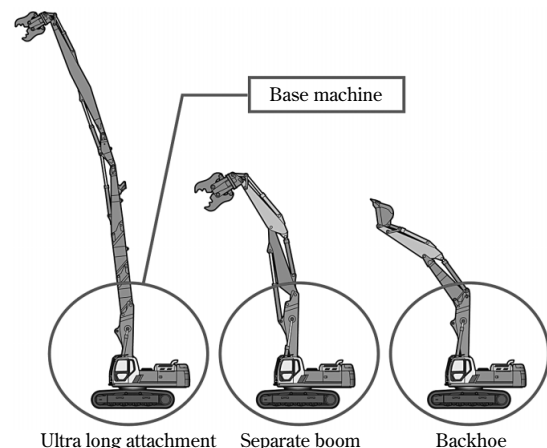
Fig. 2 Concept of machine with common use type main boom

2. Outline of attachments and their uses

The following describes two types of attachments, a short separate boom and an ultra-long attachment, both designed for a series of machines, from the SK135SR to the SK260DLC, which is introduced in this paper.

2.1 Separate boom

A separate boom has a jib cylinder at its mid-portion, which allows the boom to be bent and almost doubles the operating range compared with a conventional hydraulic excavator. The jib cylinder significantly increases the lifting capacity and enables the arm tip to be moved near the front edge of the crawler. This improves the efficiency of demolition work done near the crawlers. The separate boom secures the working range required for demolition work on lower stories and the foundation of a building. The attachments that can be interchangeably mounted at the boom tip include a crasher, breaker, rotary fork and bucket, enabling a variety of work. Also provided is a backhoe attachment for excavation application. The backhoe has the same shape as the one used for a general purpose hydraulic excavator. **Fig. 3** compares the operation range of the SK200DLC machine, which has a separate boom, with one having a conventional backhoe. **Fig. 4** shows the appearance of the SK260DLC with a separate boom.

2.2 Ultra-long attachments folded in two and three pieces

There are two specifications for ultra-long attachments; one is a two-piece type and the other is a three-piece type. The two-piece type is an ultra-long attachment with one joint in the arm. This attachment is light in mass and can easily be used in the same operating pattern as a backhoe. **Fig. 5**

shows a SK235SRDLC with a two-piece ultra-long attachment. The machine has a maximum working height of 13.68m and can demolish buildings up to four stories high.

The other type, a three-piece ultra-long attachment, is capable of extending the working range by actuating the inter boom at the mid portion. The SK260DLC, shown in **Fig. 6**, has a maximum working height of 16.5m and can be used for demolishing jobs up to five stories high.

Fig. 4 Separate boom machine of SK260DLC

Fig. 5 2 piece ultra long machine of SK235SRDLC

Fig. 3 Operation range comparison of SK200DLC
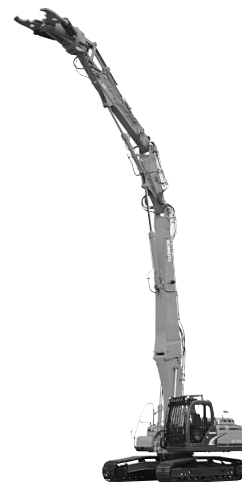
Fig. 6 3 piece ultra long machine of SK260DLC

3. General configurations

Fig. 7 shows the general configurations of the machines with main booms. The SK135SRDLC and SK235SRDLC are designed with a base machine having small rear swing and can work in narrow places without the necessity of paying undue attention to the rear. The largest machine of the series, the SK260DLC, with its main boom installed, but without an attachment, has a total length of 6.27m and a mass of 24.3 tonnes. This has enabled its transportation on a general purpose trailer.

SK135SRDLC

SK210DLC

SK235SRDLC
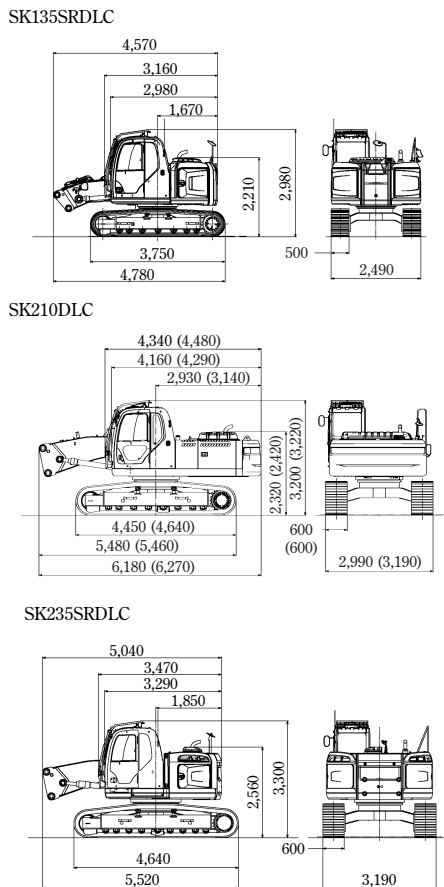
Fig. 7 General configuration

4. Attachment line-up

Table 1 summarizes the attachments designed for each model. A multi-purpose demolition machine can be used with more than one attachment, which adds value to the machine. The newly designed attachments are used with models of different classes and performance, and work at various demolition sites where buildings and foundations are demolished and debris is carried. **Fig. 8** shows an example of attachment combinations for the SK235SRDLC.

When developing the new models, attachments

Table 1 Attachment line up for each model

	SK135SR	SK235SR	SK210DLC	SK260DLC
Back hoe	○			
Separate	○	○	○	○
2 piece ultra long	○	○	○	○
3 piece ultra long		○	○	○
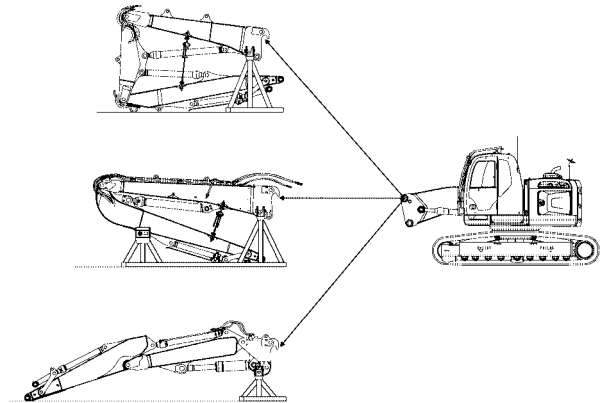
Fig. 8 Variation of attachment
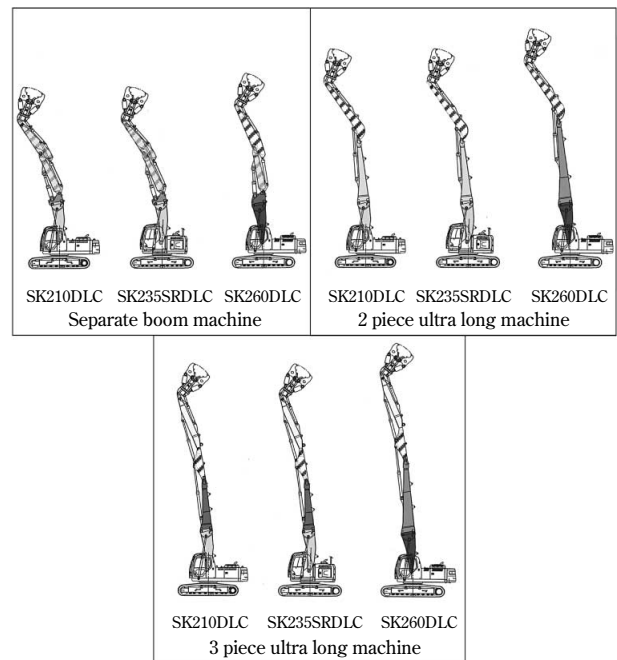
Fig. 9 Combination of attachment parts

are designed to be shared by more than one machine, which has significantly increased development efficiency. More specifically, the attachments for three models, the SK210DLC, SK235SRDLC and SK260DLC, all based on a medium-sized hydraulic excavator, use the same parts as shown in **Fig. 9**. In this figure, the parts of a pattern are interchangeable. The interchangeability of parts permitted by the new

development has evolved 9 variations (3 models, 3 specifications) and has added 4 variations to the product line.

5. Mounting and dismounting of attachments

To improve work efficiency at demolition sites, different attachments must be used interchangeably. When mounting an attachment, the hooks on the front boom are engaged on the positioning bars on the tip of the main boom. This facilitates the positioning of the connection pin-holes located at 2 positions, top and bottom, at the tip of the main boom (**Fig.10**). More specifically, the main body is driven close to the attachment, and the boom cylinder on the main boom is raised to engage the positioning bar with the hook. The attachment is turned around the hook until the positions of the two pin-holes align.

A conventional separate boom has a number of parts, such as pins and hydraulic cylinder hoses, which must be mounted or dismounted, making the work of mounting and dismounting time-consuming. The multi-purpose demolition machine developed this time comprises a structure called a "main boom front", having connecting portions for cylinders. This structure is placed between the main boom and front boom such that the structure and the front boom can be disassembled as a unit (**Fig.11**), which has significantly facilitated the mounting and dismounting of the separate boom.

A setting stand (**Fig.12**) enables mounting and dismounting without using a crane and ensures safety. Stop valves are provided at pipe joints to minimize the spillage of hydraulic oil when connecting or disconnecting pipes.

Fig.12 Setting stand of attachment

6. Safety apparatus

Each machine is well considered to ensure safety during demolition work. The machine with an ultra-long attachment is equipped with a warning apparatus that notifies the operator of the risk of turning over. The apparatus includes angle sensors placed at the joints of each attachment and triggers a buzzer when stability drops to a predetermined level. To prevent the window glass from being broken by falling objects and debris, the cab is protected by grating guards on three faces (**Fig.13**). In addition, an apparatus is provided for preventing an attachment from interfering with the cab, in consideration of the possibility that, in certain positions, an attachment at the boom tip may interfere with the cab. This safety apparatus, provided as a standard feature, triggers a buzzer when a crusher at the tip of the arm enters the region less than one meter from the front edge of the cab. **Fig.14** shows the concept of the cab interference prevention apparatus. Other safety features include a fall prevention valve for the boom, rearview camera and travel alarms.

Fig.10 Procedure of attachment assembly
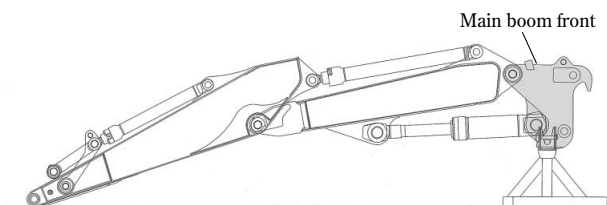
Fig.11 Main boom front

Fig.13 Appearance of demolition cabin
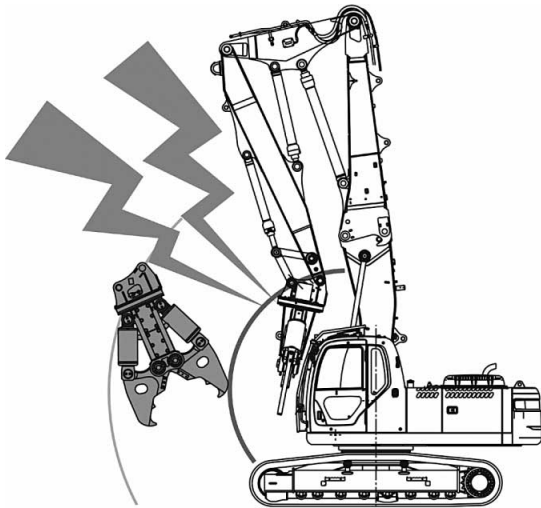
Fig.14 Cab interference prevention system

Fig.16 SK235SRDLC 2 piece ultra long attachment machine
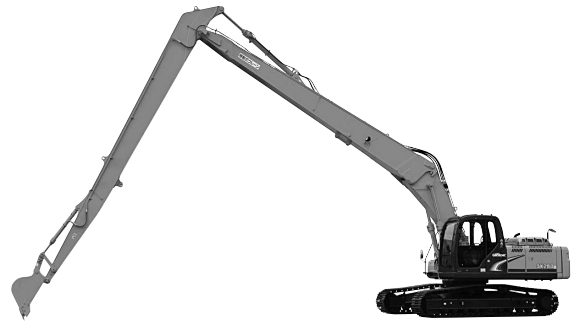
Fig.17 SK260LC separated type long reach machine

Fig.18 SK260LC long reach in separation

7. Application examples

The multi-purpose demolition machines introduced in this paper have been commercialized and are being widely used at actual demolition sites. **Fig.15** shows a SK135SRDLC separate boom machine working at a demolition site. **Fig.16** shows a SK235SRDLC with a two-piece ultra-long attachment.

These machines, designed for multi-purpose demolition, have an increasing number of variations in order to respond to the requirements of transportability and workability in addition to their demolition performance. The following are some examples of their applications.

A long reach attachment machine, having an attachment with extended length, is characterized by its wide working range and is used not only for demolition, but also for the dredging of rivers and field maintenance. Such a machine, however, has a disadvantage in its transportability. The SK260LC separate-type long reach machine (**Fig.17**) is based

on the separate boom of the multi-purpose demolition machines and has significantly improved transportability. **Fig.18** shows the machine after the attachment has been separated from it.

Conclusions

Hydraulic excavators are primarily characterized by their ability to work with a number of actuators and they have the advantage of being able to use a variety of attachments. The multi-purpose demolition machines have mechanisms to further exploit such advantages. The machines are currently used mainly for construction work involving demolition, and their application range is expected to grow in the future.

Fig.15 SK135SRDLC separate boom attachment machine

The Development of an 8 tonne Class Hybrid Hydraulic Excavator SK80H

Masayuki KAGOSHIMA

System & Component Development Department, Global Engineering Center (GEC), KOBELCO CONSTRUCTION MACHINERY CO., LTD.

There is an increasing demand for construction machines with lower fuel consumption to prevent global warming and to decrease the operational cost. In response to such demand, we have developed a hybrid system for an excavator of the 8 tonne class. The system employs advanced power electronic components, such as an electric motor, inverter and battery. These components are similar to the ones that have been used for hybrid cars, but are more sophisticated in that they are designed for an increased number of actions performed by an excavator. When installed in an SK80H model, the system has reduced its fuel consumption by 40% or more and also decreased the noise level significantly.

Introduction

With the growing concerns about global warming caused by greenhouse gas emissions, energy-saving technology is receiving increased attention. In the automotive industry, the improved performance of motors, advanced power electronics (e.g., inverters) and improved battery technologies (e.g., NiMH/Li ion batteries) have led to the commercialization of hybrid systems. Furthermore, all-electric vehicles are being put into use[1), 2)].

Since 1999, KOBELCO CONSTRUCTION MACHINERY CO., LTD. has collaborated with the New Energy and Industrial Technology Development Organization (NEDO) and Kobe Steel, Ltd. in R&D activities on a hydraulic excavator adapting a series hybrid system. The resulting technology was used to develop a system that is more practical and commercially feasible. This paper reports on a hybrid excavator, the SK80H, which was developed for mass production.

1. The purpose of hybrid excavators

1.1 The construction of a hydraulic excavator and the use of power

A hydraulic excavator comprises several actuators, such as the cylinders that actuate the boom, arm and bucket, and motors that are used for swinging and traveling. These actuators are driven by a hydraulic pump to perform tasks such as digging (**Fig. 1**). **Fig. 2** shows the change in the input power of the hydraulic pump and the change in the power consumed by the actuators during the cycle of an excavation task performed by a conventional hydraulic excavator of the 8 tonne class. As shown in this figure, the hydraulic pump in a conventional hydraulic excavator supplies the power required for the maximum load all the time, even when the power consumed by the actuators is low. The surplus power is dissipated as heat. The dissipated heat also includes heat caused by operational loss that is intentionally incorporated to improve the maneuvering feel of each operation. Also included in the dissipated heat are potential / kinetic energies consumed by lowering, swinging and stopping the working apparatuses. **Fig. 3** shows the flow of power
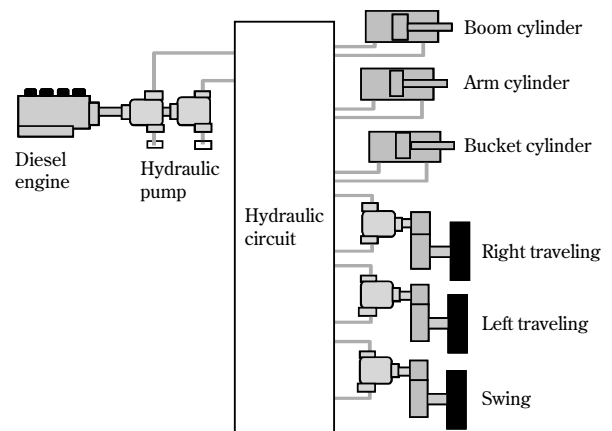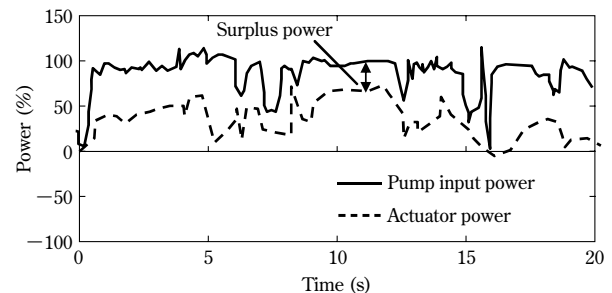

Fig. 1 Block diagram of hydraulic excavator
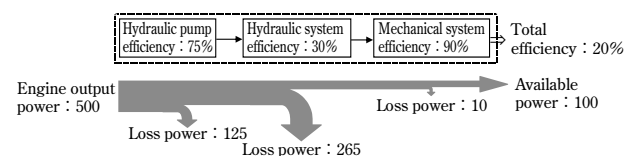

Fig. 2 Excavator power

Fig. 3 Power flow

in the hydraulic excavator. The figure also shows the efficiency of each subsystem and a power flow diagram assuming the engine power to be 500. On the average, only 20% of engine output power is exploited in a conventional hydraulic excavator.

In the field of automobiles, hybrid systems have been developed and brought into practical use for hybrid cars. These automobiles focus on the reuse of regenerative energy and on the improvement of system efficiency during the partial load operation of their engines. A hydraulic excavator, on the other hand, has a greater number of actuators to be controlled than an automobile has, and the actuators are subject to large resistance such as the reactive force of digging. In addition, the actuators are subject to large load variation, because they are repeatedly, and in a short period of time, used for high-load tasks, such as heavy digging, and low-load tasks, such as horizontal towing and leveling. **Table 1** compares a hybrid system for a hydraulic excavator with that of an automobile. A hybrid system for an automobile cannot be adopted as-is to a hydraulic excavator that is subject to large load variation. There is a need for a newly-developed system for hydraulic excavators.

Table 1 Comparison of automobile and hydraulic excavator

	Automobile	Hydraulic excavator
Application	Running	Digging, Leveling, Loading
Operation	Handle, Pedal	Lever (multiaxial)
Number of actuator	1	6
Type of Load	Running resistance	Excavation reaction force
	Inertial force	Inertial force
Load fluctuation	small	big
Velocity fluctuation	small	big

1.2 Points for fuel saving

Having in mind the facts mentioned in the above discussion, we focused on the following three points in the development of a hybrid system for a hydraulic excavator.

1) Electrically-driven swing

Making the swing motion electrically driven has made regenerative power available for reuse, significantly reducing the loss caused by the hydraulic drive. The electrical drive permits the swing motion to be driven independently from other actuators such as the boom. This has decreased the distribution loss that would otherwise have been generated during compound control actions, such as the simultaneous operation of boom raising and swinging.

2) Loss reduction in hydraulic system

The hybrid system alone cannot sufficiently improve the fuel efficiency. The efficiency of the hydraulic system must also be improved. We have significantly reduced the hydraulic loss by performing a thorough review of flow resistances in hydraulic devices, such as pumps and valves, and piping. The review included design revisions and the replacement of parts.

3) Leveling of engine load

Fig. 4 shows the changes in the engine power of a hybrid excavator during its major operations (i.e., digging, boom raising/swinging, dumping and boom lowering/swinging). Also included for comparison in this figure are the power changes of a conventional excavator. As shown in this figure, the hybrid excavator converts the surplus energy from low-load operations into electricity and stores it in a battery. The power stored in the battery is used to drive an electric motor during high-load operations to positively assist the engine. This arrangement allows
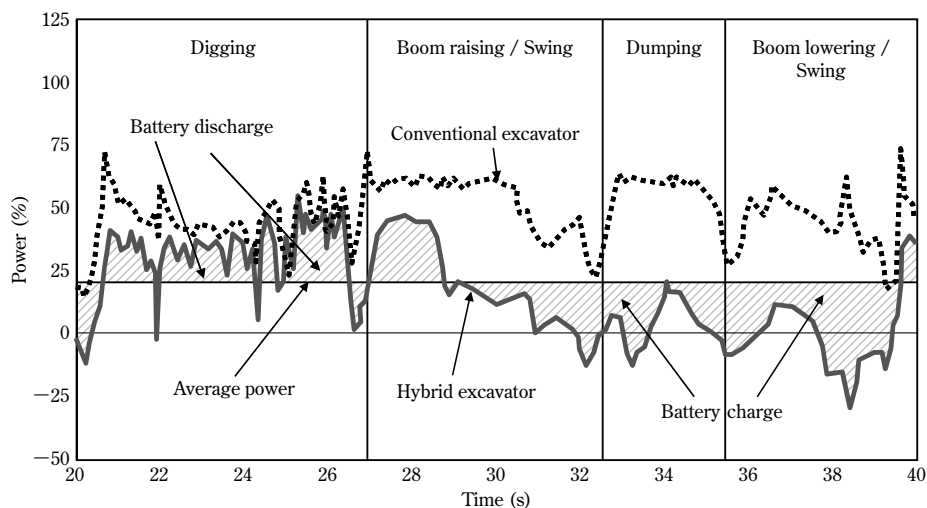
Fig. 4 Leveling of engine load

the leveling out of the engine load, enabling the downsizing of the engine and operation at high-efficiency.

2. Hybrid excavator

2.1 The system configuration

Fig. 5 is a block diagram of a hybrid system developed by KOBELCO CONSTRUCTION MACHINERY CO., LTD. This system, designed for an 8 tonne class excavator, is a series-parallel hybrid system in which the hydraulic circuits for the boom and the like are driven in parallel and the swing motion is driven in series. This system configuration was selected from among various hybrid systems that were considered. The selection was based on the desire to obtain the highest rate of efficiency at a lower cost, i.e., considering the rate of the fuel-saving effect vs. the calculated cost increase incurred by hybrid apparatuses such as motors. A conventional excavator has an engine that drives a pump to distribute hydraulic pressure to its actuators. The present system drives its pump using power from both the engine and generator-motor.

The control system includes several controllers, such as a hybrid controller, generator-motor controller, engine controller and battery monitor, for cooperative control (Fig. 5). Compared with conventional excavators, hybrid excavators are exposed to an environment with more severe noise, including, in particular, inverter noise. Therefore, wiring must be kept as short as possible, especially for the sensors. Because of this, the controllers are built into units along with other devices, and the controller units are connected by high-speed serial lines to achieve the high reliability of the system.

The following explains the function of each controller. Each component (i.e., engine, generator-motor, swing motor and battery) is assigned its own controller. The hybrid controller transmits
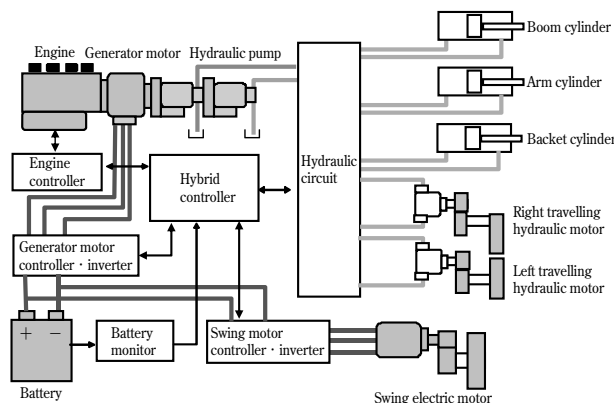
commands to the component controllers. Component failures are detected. Stopping control is executed at the time of any component failure. The hybrid controller receives and manages information (e.g., the status of components, sensing data and errors) from the component controllers and executes the power management control for the entire system. The proper function arrangement for the controllers has enabled the cooperative control of the entire system.

2.2 Hybrid components

The performance of a hybrid system (i.e., system efficiency and power performance) is determined by the way that the power is shared by each component. Thus, the determination of the output power is most important in the component specifications. In the present development, the power required for each component is determined by calculation, as well as simulation based on the results of the power actually measured on conventional excavators. The following outlines the major components listed in **Table 2**.

1) Engine

The downsizing of engines is effective in improving fuel efficiency. Conventional machines require engines of about 40kW, while the present system employs a smaller engine of 27kW. With power assistance from the generator-motor, the system has achieved a working speed and power just as high as those of the conventional systems.

2) Battery

A hybrid system requires a battery with high power density. A nickel hydrogen battery has been adapted for use in this system; it is the same type as that used for automobiles. Its capacity was determined such that its discharge power meets the output requirement for an 8 tonne class excavator with engine assist. The charging capacity is determined on the basis of the maximum regenerative power of the electric swing motor.

3) Generator-motor

Being coupled with the engine, the generator-motor must be small and possess high efficiency; hence, a permanent magnet motor has been adapted for use. This motor is flat in shape and is built in between the engine and pump. Its output was determined such that its power, including assist

Fig. 5 Block diagram of hybrid excavator

Table 2 Equipment specifications

Engine	Rated power 27(kW)/1,800(min^{-1})
Generator motor	Rated power 10(kW)/1,800(min^{-1})
Swing electric motor	Rated power 8(kW)/1,890(min^{-1})
Battery	Rated voltage (288V)

power, would be at the same level as that of a conventional excavator.

4) Electric swing motor

A permanent magnet motor with high efficiency was adapted for the electric swing motor. The motor, combined with the inverter control, enables the regeneration of energy during the deceleration of swing motion. The output is determined such that the swing motion acceleration is achieved at the same level as that of conventional excavators.

5) Inverter

The inverter adopted was one integrated for both the generator-motor and electric swing motor. The inverter output was determined from the capacity required for driving all the electric motors, considering their maximum loads.

2.3 Hybrid excavator motions

Compared with an automobile, an excavator has a greater number of actuators and performs more motions. Thus, it is important to select the power sources, such as the engine and battery, according to these motions. **Fig. 6** shows the operation of the

Fig. 6 Operation of hybrid excavator

major components according to the motions of the hybrid excavator.

1) Unloaded (Fig. 6, ①)

When the excavator is unloaded and the battery charge is below a predetermined level, the engine drives the generator to charge the battery. Thus, the battery charge is maintained at the level required for power assist, making the excavator ready for high-load operation.

2) Heavy digging (without swing motion; Fig. 6, ②)

During heavy digging, the engine drives the pump with assistance from the generator-motor driven by battery power. The use of the battery power allows the small engine to achieve the same level of power performance as that achieved by conventional machines.

3) Boom raising/swing (heavy digging and swinging; Fig. 6, ③)

During heavy digging involving swing motions, the engine drives the hydraulic pump, while the battery powers the electric swing motor. The coordinated action of the engine and motor provides the power required for the compound motions of the hydraulic system and the swinging.

4) Swing braking (Fig. 6, ④)

When the swing motion is decelerated, the regenerative power of the swing motion is charged into the battery. At the same time, the power generated by the generator-motor that is driven by the engine is also charged into the battery. This enables the reuse of the regenerative energy of the swing motion, energy that is conventionally dissipated as heat.

5) Boom lowering and swinging (light load swinging; Fig. 6, ⑤)

During hydraulic driving, the surplus power from the engine is used to generate electricity; that power is used to drive the electric swing motor and is also charged into the battery. This enables the leveling of the engine load and improves the system efficiency.

3. Effect of hybridization

3.1 Hybrid power source control

A hybrid system comprises various components such as an engine, battery and electric motor. Thus, it is important to control the power supplied to each of these components according to the load imposed on each actuator. **Fig. 7** shows the result of a test conducted on the power source control of an actual machine. In the figure, numbers ② to ⑤ correspond, respectively, to the motions ② to ⑤ depicted in Fig. 6. Numbers ② and ③ are cases with a relatively
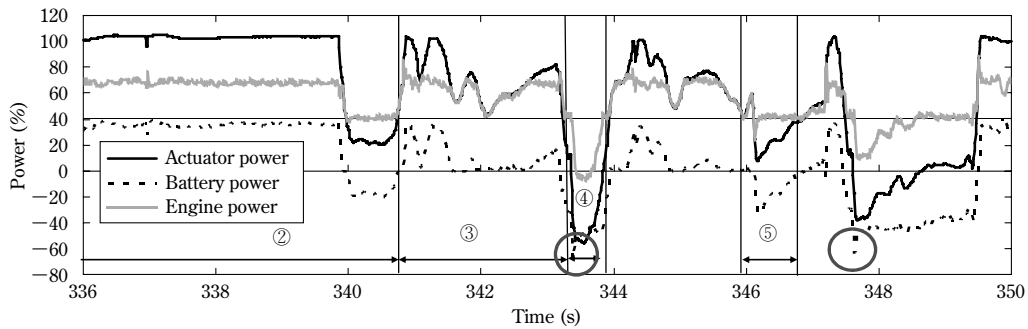
Fig. 7 Results of power control test

heavy load, in which the battery-driven generator-motor provides power assist when the total power consumed by the actuators exceeds the power supplied by the engine. Number ④ represents a case in which the swing motion is decelerated, during which action the regenerative power from the electric swing motor is stored in the battery. Number ⑤ represents a case in which the boom is lowered with a swing motion; engine power is being used to drive the swing motion and, at the same time, is being stored in the battery. As shown, almost all the motions depicted in Fig. 6 are realized. In the battery control, the maximum powers for the battery charging and discharging are determined by the battery SOC (State of Charge) and battery temperature. For the motions shown in Fig. 7, the maximum charging power and maximum discharging power are set at 46% and 48%, respectively. The battery power varies greatly, and, in a transient state, may exceed the maximum power of charging and discharging (as shown by circles in Fig. 7). Except for these portions, the power is controlled so as to remain within the maximum amount of power for charging and discharging, showing that the hybrid power source control is functioning as intended.

3.2 Fuel consumption reduction effect

The fuel efficiency evaluation of hybrid hydraulic excavators has been newly established in the Japan Construction Machinery and Construction Association Standard (JCMAS)[3]. The test method covers a comprehensive evaluation of motions, including digging & loading, leveling, traveling and idling. The fuel efficiency of the SK80H was evaluated on the basis of this standard.

Fig. 8 shows the results of the fuel efficiency measurement based on the new JCMAS. The fuel consumption for each task is compared to that of the conventional machine produced by KOBELCO CONSTRUCTION MACHINERY CO., LTD. In this figure, the data for the conventional machine is assumed to be 100 percent. For digging and loading
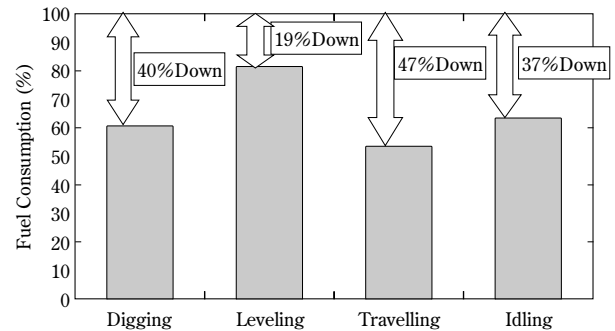
Fig. 8 Improving of fuel consumption

tasks, an almost 40% reduction in fuel consumption has been achieved. The data also confirms that a maximum reduction of 40% has been realized for CO_2 emissions.

3.3 Noise reduction effect

Silence is another important feature for excavators of the 8 tonne class, since they are used for construction work in urban areas. A hybrid excavator, the SK80H, was measured for its noise reduction effect. When compared to a conventional excavator of the same class, the hybrid excavator emits less noise, thanks mainly to the noise reduction effect of its downsized engine. Although, in comparison with conventional machines, it lacks any special noise reduction measures, the SK80H emits 90 dB(A), a significant noise reduction about 3 dB(A) lower than the standard value. The machine is officially designated as ultra-low-noise construction equipment under Japanese Ministry of Land, Infrastructure, and Transport noise regulations. The hybrid system has been proven to provide an effective means for noise reduction.

Conclusions

The SK80H, developed as an 8 tonne class hydraulic excavator, has been introduced as an example of volume production machinery designed as energy-saving construction equipment. The

hybrid system has enabled the downsizing of the engine, improved the fuel efficiency by 40% and achieved a significant noise reduction. We will continue to strive to further improve our product on the basis of field information, such as actual operational data, and also to reduce the cost and increase productivity, while maintaining the above-described fuel efficiency performance.

References

1) K. Kondo. *Development of Electrical 4WD System for Hybrid Vehicles. 2001 JASE Convention Proceedings.* No.101-01, p.13-16.
2) M. Sakaki et al. *Development of Capacitor Hybrid System for Urban Buses. 2001 JASE Convention Proceedings*. 2001, No.102-01, p.9-14.
3) *Japan Construction Mechanization Association. Earth-moving machinery- Test methods for energy consumption- Hydraulic excavators.* JCMAS H020 : 2010.

Ultra-low Noise Hydraulic Excavators Using a Newly-developed Cooling System (iNDr)

Hajime NAKASHIMA[*1], Kazuhiro UEDA[*1], Tomoyuki TSUCHIHASHI[*1], Yasumasa KIMURA[*2], Zenzo YAMAGUCHI[*2]

[*1] Power Plant Engineering Group, Hydraulic Excavator Engineering Department, Global Engineering Center (GEC), KOBELCO CONSTRUCTION MACHINERY CO., LTD.
[*2] Mechanical Engineering Research Laboratory, Technical Development Group

Reducing noise from construction machinery is important in creating a comfortable environment for residents near construction sites and for operators and workers. This is particularly so because an increasing amount of construction is being carried out in urban areas and at night. This article describes a newly-developed ultra-quiet hydraulic excavator that incorporates a patent-pending integrated Noise and Dust reduction (iNDr) cooling system. This excavator has achieved a sound power level that is 5dB lower than the most stringent restriction level set by the Japanese Ministry of Land, Infrastructure, Transport and Tourism. The excavator has been launched as one of our general-purpose models.

Introduction

Lately, there has been a more urgent call for the noise reduction of construction machinery because an increasing number of construction projects are being carried out at night in urban areas, and the environment must be improved for residents near construction sites and for operators. Noise reduction has become an important issue for the manufacturers of construction machinery.

Accordingly, regulations for noise abatement are issued and tightened every year. In Japan, the Ministry of Land, Infrastructure, Transport and Tourism established a type designation system for low noise construction machinery and set the criteria for low noise and super-low noise construction machines. The super-low noise level is even 6dB lower than the low noise level. In Europe, the distribution of machines that emit noise exceeding the EU noise regulation value is not allowed, and the regulation values are becoming more stringent every year. China is enacting noise regulation this year (2012).

Fig. 1 shows the noise regulation values for hydraulic excavators in Japan and Europe. The noise evaluation is standardized according to the sound power level (PWL), which indicates the total acoustic energy emanating from the sound sources of a machine. Progress has been made in the reduction of machine noise in order to comply with both the Japanese and EU regulations, increasing the number of construction machines designated as the super-low noise type. The trend for lower noise machines is
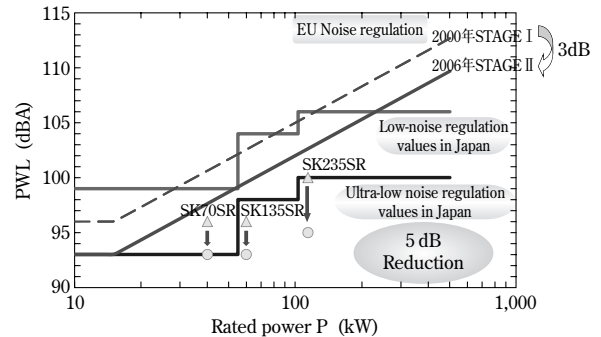
Fig. 1 Noise level of new SR series and noise regulations

expected to escalate.

Another important consideration, in addition to that of noise level reduction, is sound quality. Sound is perceived quite differently by different people, or by the same people at different times and in different situations. The sounds made by construction equipment are a major cause of environmental deterioration perceived by local residents. For the operators of the machines, however, noise can be a source of information that aids in understanding the condition of the equipment. Thus, it is important to consider the creation of an acoustic environment that causes no discomfort to the local residents and enables operators and surrounding workers to work safely and efficiently without undue tiredness.

In this context, we have developed a series of general-purpose hydraulic excavators, the ACERA Geospec SR series, for urban projects. This machine has a noise level that is 5dB lower than that required by the super-low noise standard, the most stringent standard set by the Ministry of Land, Infrastructure, Transport and Tourism. The feature has made the series stand out from the products made by other companies.

There were two approaches taken in the development of the series. One was to reduce the level of the noise, as the level significantly contributes to its obnoxiousness. The other was to pursue a quality of sound that would create less discomfort. The quality of the sound tends to deteriorate with a reduced noise level. This paper introduces the development of the Integrate Noise & Dust Reduction cooling system (hereinafter, "iNDr") as an example of this improvement.

1. Hydraulic excavator sound sources and their features

Fig. 2 depicts the structure of a hydraulic excavator. Also shown are the major sound sources in the excavator. A hydraulic excavator has a diesel engine, which drives a hydraulic pump that sends pressure oil via control valves to actuate hydraulic cylinders and motors. The engine is placed in an enclosure with a fan, hydraulic pump and air cleaner. The enclosure has an opening from which the sound emanates. The term "enclosure", as used herein, refers to the casing enclosing the sound sources.

The major sound sources include the fan, engine, hydraulic devices (e.g., hydraulic pump and control valves), slewing gear and caterpillar treads. The engine emits sounds of mechanical origin, as well as intake and exhaust noise. Construction work itself generates impact and rattling noises. The amount of noise contributed by these factors varies, depending on the size of the excavator and the working conditions. **Fig. 3** shows an example of the sound source contributions of a mid-sized hydraulic excavator at work. The contributions of the five sound sources categorized in the figure were determined by insulating the individual sounds. The inner pie chart shows the contribution in energy ratio of each sound source, while the outer pie chart shows the contributions from the enclosure opening and other sources.
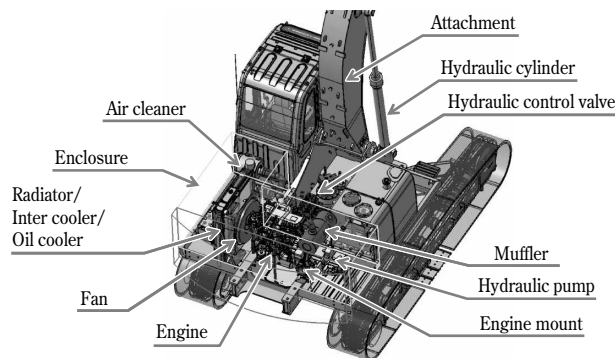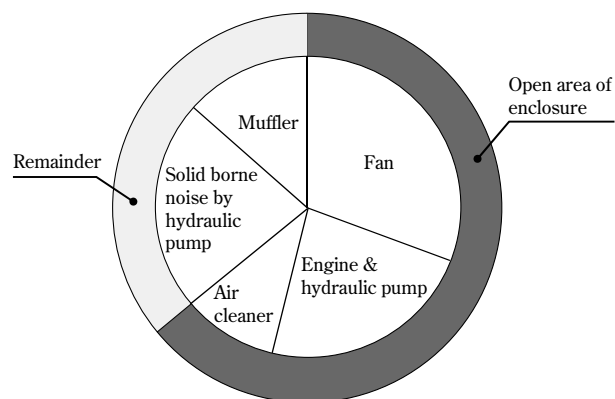
Unlike an automobile, a hydraulic excavator is used for stationary work at high engine load without stream wind. This invariably requires the high rpm rotation of a cooling fan, which makes the fan a significant sound source. During work, the power source becomes subject to a high load, which abruptly increases both the mechanical sound of the engine and the hydraulic sound. This amplifies the level fluctuation and adversely affects the sound quality. Solid-borne sound is caused by pulsations of the hydraulic devices and is propagated and emitted, not from the enclosure, but from other parts such as the frame and any attachment.

The sounds emanating from the engine and hydraulic pump are mostly absorbed or insulated by a lining of acoustic material inside the enclosure, and they partially escape from the opening that serves as a pathway for cooling air. Hence, one of the major design challenges is a choice between mutually exclusive alternatives: i.e., the reduction of the noise escaping from the opening and the securing of ventilation to establish a heat balance.

2. Ultra-low noise and iNDr

2.1 Development goals

Fig. 4 (left) shows the result of a survey on environmental noise pollution, indicating that the complaints about the noise of construction work rank second after those about factory noise.[1] As shown in Fig. 4 (right), most complaints occur in urban areas. This is because urban construction sites are small in area and a number of restrictions on the work arise from the surrounding areas. There is a need for smaller and quieter machines that work safely and show consideration for the environment of the surrounding areas.

After reviewing conventional machines, the following targets were set for improvement.

Fig. 2 Main noise sources of hydraulic excavators

Fig. 3 Ratio of measured sound power of main sources

Complaints by state		
Rank	Complaints	
	Prefecture	Number
1	Tokyo	3,263
2	Osaka	1,756
3	Aichi	1,494
4	Saitama	1,122
5	Kanagawa	1,081
National total		15,849

Fig. 4 Status of environmental noise pollution

① Notable silence
   Environmental protection for the surrounding area：a reduction in the power level to a figure of 5dB below the regulation value
② Reduction of machine-generated noise
   Reduction of noise by 10dB in the vicinity of the cabin, at the point where the noise level reaches its maximum.

Achieving these goals would mean no more need for concern about working at night or near hospitals and would facilitate close communication among workers and ensure safety at work.

2.2 Structure of iNDr

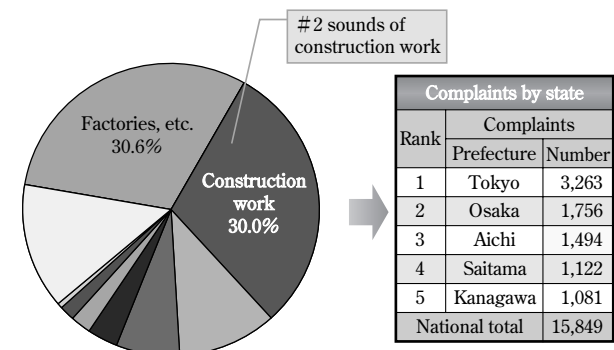As described previously, the enclosure opening makes the largest contribution to the total noise, so the noise from the opening must be reduced.

A system, the Integrated Noise & Dust Reduction Cooling System (iNDr), has been designed to suppress the emission of sound, while securing the flow of cooling air in an enclosure. This has improved the soundproofing performance significantly. The system has also been used to install a dust filter in the duct path, which has significantly improved the ability to clean heat exchangers such as radiators and oil coolers. Their cleaning has been a major issue for conventional construction machines. **Fig. 5** shows the structure of iNDr. **Fig. 6** compares the iNDr system with a conventional structure.

The following are the five points given consideration in designing the system.
① Apertures are closed as much as possible, such that the intake and discharge of air to and from the engine room occurs only at one opening.
② In the conventional structure, sound sources are visible straight from the opening, which limits the soundproofing effect. The newly developed structure includes an opening
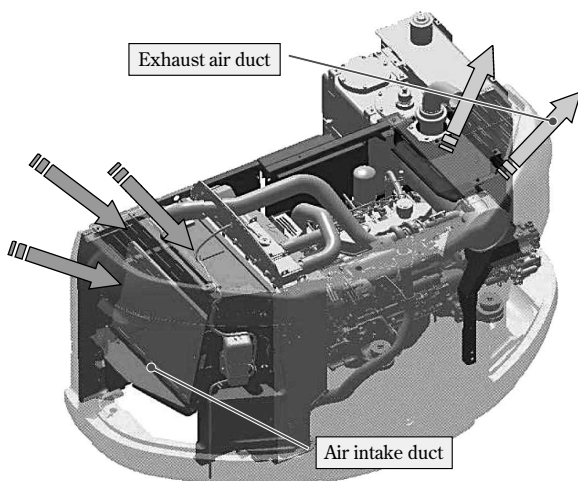
Fig. 5   iNDr structure
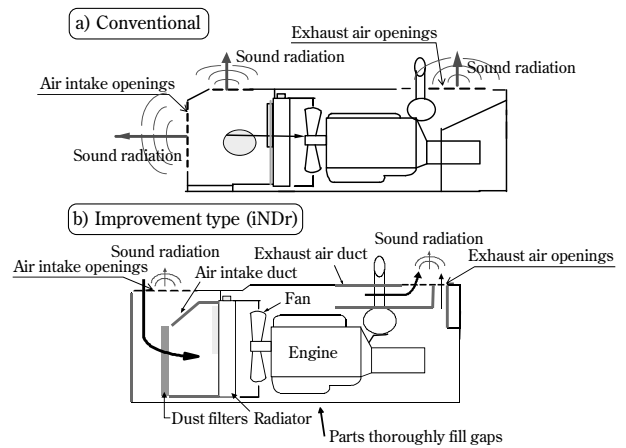
Fig. 6   Comparison of conventional type and improvement type (iNDr)

having the offset structure of a sound absorbent duct, which significantly reduces the radiation of sound.
③ In consideration of the noise and exhaust at the lateral sides of the machine, the opening is located on the top surface.
④ The sound-absorbing performance inside the enclosure is improved by acoustic materials.
⑤ A dust filter is placed in the duct in front of the radiator, such that the filter can be installed and removed easily.

In the inlet duct，there is a trade-off between draft resistance and sound attenuation. Therefore, the off-set between the pathway positions of the opening and cooling fan was optimized by analysis and bench testing.

We have applied for 8 patents, including peripheral patents.

2.3 Analysis and experimental method

2.3.1 Experiment on soundproofing performance of engine enclosure

As previously described, one of the major challenges in the design is the choice between mutually exclusive alternatives: the reduction of the noise escaping from the opening and securing ventilation to establish a heat balance. Thus, the soundproofing structure of the enclosure must be considered. To solve such problems, experiments on actual size machines, as well as numerical simulations, are effective. An easy-to-modify mock-up apparatus was used to improve development efficiency.[2] **Fig. 7** outlines an experimental apparatus simulating the enclosure.

The apparatus has a fan, a major sound source, which is driven by an electric motor substituting for an engine. The engine sound is emitted from an ultra-
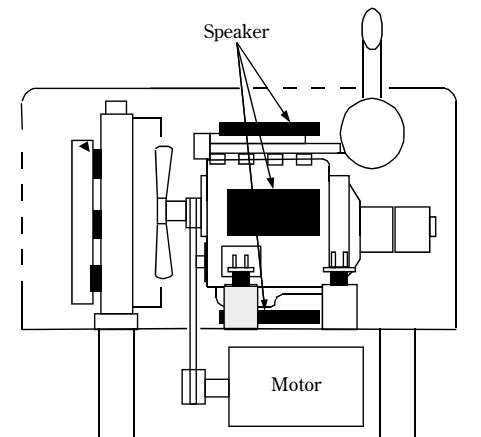
Fig. 7 Experimental apparatus of mock up model
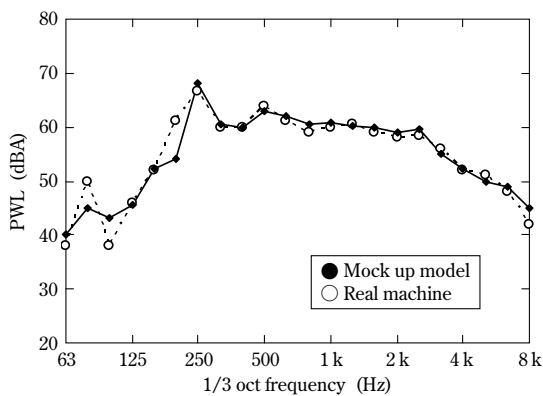
Fig. 8 Comparison of sound power between mock up and real model

thin flat speaker placed adjacent to the electric motor. The sound evaluation is based on the method set by ISO6395 for measuring exterior noise emitted from construction machinery. The evaluation includes the sound power level calculated from the noise measured at 6 points on the face of a hemisphere and the ventilation volume of the heat exchanger (e.g., radiator) measured simultaneously.

Fig. 8 compares the 1/3 octave frequency characteristics of the mock-up apparatus with that of an actual machine. As shown, the characteristics agree reasonably well, verifying the validity of the prediction.

The 1/3 octave band frequency analysis is the most commonly used method for acoustic signal analysis, in which band filters are distributed logarithmically in accordance with the frequency resolution characteristics of the human ear.

### 2.3.2 Estimating cooling air volume by fluid analysis

Analysis techniques have been keeping pace with the increasing speed of computers. Flow analysis, including the modeling of an entire engine room, used to take several months, but now takes about 2 weeks, making the models available for machine
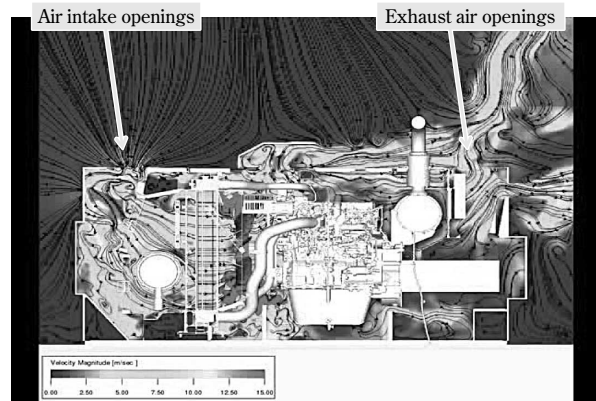
Fig. 9 Analysis of cooling air flow in engine room

development. **Fig. 9** shows the result of an analysis using the lattice Boltzmann method on the cooling air flow inside an engine room. The lattice Boltzmann method approximates fluid as an aggregation of a finite, but large, number of hypothetical particles, each having a velocity. The method uses lattice Boltzmann equations to calculate the velocity distribution function from the collisions and translational motions of the particle and to determine parameters such as velocity and pressure in the flow field. So far as the speed of calculating for large-scale models is concerned, this method is superior to conventional numerical calculation based on Navier-Stokes equations and has the advantage of the calculations being made using actual shapes without simplifying them. The method is useful not only for the numerical evaluation of air flow, but also for confirming and counter-measuring the stagnant flow and eddies.

2.3.3 Acoustic analysis

Conventionally, acoustic analyses required a large amount of time. Sound source models have become even more complicated. The analysis time and complicated modeling have made the practical adaptation of the analyses difficult. We have collaborated with the Mechanical Engineering Research Laboratory, Kobe Steel, Ltd., to develop a method that works in a practical way in machine development.

1) Technology of acoustic field analysis in high-frequency regions

Conventionally, the boundary element method, a type of numerical analysis technique, has commonly been used for acoustic field analyses. The boundary element method is a method for numerically solving boundary integral equations, derived from the governing differential equation for the field, through discretization. This method is advantageous in sound analysis in that it requires the meshing only of

the boundary surface of the subject space and calls for no special boundary condition for the problems of open domain (e.g., acoustic emission to outdoors). However, in the case where a boundary is discretized according to the boundary element method, the boundary must be divided into pitches as short as 1/8 wavelength of the sound to attain sufficiently high analytical accuracy. Therefore, the shorter the wavelength and the higher the frequency of the sound, the finer the meshing becomes. This requires a significantly large amount of calculation time and a large memory capacity.

Fig.10 shows the relation between the number of elements and the analysis time in different analysis techniques. When considering an acoustic field analysis on the scale of construction machinery, the maximum frequency has conventionally been limited to about 500Hz. Modern computers with improved performance and a newly developed algorithm (e.g., the fast multipole boundary element method) have gradually enabled the analysis of higher frequencies; however, the requisite calculation time and memory capacity have not yet reached a level permitting the use of this method in practical design. Focusing on the fact that high-frequency sound is less affected by fluctuations, we have developed a technique for analyzing acoustic fields. The newly developed method (acoustic radiosity method) adapts the radiosity method[3), 4)] used for thermal analysis and light transmission analysis (CG rendering technique). The acoustic radiosity method also requires meshing of only the boundary surface, allowing the models to be shared with the boundary element method. Analyzing in the low-frequency range, up to about 500Hz, using the boundary element method, and analyzing in the higher-frequency range, using the acoustic radiosity method, have shortened the calculation time to 1/30 of that required by the conventional method.

2) Technology for modeling sound sources

A conventional method for acoustic field analysis requires inputting vibration velocities for all the elements of a structure. The number of elements increases with increasing frequency and reaches several tens of thousands in the high frequency region, as shown in Fig.10. Analyzing vibration velocity requires the measurements of several tens of thousands of data points, which makes the analysis impractical. We have managed to reduce the number of measurement points from several tens of thousands down to several tens by adapting an equivalent sound source method, in which the measurement points are replaced by equivalent and simple sources of sound. More specifically, the sound sources were identified by the following procedure.
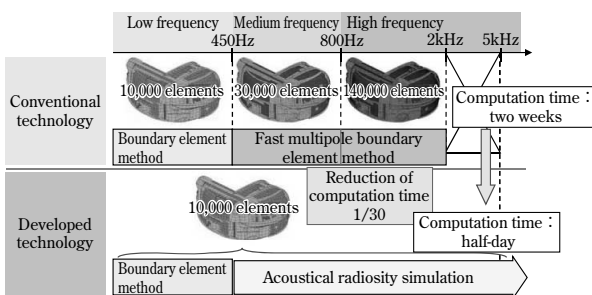
① Measuring sound pressure, p, in the surrounding area during actual operation.
② Measuring the transfer function, H, of the sound pressure in the surrounding area while assuming a sound source on the surface.
③ Determining the equivalent sound source, q, satisfying the sound pressure distribution during actual operation. ($p = Hq$)

Fig.11 shows the result of accuracy verification for the acoustic field analysis up to 4,000Hz. An engine is considered, for which the vibration velocity should preferably be input at intervals of 10mm, or 1/8 of a wavelength. The result compares a case in which intervals of 200mm are applied to the conventional analysis with a case in which the same intervals are applied to the newly developed analysis involving the identification of an equivalent sound source. The newly developed equivalent sound source method, inputting a sound source at 200mm intervals, has achieved the same level of accuracy as the conventional method with 10mm intervals and has shortened the analysis and measurement time. The new technology enables the modeling of objects such as fans, whose vibration is difficult to measure directly.

2.4 Evaluation results

Fig.12 compares the sound power levels, at 1/3 octave frequencies, of the enclosures before and after the modification. In the frequency range higher than 400Hz, the noise emission of the modified enclosure

Fig.10 Sound analysis technology of high-frequency region

Fig.11 Modeling Accuracy of of the sound source

Fig.12 Comparison of measured PWL between original and improved enclosure

is more than 10dB lower than that of the conventional enclosure, contributing to the reduction of overall noise.

Fig.13 compares the noise levels at points one meter away from the machine. The noise is reduced by 10dB at points on the left hand side of the cabin, which allows smooth communication between the operator and workers.

Once the sound radiating from the enclosure opening is reduced significantly, the solid-borne sound of hydraulic origin, the sound emitted from vi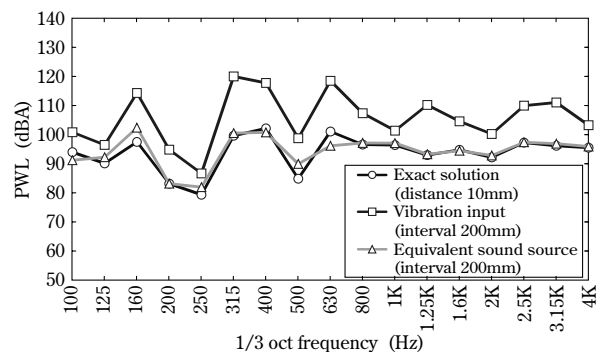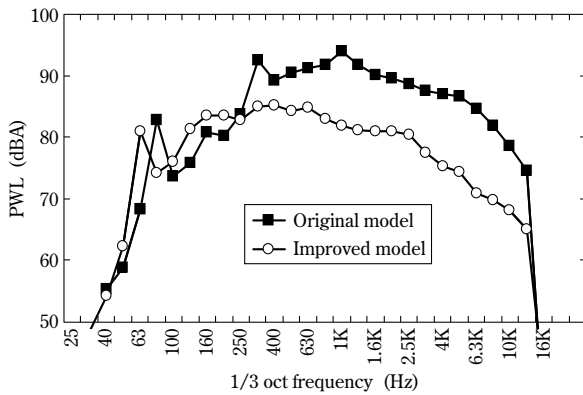brating surfaces, stands out more, deteriorating the sound quality. A technique for improving the sound quality has been adapted to the hydraulic pipe supports to reduce their potential for transmitting vibration. **Fig.14** shows the changes in auditory feeling[5] over time, before and after the modification, during three cycles of excavation work. The modification has reduced the value, improving the overall result.

2.5 Product development and New Technology Information System (NETIS)

The newly developed technology is employed in three models of the ACERA Geospec SR series. As previously shown in Fig.1, the current models (depicted by △) were upgraded to new models (depicted by ○) with the aim of noise reduction. These models, SK135SR and SK235SR, have achieved a noise level that is 5dB lower than the value set by the most stringent regulation, the super-low noise standard of the Ministry of Land, Infrastructure, Transport and Tourism. The SK70SR and SK135SR have achieved noise levels as low as those of mini-excavators.

In 2010, our series was certified and registered under the New Technology Information System (NETIS) by the Ministry of Land, Infrastructure, Transport and Tourism. Thus, by exploiting our
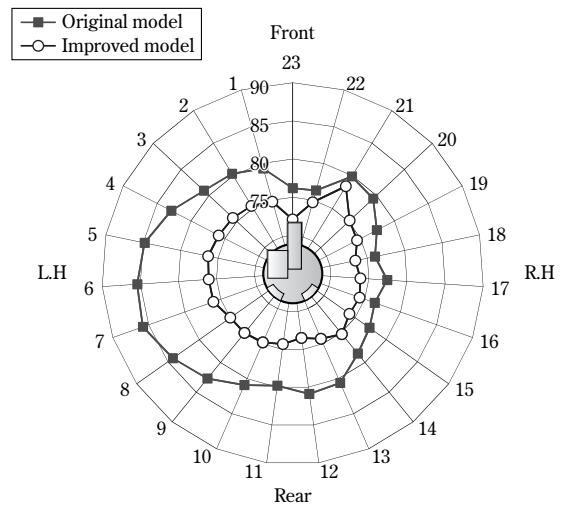
Fig.13 Comparison of noise near machine
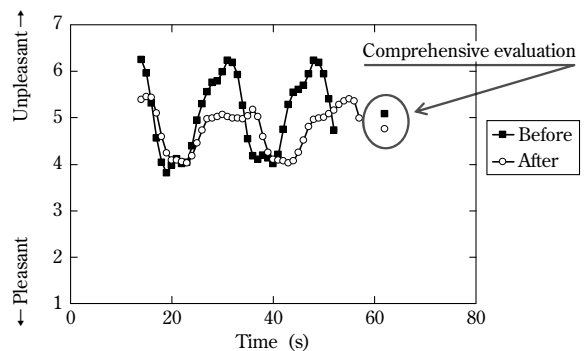
Fig.14 Result of subjective evaluation of pleasant-unpleasant

products, our clients can raise the performance rating for their construction work.

2.6 For further reduction of noise

To lower the noise level even further, the sound of the fan, the major source of noise, must be reduced. This calls for further improvement focusing on the air flow in and around the fan and the development of a cooling system with even less noise. With the recent advancements in the technology for analyzing the fluid noise of fans, a fundamental solution may be expected. It should be noted, however, that the reduction of fan noise can lead to the reduction of the constant component of mechanical sound; and when that happens, variable components linked to excavation work and hitherto masked by the fan noise, may now stand out, deteriorating the sound quality.

Conclusions

Further progress can be expected in the noise reduction of hydraulic excavators. On the other hand, the regulations on exhaust emissions are becoming more and more stringent. As a result, new

challenges are emerging, including increased cooling noise due to the increased amount of heat generated by the engine and the revised equipment layout and soundproofing structure for additional exhaust purification apparatuses. More attention must be paid, not only to reducing the sound from the engine room, but also to reducing other sounds, such as the impact sounds caused by excavation attachments and the rattling sound of traveling apparatuses.

The development of new items is desired for future noise reduction. The improvement of sound quality must be based on the perceptions of those who hear the sounds. It is essential to reduce the noise level even further in the near future, not only in the surrounding area, but also inside the cabin for the amenity of the operator. In addition to the reduction of the noise level, there is a need for further improvement in sound quality, considering the fatigue experienced after extended operation of the machinery and also the fact that a certain amount of sound is required for safe operation. We will continue to pursue the goal of comfortable sound in the acoustic design of hydraulic excavators and thus contribute to provide hydraulic excavators that match the needs of society.

References

1) Office of Odor, Noise and Vibration, Environmental Management Bureau, Ministry of the Environment. *2010 Survey on the Enforcement Status of the Noise Regulation Law*, p.8-9.
2) T. Tanaka et al. *R&D Kobe Steel Engineering Report*. 2007, Vol. 57, No.1, p.43.
3) A. Le Bot et al. *J. Acoust. Soc. Am*. 2000, Vol. 108, No.4, p.1732.
4) S. Siltanen et al. *J. Acoust. Soc. Am*. 2007, Vol.122, No.3, p.1624.
5) Hatano et al. *17th ICA Proceedings Room*. 2001, Vol.Ⅳ, p.189.

Simulation Techniques for Improving the Fuel Efficiency of Hydraulic Excavators

Dr. Etsujiro IMANISHI[*1], **Takao NANJO**[*1], **Akira TSUTSUI**[*2]

[*1] Mechanical Engineering Research Laboratory, Technical Development Group
[*2] Electronics Research Laboratory, Technical Development Group

Simulation techniques to reduce the fuel consumption in hydraulic excavators are presented in three categories: first, a strongly non-linear dynamic simulation technique for a coupling system with a non-linear hydraulic system and a linkage system; second, a technique for evaluating fuel consumption in the engine when the engine powers the hydraulic pump in a digging operation performed by a hydraulic excavator in real time; and, finally, a dynamic simulation technique for evaluating the efficiency of a hybrid system consisting of power electronics equipment, electric-hydraulic equipment, and a linkage system.

Introduction

Due to global warming and a steep rise in the price of crude oil, lower fuel consumption is increasingly required even for hydraulic excavators. As shown in **Fig. 1**, a hydraulic excavator has a power train system, including an engine, a hydraulic pump driven by the engine, and hydraulic piping and valves to move an attachment. Various efforts have been made to reduce the fuel consumption of hydraulic excavators, including the control of pumps and the reduction of pressure loss in their pipes, but this still leaves room for further improvement. Now, all of the systems must be evaluated to further reduce their loss. A hybrid system[1, 2] comprising an engine and battery is considered to be an effective solution.

This paper introduces system simulation techniques that are important in reducing the fuel consumption of hydraulic excavators. The techniques introduced first are a non-linear dynamic analysis technique for a system in which a strongly non-linear hydraulic system is coupled with a linkage system and a technique for evaluating the engine fuel consumption of a hydraulic excavator during a digging operation in which the power for the hydraulic pump is loaded on the engine in real time.

This is followed by the introduction of a dynamic simulation technique for a hybrid system, based on the modeling of the total system consisting of electronics components, such as a generator, battery and converter, constituting a hybrid power source; electro-hydraulic components that constitute an actuator system; and a linkage system for attachments.

1. Power evaluation and reduction of fuel consumption of hydraulic excavators

1.1 Contribution analysis of power loss in hydraulic system

To conduct a coupled analysis of the hydraulic system and linkage system of a hydraulic excavator, the coupled system is described in an MCK type, non-linear equation of motion,[3] using state variables of displacement for the linkage system and the integral of the flow rate for the hydraulic system. This has enabled numerical integration by an implicit method and has stabilized the analysis of the strongly non-linear system. In the linkage system, beam elements[4] and truss elements are used, in consideration of the geometrical non-linearity caused by the large motion in a space. These elements are used for modeling the attachment of the hydraulic excavator (**Fig. 2**). The hydraulic system was modeled using piping elements, valve elements, cylinder elements[5] and the like, as shown in **Fig. 3**. In each cylinder element, the flow of hydraulic oil in and out of the port either extends or

Fig. 1 Power train system of hydraulic excavator
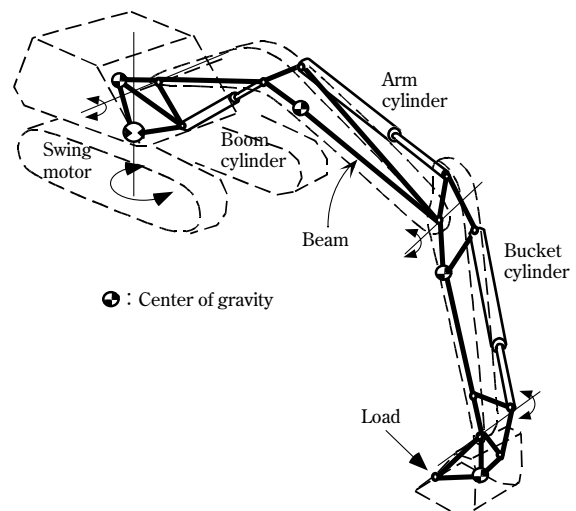
Fig. 2 Modeling of attachment of hydraulic excavator

contracts the cylinder, causing a pressure inside the cylinder, in accordance with the load applied at the end of the cylinder axis. In the cylinder elements, the integral of the flow rate of the hydraulic oil in the hydraulic system is coupled with the nodal displacement of the linkage system, enabling the coupled analysis.

To verify the validity of the present analysis, the evaluation of a hydraulic excavator during two cycles of digging work was compared with the experimental results. A digging task roughly consists of digging, boom raising, dumping, boom lowering and swinging. It involves all the actuators except for the one used for traveling. **Fig. 4** compares the

experimental and analysis results for the actuator behavior, pump power and fuel consumption. The analysis fairly reproduces the actual performance with an error in fuel consumption of no greater than 0.4%. The power losses occurring in various parts of the hydraulic system are obtained from the results of the analysis (**Fig. 5**). **Fig. 6** shows the losses classified by the elements of the hydraulic system, such as piping, valve opening and valve passage. This diagram indicates the contributions of the losses occurring in the hydraulic system during a digging task, an important result used for determining a quantitative energy-saving guideline. Based on the result shown in Fig.6, a specific target was set to halve the power losses for the portions where they are significant.

This technique has enabled us to analyze the complex motions of a hydraulic excavator during a digging operation in a detailed and accurate manner. The clear definition of the contribution to energy-saving has enabled an effective reduction of the power loss caused, for example, by the pressure loss at a valve, and has realized a hydraulic system for

Fig. 3 Hydraulic system of hydraulic excavator
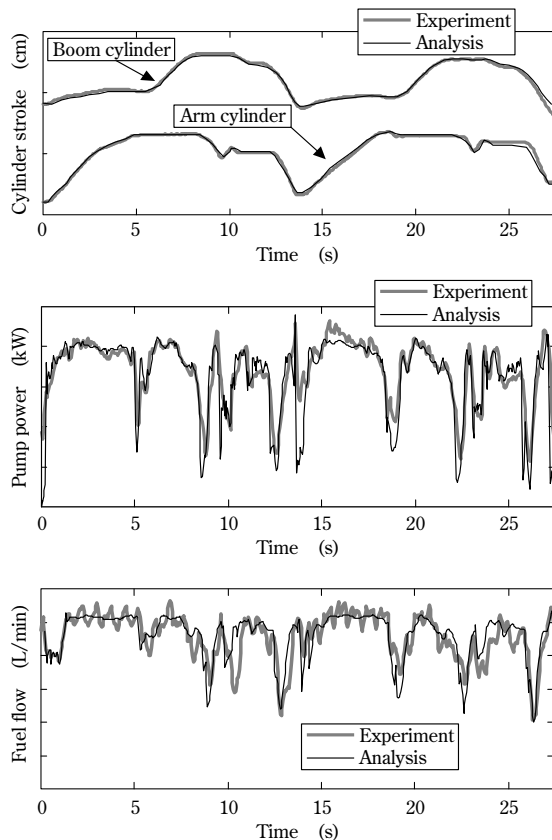
Fig. 4 Comparison with experimental and analytical results in digging operation

Fig. 5 Simulation results of hydraulic loss power in digging operation

Fig. 6 Simulation results of power loss contribution generated in hydraulic system

hydraulic excavators with high energy savings.

1.2 Technique for reducing power loss in hydraulic system

The results of the loss contribution analysis indicate that the pressure losses inside the valves account for the major portion of the power loss in the hydraulic system. Expanding all the internal passages enlarges the valves, making it difficult to mount them on a hydraulic excavator; so we focused on the most effective passages, as indicated by the loss contribution analysis, and expanded them.

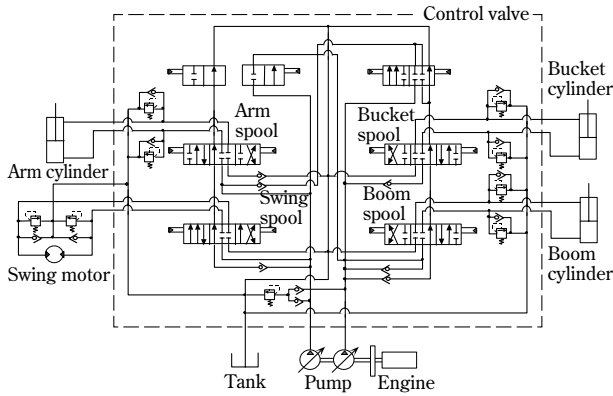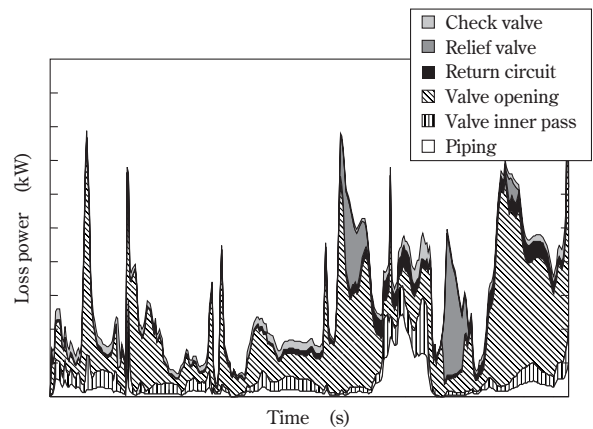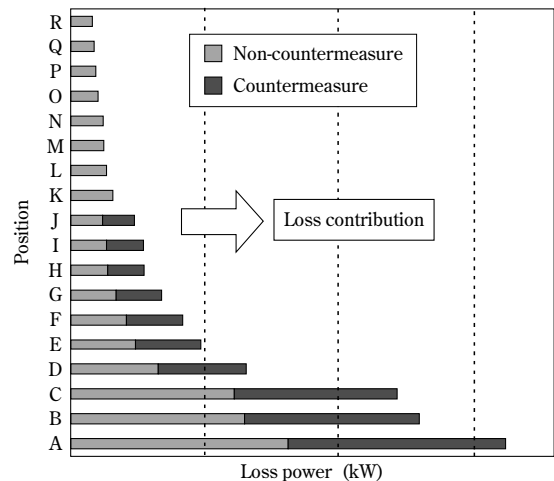The loss contribution analysis also identifies the relief valves of the hydraulic system, which are used in swinging, as major parts causing power loss in the hydraulic system. Therefore, we devised a swinging relief control, combined with a pump flow control. In the hydraulic system for the swinging motion of a conventional hydraulic excavator, the oil from the hydraulic pump is supplied to the hydraulic motor during acceleration, but a portion of the flow is unused and discharged from the relief valve. Hence, we focused on the characteristics of the relief valves and devised a control method in which the pump pressure signal is used to control the supply flow from the pump, such that the flow that had been unused and discharged from the relief valve is minimized, while securing the pressure required for the swinging motion. Other improvements made on the hydraulic system include a control method in which the pump control and valve control are optimally combined to optimize the pump supply flow, which has led to a significant reduction of loss in the hydraulic system.

1.3 Evaluation and improvement of engine fuel consumption

Fig. 7 is a conceptual diagram showing a "hardware in the loop simulation" (HILS) system. This particular system includes an engine (engine
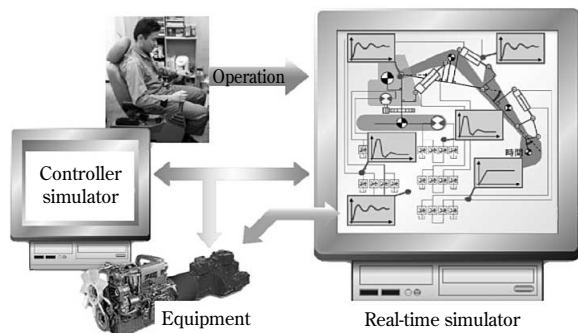
Fig. 7 Configuration diagram of engine HILS system

HILS), in which the hydraulic pump power, in response to the operating lever during actual operation, is determined by simulation and loaded on the engine in real time. This system has an animation display capability which allows lever operations in response to the actual movement of the attachment. The engine HILS system for engines integrates the system analysis and engine bench evaluation technique, thereby enabling the evaluation of the fuel consumption performance of the engine during various operations without a load pattern. This new technique has enabled the highly accurate test-bench evaluation of the fuel consumption of the engine installed on a hydraulic excavator. Efforts have been made to improve the fuel consumption of, not just the engine alone, but the entire system. As a result, the newly developed engine-pump control technique has optimized the fuel consumption performance of the engines of hydraulic excavators.

An engine purchased from a truck manufacturer is tuned for trucks; therefore, it must be adapted for the load imposed by a hydraulic excavator. A truck engine is tuned to exhibit high fuel consumption at a low rotational speed, which deteriorates fuel consumption in the region suitable for a hydraulic excavator. For this reason, the engine HILS system was used to optimize the fuel consumption characteristics of the excavator engine. As a result, a significant improvement has been achieved in fuel consumption in the high torque region.

As for engine-pump control, a conventional machine, which prioritizes productivity, aims at maximizing the horse power at the maximum rotational speed. However, the problem with this approach is that engine combustion efficiency is sacrificed at high rotational speeds at which the torque is low. An isochronous control was adapted for controlling the rotational speed so that it would be as low as possible and kept at a constant level, with the aim of optimizing the pump control and engine revolution. As a result, the fuel consumption has been reduced significantly.

1.4 Low fuel consumption effect

The energy-saving technology of the hydraulic system and technique for improving engine fuel consumption have achieved fuel consumption reductions of 20% for S-mode digging accomplishing the same amount of work, and an improvement of 8% in the amount of work for H-mode digging using the same amount of fuel, when compared with a conventional 20 tonne class hydraulic excavator. The fuel consumption was measured according to the Japan Construction Mechanization Association

Standards (JCMAS). The results confirmed a 17% reduction in fuel consumption, compared with the conventional machine.

2. Development of hybrid hydraulic excavator

2.1 Hybrid system outline

An exterior view and system configuration of a hybrid excavator are shown respectively in **Fig. 8** and **Fig. 9**. The system consists of independent actuators. This reduces the hydraulic distribution loss that occurs in conventional hydraulic excavators. The hybrid power source is a series system consisting of an engine, battery and capacitor for leveling the engine power.

2.2 Power source system

Because the power source is a series system, the power is supplied from the hybrid power source to each actuator via a direct current bus. Therefore, the power is supplied and distributed to each actuator in accordance with the actuator's power consumption. For a stable supply of power from the power source to the actuators in accordance with their power
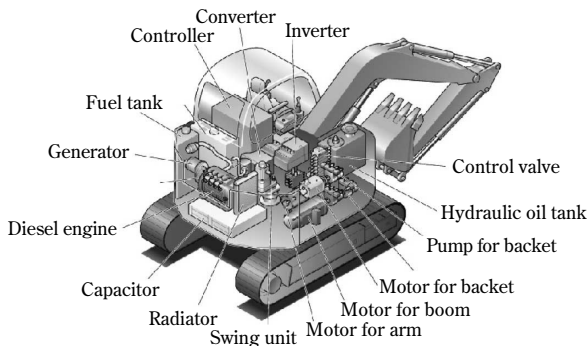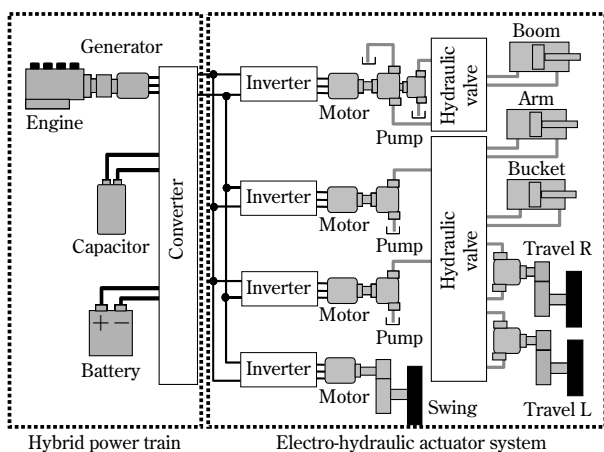
consumption, the control keeps the voltage in the direct current bus constant (direct current bus voltage control).

2.3 Actuator system

The actuator system consists of a boom system, arm-bucket system, traveling system and swing system. The boom system, holding the weight of the attachment, is an electro-hydraulic system that is closed and comprises an electric motor, bi-directional hydraulic pump and control valve, designed to regenerate the potential energy accumulated while the boom is raised. The hydraulic power generated by the boom head when the boom descends is exerted on the bi-directional hydraulic pump, which generates regenerative electric power in the electric motor. This regenerative electric power is charged into the capacitor and battery. The arm-bucket system is an open system comprising an electric motor, mono-directional pump and direction control valve. The swinging system is a system driven by an electric motor and does not employ hydraulic devices because of its rotational motion. The traveling system is a system driven electro-hydraulically, using the hydraulic source for the arm and bucket.

2.4 System equations

The mathematical model of a hybrid excavator consists of system equations, in which the equations, formulated for the elements of the linkage system, hydraulic system, power electronics system, and engine system, are combined according to the formulation of the finite element method[6]. **Fig.10** depicts the configuration of the mathematical model for a hybrid system. The characteristics matrix generated for each element and the system command for the power source system and actuator system are incorporated into the matrix and external force terms of the system equations. Subsequently, the system equations of motion are solved for each time step to conduct a simulation. This technique employs the Newmark β method for time integration and Newton's method for convergent calculation, which secures the stability of the numerical analyses.

Fig. 8 Conceptual scheme of hybrid excavator

Fig. 9 System diagram of hybrid excavator
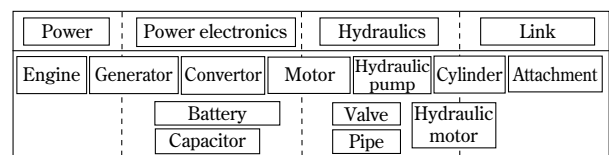
Fig.10 Configuration of mathematical model of hybrid system

2.5 Performance evaluation analysis and accuracy verification

Various performance evaluation analyses were conducted using the total simulation model for the hybrid system. A hybrid excavator was built for performance demonstration so that it could be compared with that of a conventional machine.

As an example of power evaluation during actual operation is shown in **Fig.11**, in which performance evaluations were conducted on the power of the actuators during excavating and dumping tasks, typical tasks for hydraulic excavators. The action is a combined action of the four actuators for the boom, arm, bucket and swing. The comparison was made between the sum total of the input power supplied to the electric motor for driving the actuators of the hybrid system and the output power from the hydraulic drive pump of the conventional machine, this output power being regarded as the power input to the actuators. In the hybrid system, a significant reduction of input power is observed in the later stage of the operation, the stage where the actuator output becomes low, which verifies the reduction of hydraulic distribution loss during low hydraulic output, as intended. **Fig.12** shows the energy balance of the actuator system during this operation. During the operation, a power reduction of approximately 45% was achieved, as compared with the conventional hydraulic system.
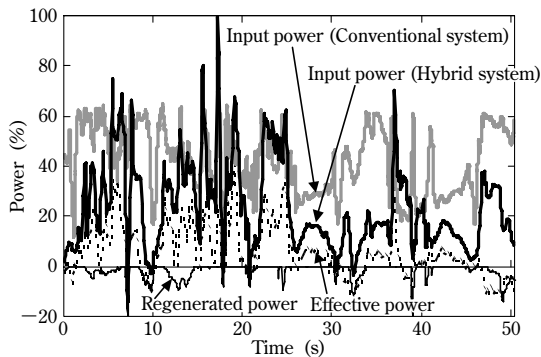
Fig.11 Actuator power on excavating and loading
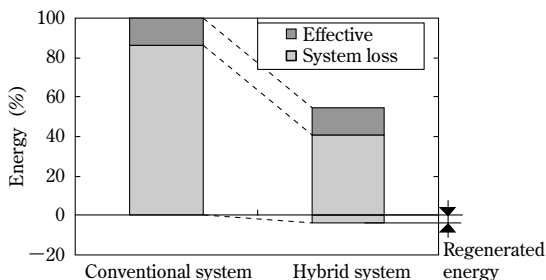
Fig.12 Energy consumption of actuator in excavating and loading
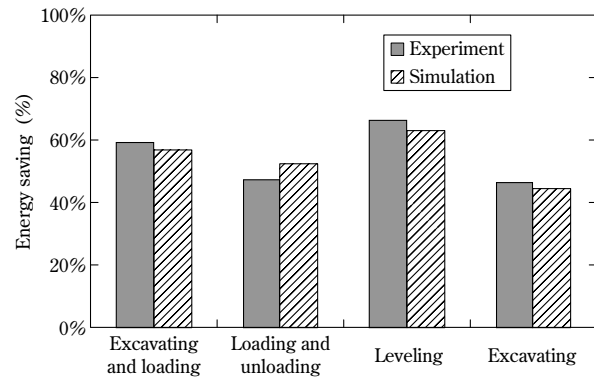
Fig.13 Experimental and simulation results of fuel energy saving effect on each operation mode

The total simulation model was used to evaluate the fuel consumption performance during typical work patterns, including the aforementioned excavating and dumping tasks. The result was compared with the performance of the actual machine for verification. **Fig.13** shows the energy-saving effect of the hybrid system, as compared with the conventional system. Also shown in the figure are a comparison of results for the actual machine and the simulation model. Overall, energy-saving effects of no less than 40%, compared with a conventional machine, have been achieved for all the types of operation, although the effects vary according to the type of operation. The simulation results and the results actually measured on the demonstration machine yield the same energy-saving effects within a 5% margin of error. The target performance has been achieved as intended. This verifies that the simulation technique according to the present method is a practical technique for accurately predicting the fuel consumption performance of hybrid excavators.

Conclusions

The technology used for the development of an energy-saving type of hydraulic excavator has been outlined in this paper. The need for energy-saving-type hydraulic excavators will continue to increase; however, it is difficult to achieve any significant improvement solely by improving the current power system losses, which requires the development of new systems. To carry out this purpose, a system evaluation technique covering power electronics is indispensable. We will continue to strive for further energy saving and contribute to the protection of the global environment.

References

1) H. Inoue. *KENSETSU NO SEKOU KIKAKU.* 2009, No. 707, p.30-34.
2) M. Kagoshima. *KENSETSU NO SEKOU KIKAKU.* 2009, No.707, p.40-44.
3) E. Imanishi, et al. *Transactions of the Japan Society of Mechanical Engineers (Trans. Jpn. Soc. Mech. Eng.).* 2003, Vol.69, No.685, p.2336-2343.
4) H. Zui et al. *Transactions of the Japan Society of Mechanical Engineers (Trans. Jpn. Soc. Mech. Eng.).* 1986, Vol.52, No.483, p.2814-2821.
5) E. Imanishi, et al. *Transactions of the Japan Society of Mechanical Engineers (Trans. Jpn. Soc. Mech. Eng.).* 1987, Vol.53, No.492, p.1711-1719.
6) T. Nanjo, et al. *Transactions of the Japan Society of Mechanical Engineers (Trans. Jpn. Soc. Mech. Eng.).* 2011, Vol.77, No.782, p.3694-3704.

Reducing Weight and Width of Latticed Boom Crawler Cranes

Teppei MAEDO[*1], **Yasuo ICHIKAWA**[*1], **Yutaka KOBAYASHI**[*2], **Eiji MIYA**[*2],
Takunori YAMAGUCHI[*3], **Hiromitsu HAMAGUCHI**[*3]

[*1] Engineering & Development Div., System & Component Development Dept., KOBELCO CRANES CO., LTD.
[*2] Engineering & Development Div., Crane Engineering Dept., KOBELCO CRANES CO., LTD.
[*3] Mechanical Engineering Research Laboratory, Technical Development Group

Reduction of the transportation width to less than 3m and the transportation weight to less than 32 tonnes in Japan (45 tonnes overseas) have been achieved for latticed boom crawler cranes (LBCCs) of the 110 tonne and 250 tonne classes. The lifting weights of the 110 tonne and 250 tonne class cranes are comparable with those of our cranes already on the market. One of the important factors in this achievement is the weight reduction of the boom without sacrificing their lifting capacity. To this end, structural analyses of the booms have been performed using finite-element simulations, and their operational ability has been verified by a newly produced general-purpose LBCC.

Introduction

Latticed boom crawler cranes (hereinafter referred to as "LBCCs") are the flagship products of KOBELCO CRANES CO., LTD. The company has one of the largest market shares in the world. The high rate of the yen and the rise of Chinese manufacturers in recent years, however, have made the competition more intense for general purpose LBCCs with lifting capacities no greater than 250 tonnes. Against this background, and to ensure its position as a top runner with outstanding technology, the company has newly developed and launched twenty-one types of general-purpose LBCCs. This market release was backed by new emission regulations, such as Interim Tier 4 (North America) and Stage ⅢB (Europe), enacted in 2011.

The development of the new cranes was based on three product concepts: namely, ensuring safe and secure work anywhere in the world (meeting all the regulations for environment, transportation and safety), enabling efficient work and safety management (improved transportability, low energy consumption, work history management and optimized structure), and allowing efficient maintenance (preventive maintenance based on the work and maintenance history).

Among these product concepts, developing a structure with improved transportability has turned out to be of particular importance. Generally, when an LBCC is to be transported, its main body is disassembled and loaded onto a trailer. However, different countries have different regulations for the

mass and width (transportation width) of the load that a trailer can carry. Besides this, construction projects are often planned at narrow sites, for example in European cities, where the location calls for a machine that can be disassembled into a narrower width for transportation.

Therefore, there has been a need to remodel conventional machines to further decrease the transportation widths of their main bodies and to reduce their weights down to a level that meets transportation regulations.

This paper describes crane structures with special focus on their weight reduction.

1. Development goals

Table 1 compares the transportability of 110 tonne class LBCCs, including the current model and a new model (one example), as well as two machines built by other companies.

The newly-developed general-purpose LBCC is designed to meet the following requirements for

Table 1 Comparison of transportabilities among the current model, new model, and other companies' cranes (Overseas model of the 110 tonne class)

	KOBELCO		Company L	Company T
	Current model	New model		
Weight of transportation (t)	40.7	36.4	36.7	37.0
Width of transportation (m)	3.2	2.99	3.5	3.6
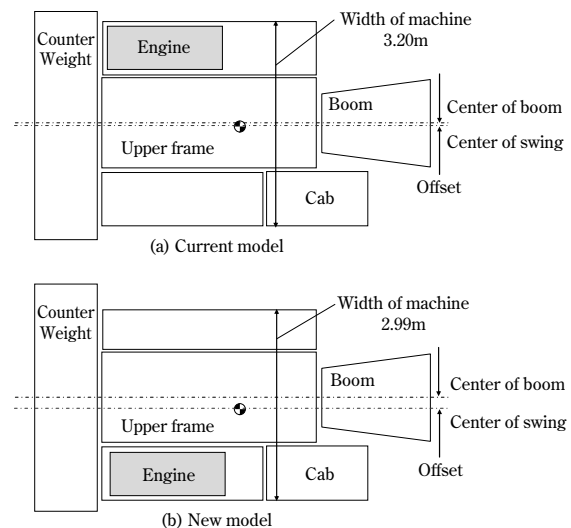
Fig. 1 Comparison of machine width in current and new models

transportation after disassembly:
· Transportation width: 2.99m or less (**Fig. 1**)
· Transportation mass: 32 tonnes or less (Japanese model), 45 tonnes or less (overseas model)
The new machine is designed to have a lifting capacity comparable with that of conventional machines.

2. LBCC structure

As shown in **Fig. 2**, an LBCC has an upper body, a car body and a lower body. The upper body includes

(a) General view

● : Bearing fixed bolt (Lower body)

▲ : Bearing fixed bolt (Upper body)

(b) Zoomed view of boom, upper body and lower body
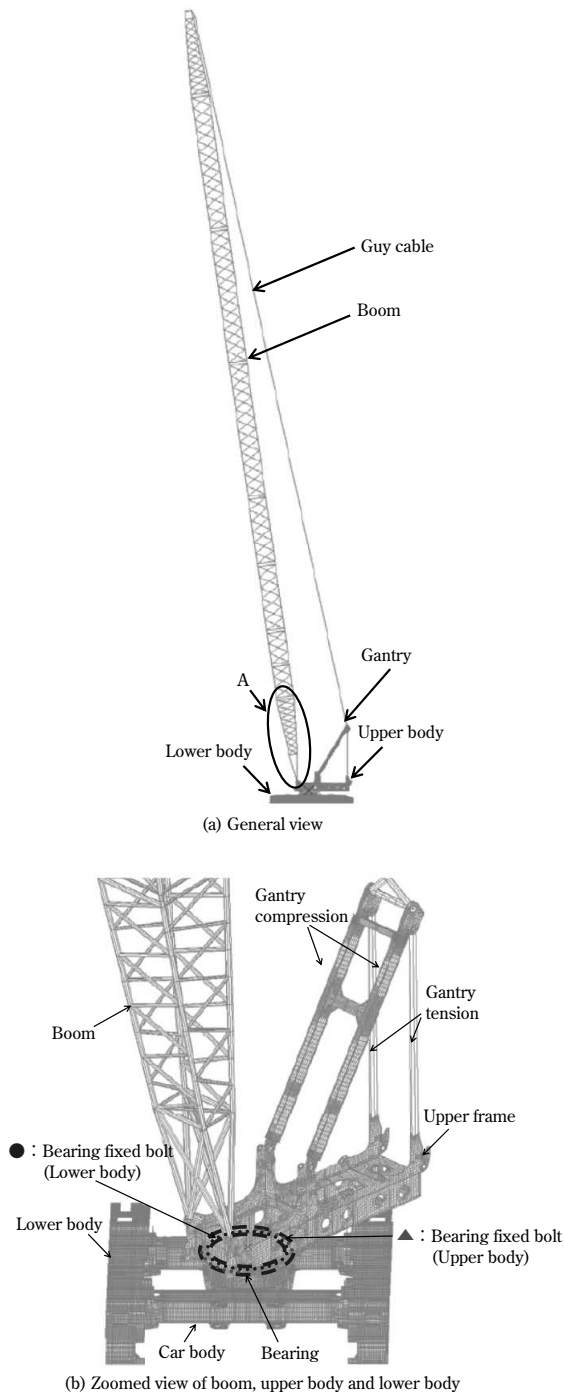
Fig. 2 FEM model of LBCC (110 tonne class)

a slewing frame and a gantry, in which the slewing frame carries major components such as a boom, cab and engine. The car body is connected to the slewing frame via a slewing bearing. The lower body is connected to the car body and is equipped with a pair of crawlers that touch the ground. These upper and lower bodies are the critical elements in the structural design.

3. Weight reduction of the structure

As shown in the comparison in Fig. 1, the structure with a transportation width of no greater than 2.99m has an offset, or distance between the boom's center and slewing center, greater than that of the conventional structure. This causes an offset load to be exerted on the main body. Reducing the structural weight to meet the transport regulations of various countries may decrease the structural stiffness. This reduction also increases the deflection of the boom as well as the axial force exerted on the screw bolts that fasten the slewing bearing, posing a problem.

The primary structural requirements for an LBCC are strength and stiffness for lifting operations. In the current development, the cross sectional areas are secured to the greatest degree possible within the limitations of the transportation performance set as a development goal. A finite element method analysis was performed to optimize and determine the structure and shapes. For example, in the case of the 110 tonne class LBCC, in which the determinant for strength is the maximum side-ways deflection of the boom, the aim was to reduce the total mass of the lower boom portion, slewing frame and car body by about 3.1 tonnes, as compared with the conventional model, to achieve the transportability goal. In the case of the 250 tonne class LBCC, on the other hand, the determinant for strength is the maximum axial force, which is exerted on the screw bolts that fasten the slewing bearing and is caused by an inhomogeneous stiffness distribution in the main body. To achieve transportability for this model, the goal was to reduce the total mass of the slewing frame and car body by about 0.7 tonnes, as compared with the conventional model. The following describes the details of the weight reduction achieved for these two models, the 110 tonne class and 250 tonne class LBCCs.

3.1 Analysis model

Fig. 2 shows a finite element method (FEM) model of an LBCC. In this model, the slewing frame, car body, crawler, gantry compression member, guy

cables and slewing bearing are regarded as "shell elements"; the attachment is regarded as a "beam element"; and the gantry tension member is regarded as a "truss element". The upper body and lower body are connected by a "beam element" or by a "rigid element" at the axial center of each screw bolt fixing the slewing bearing.

Analyzing the entire structure of an LBCC, as described above, allows evaluation of the stiffness and deformation, not only of the subject part, but also of other relevant structural parts, unlike a case in which each structural part is independently analyzed. This enables the analysis of the areas adjacent to joints, such as the screw bolts fixing the slewing bearing, without much deviation from the actual measurements, offering a tool for studying reinforcement with minimum mass.

The load conditions for the 110 tonne class LBCC were set so as to include a boom length of 70.1m (fully extended), the boom length that maximizes the sideways deflection, a working radius of 12.0m and a lifting load of 19.6 tonnes. On the other hand, the load conditions for the 250 tonne class LBCC include a boom length of 15.2m (fully contracted), the boom length that maximizes the moment load exerted on the slewing bearing, a working radius of 10.0 m and a lifting load of 117 tonnes.

3.2 Weight reduction

3.2.1 Weight reduction of 110 tonne class LBCC

A preliminary verification performed on a 110 tonne class LBCC, using an FEM model (Fig. 2), revealed that the lack of stiffness increases the deflection of the boom to close to the allowable limit when lifting a load. Reinforcement was considered such that the weight would stay within the reduction target. The lower boom portion (designated as "A" in Fig. 2(a)) and a portion of the slewing frame shown in Fig. 2(b), the portion at which the boom is attached, were examined. The details are as follows.

1) Reinforcement of boom and slewing frame

A boom has a lattice structure consisting of pipes and is separated into upper, middle and lower parts, in which each part is connected to the adjacent part by pins. The load exerted at the tip of the boom is transmitted, via guy cables that support the boom, to the slewing frame and to the lower body. As shown in **Table 2**, verification using the FEM model has revealed that reinforcing the lower body has only a small effect on the sideways deflection of the boom. The sideways deflection of the boom is found to be more effectively decreased

by increasing the outer diameter and the wall thickness of the main pipes of the lower boom (portion A in Fig. 2(a)). Reinforcing the slewing frame in and around the area where the boom is attached (**Fig. 3**) is also effective against sideways deflection. Reinforcement measures suggested by the preliminary verification were implemented in an actual machine. The deflection at the tip of the boom was measured and found to be 14% smaller than it was before the reinforcement, and it is well below the allowable limit (**Fig. 4**).

2) Weight reduction for 110 tonne class LBCC

As a result of the above study, the total of the masses of the lower boom portion, slewing frame and car body has been decreased by about 3.1 tonnes, as compared with the conventional machine.

Table 2 Effect of boom, upper body and lower body reinforcement

Part of reinforcement	Reduction of displacement to mass of reinforcement
Boom	▲1.54mm/kg
Upper body	▲0.78mm/kg
Lower body	▲0.17mm/kg
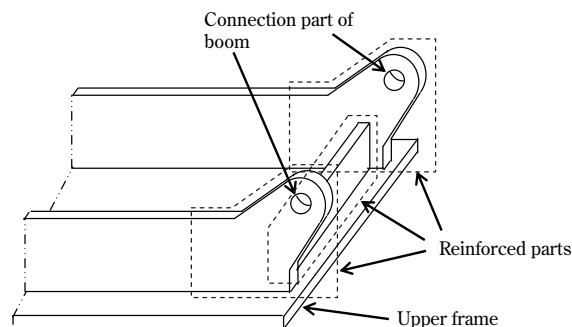
Fig. 3 Reinforced parts of upper frame
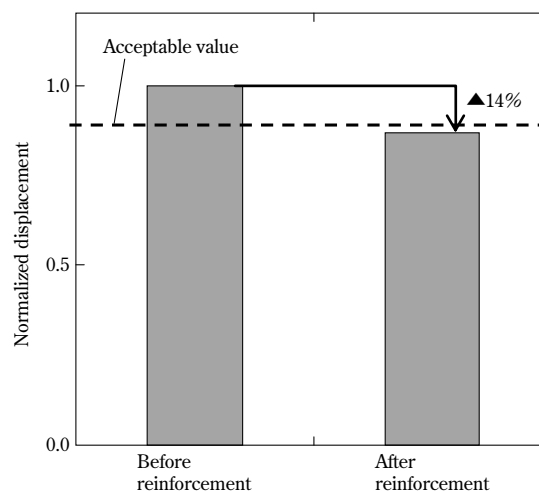
Fig. 4 Effect of reinforcement

3.2.2 Weight reduction of 250 tonne class LBCC

Fig. 5(a) depicts an FEM model of a 250 tonne class LBCC. A preliminary study was conducted using this FEM model. The results show that the increased offset and decreased weight of the main body together have increased the axial force exerted on the screw bolts that fasten the slewing bearing almost to the permissible limit. Thus, reinforcement was considered such that the weight stays within the reduction target. A pair of annular portions on the upper body, to which one side of the slewing bearing is attached (Fig. 5(b), hereinafter collectively referred to as "portion B"), were examined, as were a pair of annular portions on the lower body to which the other side of the slewing bearing is attached (Fig. 5(c), hereinafter collectively referred to as "portion C"). Reinforcement methods were studied for these portions.

1) Reinforcement of portion B

Portion B includes a slewing frame and a slewing bearing, which are held together by screw bolts. As shown in Fig 5(a), the load of lifting is transmitted to the slewing frame, slewing bearing and the lower body via a boom, guy cables that support the boom, a mast, a hoist rope and a gantry. Each portion to which the slewing bearing is attached is subject to a moment load exerted by gantry tension members. This moment load varies from point to point because

it is affected by the offset between the centers of the boom and slewing bearing and also by the distances between the points and the tension members. Due to the offset, portion "D" in **Fig. 6** is subject to a higher moment load around the y-axis, as compared with portion "E". Portion "D" is also subject to a higher moment load around the x-axis because it is located farther away from the gantry tension member. In addition, the screw bolts in and around portion-D are subject to a greater axial force because a side plate of the slewing frame increases the local stiffness.

Accounting for the above, the FEM model shown in Fig. 5(a) was used for a preliminary study of the axial force exerted on the screw bolts. The result indicates that reinforcing portion F in Fig. 6 decreases the axial force exerted on the screw bolts in and around portion D. Reinforcement of portion F is considered to have leveled out the uneven stiffness in and around portion D.

2) Reinforcement of portion C

In the lower body depicted in **Fig. 7**, portion G exhibits a stiffness higher than the periphery because this portion is reinforced by an annular ring and side plate. On the other hand, portion G is subject to the moment and thrust load transmitted from the boom and upper body via the slewing bearing. This causes a large axial force to be exerted on the screw bolts that fasten the slewing bearing in and around portion G.

(a) General view

(c) Bearing fixed part of lower body (part C)

(b) Bearing fixed part of upper body (part B)
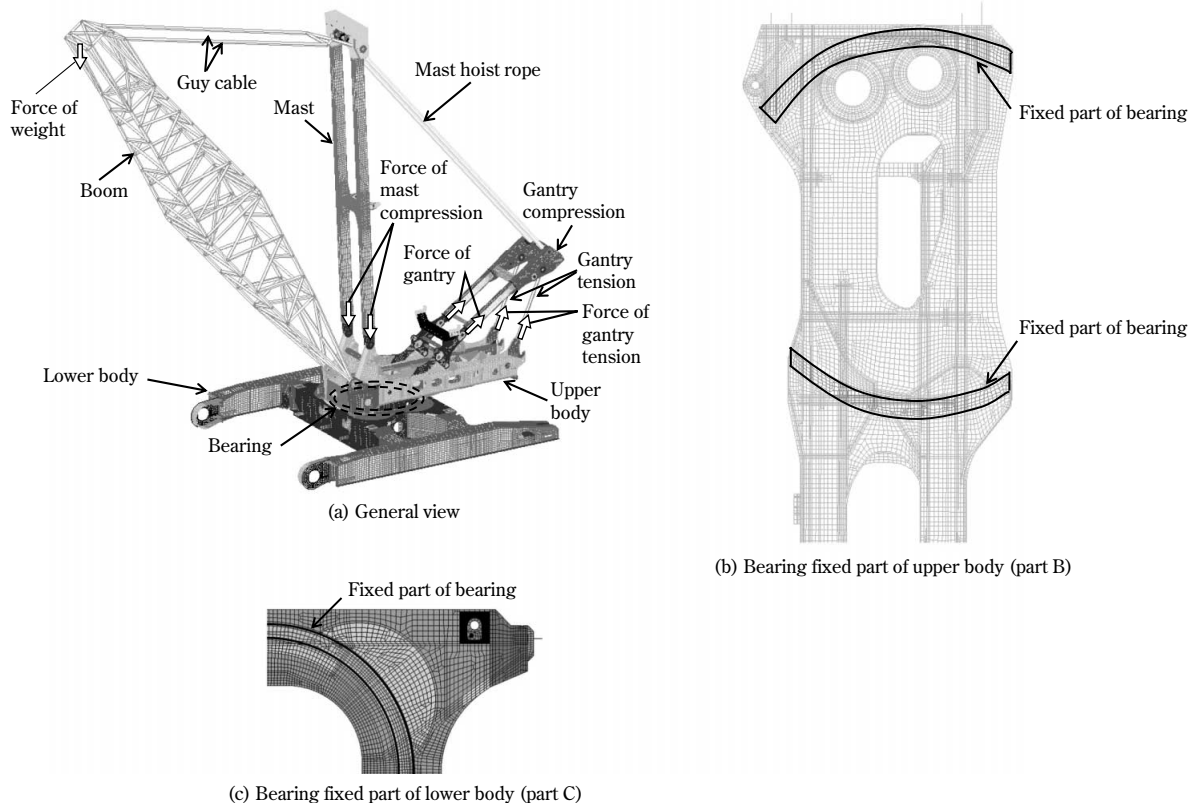
Fig. 5 FEM model of LBCC (250 tonne class)
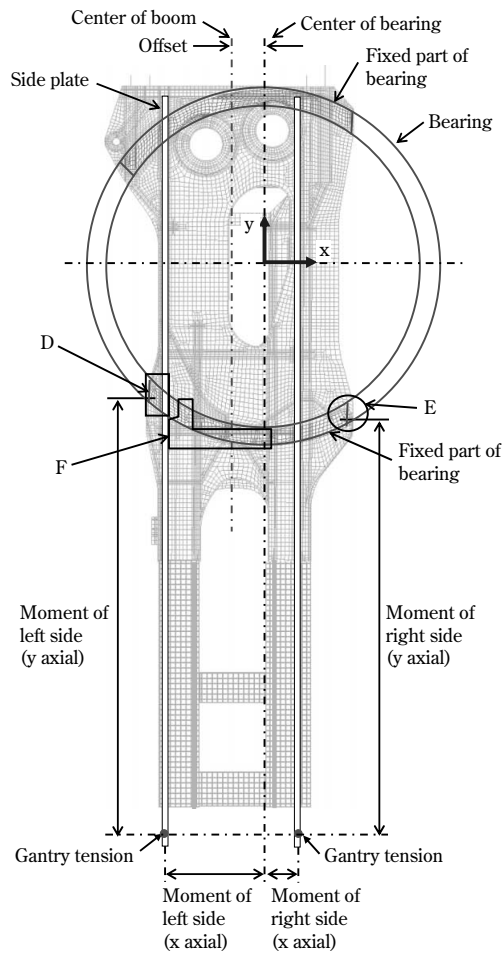
Fig. 6 Reinforcement of bearing fixed part
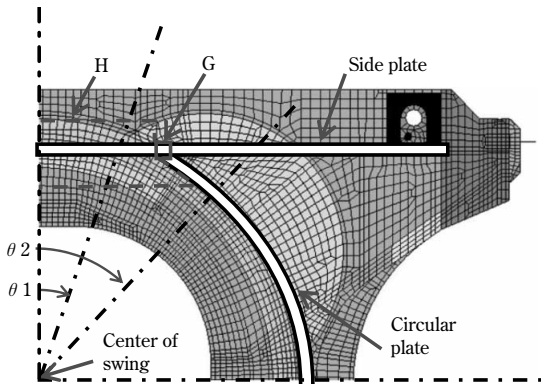
Fig. 7 Reinforcement of lower body
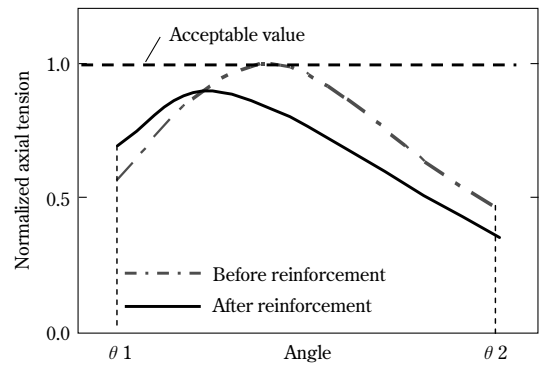
Fig. 8 Bolt axial tension reduction achieved by reinforcement

An FEM analysis was conducted to account for the above. The result indicates that reinforcement of portion H in Fig. 7 levels out the uneven stiffness in and around portion G, decreasing the axial force exerted on the screw bolts. The reinforcement of portion H based on this result, as well as the reinforcement of portion F, as described in section (1), have decreased the axial force exerted on the screw bolts to a point below the allowable limit (**Fig. 8**).

3) Weight reduction of 250 tonne class LBCC

As a result of the above study, the total mass of the slewing frame and car body of the 250 tonne class LBCC has been decreased by approximately 0.7 tonnes, as compared with the conventional machine.

Conclusions

The method of reducing the weight and simultaneously securing the stiffness of a general-purpose LBCC of 250 tonne class or smaller is described. The technique for analyzing an entire body, as introduced in this paper, is a versatile approach and is adaptable to LBCCs larger than the 250 tonne class. Such an LBCC has a longer boom, as well as larger upper and lower bodies, and can exhibit larger deformations. We will strive to reduce the weight and to optimize the stiffness of other machines by adopting a similar approach.

Energy Saving System for Crawler Cranes

Katsuki YAMAGATA[*1] ・ Takaharu MICHIDA[*1]

[*1] Engineering & Development Div., System & Component Development Dept., KOBELCO CRANES CO., LTD.

KOBELCO CRANES CO., LTD. has developed a new crawler crane equipped with a system for improving fuel consumption and reducing CO_2 emissions. The system comprises a fuel-saving mode, a high-speed winching mode, an auto idling-stop mode and the positive control of hydraulic pumps. The new crawler crane has achieved a fuel efficiency that is about 30% better than that of the conventional cranes produced by the company.

Introduction

The "Act on Regulation, Etc. of Emissions from Non-road Special Motor Vehicles" (commonly known as the "Off-Road law") was revised. In October 2011, a more stringent emission standard came to be applied to special vehicles using diesel fuel. Transportable crawler cranes are subject to this regulation. To meet the new regulation, KOBELCO CRANES CO., LTD. has made a full model change in a general purpose crawler crane and has begun selling the newly-developed machine (**Fig. 1**). This machine emits less nitrogen oxide (NO_x), non-methane hydrocarbon (NMHC) and particulate

Fig. 1　New crawler crane

matter (PM) in its exhaust. With the concept of placing importance on environmental performance, the machine incorporates new features for saving energy and reducing CO_2 emissions. As a result, the newly-developed machine has a fuel consumption that is approximately 30% less than that of conventional machines (during the general crane work of framing construction in building applications). This paper introduces these new features for energy saving and the reduction of CO_2 emissions. There is also an outline of the technology that enabled these features.

1. Energy saving technology for crawler cranes

Conventional crawler cranes place more importance on ease of operation and operational stability than on energy saving performance. Energy saving measures in conventional crawler cranes, such as those manufactured by KOBELCO CRANES CO., LTD., have been limited to reducing power consumption during no-load operation.

When the running torque of a hydraulic pump is given by T (Equation (1)), the power L is expressed by Equation (2). This sort of no-load operation is attained by placing the operating lever of the actuator in the neutral position. The equations indicate that minimizing the displacement q of the variable displacement hydraulic pump decreases the pressure loss of the hydraulic system, which reduces the running pressure of the pump. Therefore, minimizing the running torque T, expressed by Equation (1), decreases the power consumed during no-load operation.

$$T = pq/2\pi \quad \cdots\cdots\cdots\cdots\cdots\cdots\cdots\cdots\cdots\cdots\cdots (1)$$
$$L = 2\pi TN/60000 \quad \cdots\cdots\cdots\cdots\cdots\cdots\cdots\cdots (2),$$

wherein,

T : running torque of the hydraulic pump (N・m)
p : discharge pressure of the hydraulic pump (MPa)
q : hydraulic pump capacity (cm^3)
L : hydraulic pump power (kW)
N : hydraulic pump revolution (min^{-1}).

The newly-developed crawler crane is also equipped with a system consisting of the following four features designed for energy saving and the reduction of CO_2 emissions:

　i) Energy saving mode
　ii) High-speed winching mode
　iii) Automatic idling-stop

iv) Positive control for hydraulic pump

Other energy-saving features include the improved fuel consumption characteristics of the engine itself and reduced pressure loss in the hydraulic devices and piping. This paper describes the above four new features.

2. Energy saving mode

Fig. 2 shows the specific fuel consumption of an engine installed in the newly-developed crawler crane. In general, the actuator moves at the maximum speed when the engine revolution reaches its maximum. On the other hand, the specific fuel consumption is known to deteriorate with maximum engine revolution. Rather, a relatively high level of specific fuel consumption is known to be achieved near the revolution at which the engine gives the maximum torque. The newly-installed engine also exhibits this behavior.

In order to drive the hydraulic pump in a zone in which the engine exhibits a favorable specific fuel consumption−hence, to save energy−an energy saving mode (trade name "G engine") has been devised to limit the maximum revolution of the engine.

Meanwhile, the efficiency of crane work, or the speed of winching up and down, must not be sacrificed under this energy saving mode. For this reason, the capacity of the hydraulic pump for the main actuator has been increased beyond that of the conventional pump and the pump is constructed such that its maximum capacity can be switched between two levels as shown in **Fig. 3**. Switching between the two maximum levels is configured in such a way as to preserve the relationship expressed by Equation (3). When the energy saving mode is selected, the maximum capacity is switched to q_1. This enables the hydraulic pump to achieve the same discharge rate (rated flow), Q, as that achieved by the maximum revolution (N_2) and the maximum capacity (q_2) in the standard mode, even when the

engine revolution N_1 is limited by the energy saving mode (**Fig. 4**).

$$q_1 N_1 = q_2 N_2 = Q \cdots\cdots\cdots\cdots\cdots\cdots\cdots (3)$$

wherein,

q_1: the maximum pump capacity (cm³) in energy saving mode,

q_2: the maximum pump capacity (cm³) in standard mode,

N_1: the maximum engine revolution under the restriction of the energy saving mode (min⁻¹),

N_2: the maximum engine revolution in the standard mode (min⁻¹), and

Q: the rated flow of the hydraulic pump (cm³/min).

Fig. 5 is a schematic diagram showing a typical hydraulic system for driving the hydraulic devices in a crawler crane. The newly-developed machine is equipped with a hydraulic pump that has a large capacity for running traveling devices and winches
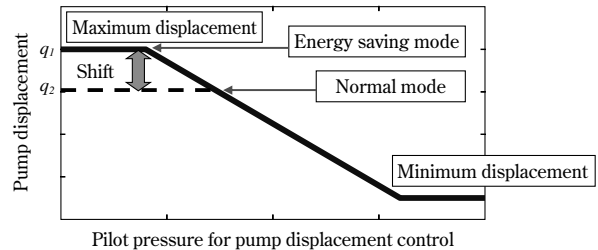
Fig. 3 Pump displacement characteristics
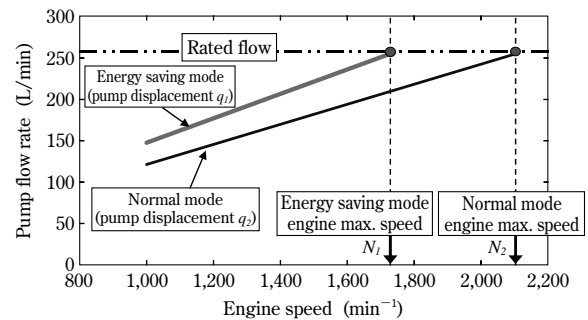
Fig. 4 Characteristics of pump flow rate in energy saving mode

Fig. 2 Specific fuel consumption of engine
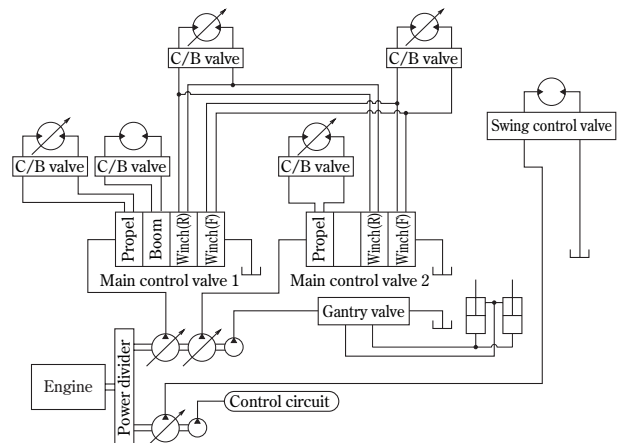
Fig. 5 Hydraulic system of crawler crane

(i.e., main and auxiliary winches). The increased pump capacity, along with the energy saving mode, has realized an energy saving effect during general crane work and continuous traveling.

The system is adapted for switching between an energy saving mode and standard mode. This adaptation was made because limiting the maximum revolution of an engine decreases its power. The switching capability allows an operator to choose the standard mode, which prioritizes engine power in heavy duty work where full engine power is required.

In order to verify the energy saving effect, the specific fuel consumption was measured on an actual machine operating under an average engine load of 20%, emulating general crane work for framing construction in building applications. For a machine equipped with a 271kW engine, the specific fuel consumption was measured to be 35.7L/h for the standard mode and 31.7L/h for the energy saving mode. The result confirms that the energy saving mode achieved an energy saving effect of about 11%. For a machine equipped with a 213kW engine, the standard mode yielded 32.5L/h, while the energy saving mode yielded 28.0L/h for the specific fuel consumption, verifying an energy saving effect of about 14% when in energy saving mode.

3. High-speed winching mode

A conventional crawler crane sets its engine revolution to the maximum even for a small lifting load to operate its winch at maximum speed and to shorten the up/down time. To prevent free fall during the descending operation, the hydraulic circuit that controls the winching is provided with a valve called a "counterbalance valve." This valve is opened with a small supply of pressure to generate a braking pressure that corresponds to the lifted load on its discharge side. This mechanism prevents free fall, while enabling descending operations to be performed with a small amount of power and in correspondence with the supply flow.

However, a varying load and other factors may cause instability, with hunting of the winch during lifting-down operation. Therefore, the valve is generally provided with a dumping property in its open direction. This stabilizes the operation, but sacrifices responsiveness. Because of the dumping property, the counterbalance valve does not open fast enough to discharge a sufficient flow when a small load is lifted. Winching down at maximum speed, with the engine rotating at its maximum revolution, increases the amount of oil in the flow passage on the discharge side, which causes a boost

pressure to be generated at the inlet of the hydraulic motor. This boost pressure causes the hydraulic pump to be driven at a high pressure (designated by ◆ in **Fig. 6**), which generates unnecessary power, deteriorating the fuel efficiency during descending operations. In other words, the prevention of hunting has caused unnecessary power consumption.

The high-speed winching mode (trade name "G winch") focuses on the above issue and enables the winch to move at a rate almost equal to the maximum speed, even when the lifted load is small (**Fig. 7**). More specifically, this feature employs a hydraulic winching-motor that has the capability of switching among three capacity levels characterized by a special intermediate capacity, as shown in **Fig. 8**. This feature allows for setting the hydraulic motor to rotate at a high revolution even when the engine rotates at a low revolution and both the discharge rate of the hydraulic pump and the flow supplied to the hydraulic motor are small. Under normal conditions, the capacity of the hydraulic motor is set to the intermediate level (a), which allows the winch to move at the maximum speed. In a high-
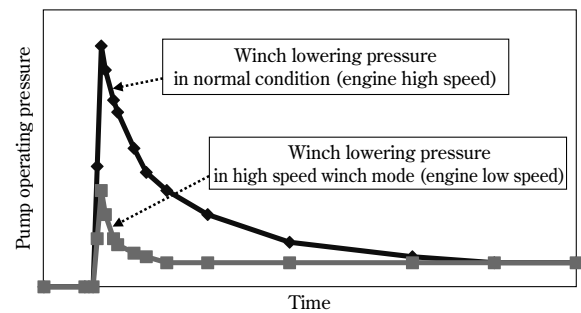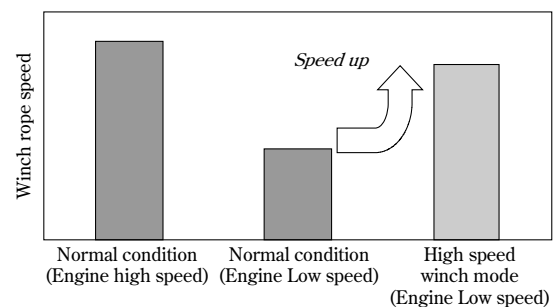

Fig. 6 Pump operating pressure in winch lowering

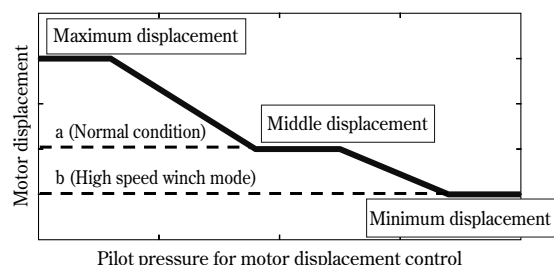Fig. 7 Winch speed in high speed winch mode

Fig. 8 Motor displacement characteristic of three position displacement control type

speed winching mode, the motor is set to the minimum capacity level (b), such that the winch speed is maintained at the maximum rate.

The new hydraulic motor system enables the winching up and down of a small lifting-load at a maximum speed with the engine set at a low revolution, not at the maximum revolution. In addition, the low engine revolution maintains only a small discharge rate in the flow passage on the outlet side of the counterbalance valve, which minimizes the boost pressure acting on the hydraulic pump. As a result, the hydraulic pump is operated at a low pressure (as designated by ■ in Fig. 6), while enabling high-speed winching up-and-down with the engine rotating at a low speed. Furthermore, as expressed by Equation (1), decreasing the driving pressure of the hydraulic pump decreases its running torque, which reduces the fuel consumption by a commensurate amount.

Actual measurement has verified that the momentary fuel consumption is decreased by 60 to 80% when winching down the hook alone.

4. Automatic idling-stop system

Typical crane operations, excluding cyclic loading, have long intervals between the steps in a job. An automatic idling-stop system has a computer that determines if the crane is in idle and automatically stops the engine during idle time. This system cuts unnecessary fuel consumption and exhaust gas (CO_2) emission during idle time. Safety is the major priority in crane work, and all the safety conditions must be satisfied in an idle condition before starting the countdown to the activation of the idling-stop system. The countdown is displayed on a monitor in the cab such that the operator can cancel it. Once the countdown expires (for example, in ten seconds) without a cancelation, the engine stops automatically. Rebooting the engine can be accomplished by simply rotating an accelerator grip, which permits quick restoration from the idle mode (**Fig. 9**).

A study on general crane operations has revealed
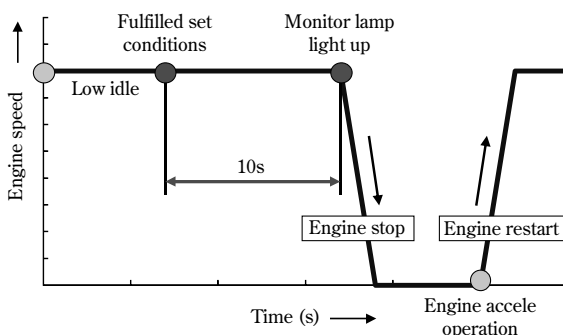
that, in most cases, idle time accounts for 50 to 75% of the entire operating time of an engine. Assuming that the idle time occupies 75% and the engine can be stopped for 37% of the operating time (i.e., half the idle time), it is calculated that there is a maximum energy saving of about 15% (in the case of crane work for general framing construction where the engine load rate is assumed to average 20%).

5. Positive control for the hydraulic pump

As previously described, a conventional crawler crane has been equipped with an energy saving system in which the capacity of its variable-capacity hydraulic pump is minimized only when the operating lever is put into the neutral position. When the lever is in an operational position, however, the hydraulic pump runs at its maximum capacity. In addition, a loss of energy is caused by a surplus flow when the flow (for controlling acceleration, deceleration and precise velocity) is controlled by a valve for controlling operative directions and speed.

The newly-developed crawler crane has a positive control (**Fig.10**) which further upgrades the capacity control of the variable-capacity hydraulic pump. This feature enables the hydraulic pump to discharge a flow of just the amount required by actuators that are controlled by the operating lever. Therefore, the surplus discharge, unnecessary for the work, is minimized, as is the loss of energy during speed control using the operating lever.

The energy saving effect of the positive control is verified by measuring the fuel consumption of an actual machine operating according to a winching pattern as shown in **Fig.11**. The result indicates that significant fuel reductions have been achieved for the
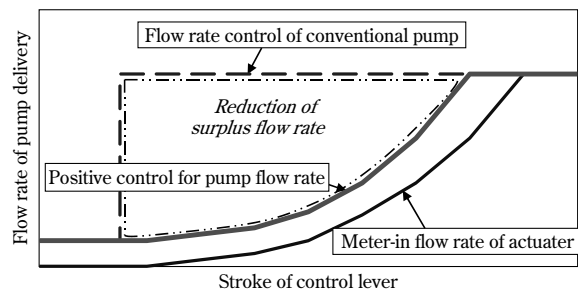
Fig.10 Positive control system for delivery flow rate of pump
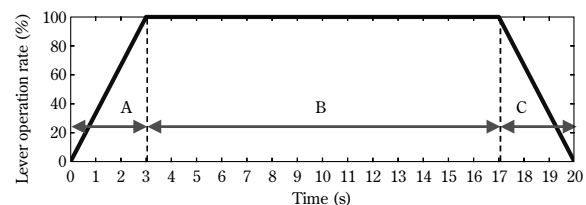
Fig.11 Winch operation pattern

Fig. 9 Auto-idling-stop system

speed control during interval A and interval C. The energy saving effect for the entire operating pattern (interval A + interval B + interval C) has turned out to be about 7%.

Conclusions

This paper introduces new features installed in a crawler crane newly-developed for energy saving and the reduction of CO_2 emissions. The requirements for reducing the environmental burden will become increasingly stringent. We will strive to further advance technologies for reducing the environmental burden so as to meet user needs and thus contribute to society.

Approach for Improving Fuel Consumption of City Cranes

Naoto HORI[*1], Joji TERASAKA[*1], Takahiro KOBAYASHI[*2], Naoki SUGANO[*3]
[*1] Engineering & Development Div., System & Component Development Dept., KOBELCO CRANES CO., LTD.
[*2] Quality Assurance Dept., KOBELCO CRANES CO., LTD.
[*3] Mechanical Engineering Research Laboratory, Technical Development Group

Two control systems have been newly developed for fuel saving in hydraulic wheel cranes: namely, a one-way-clutch system and an advanced engine control system. The former allows one-way transmission of power only in the direction from the motor to the axle and require neither an actuator nor a controller to control the motor action. The advanced engine control system determines the engine rotation speed in response to partial stroke operations of the lever, preventing the unnecessary generation of engine power. It was found that fuel savings of 12% in driving and 20% in crane operation were achieved for the former and the latter systems, respectively, in the practical operation of the cranes.

Introduction

Energy-saving performance has become increasingly important with the rise of fuel costs and the environmental consciousness of the users. In the field of construction machinery, machine makers have been developing new models that feature lower energy consumption to meet new emissions regulations[1,2].

The wheel cranes manufactured by KOBELCO CRANES CO., LTD. mainly rely on hydraulic control systems to transmit power from their engines to actuators for traveling and working. A hydraulic control system has a pump and valves that control the behavior of the actuators, and significant power losses occur in various parts of the system. Therefore, minimizing these losses by optimizing the control system and mechanism is a key to improving the energy saving performance.

In 2008, KOBELCO CRANES CO., LTD. launched a wheel crane, the RK250-7. In 2011, this model underwent a minor change in which newly developed technologies were incorporated to further improve its energy saving performance. This paper describes the approach taken to improve the energy saving performance of the wheel crane and introduces those newly developed technologies.

1. Hydraulic systems in wheel cranes

1.1 Hydraulic system for traveling

The RK250-7 comprises a traveling system including a hydraulic static transmission (hereinafter denoted as "HST")[3,4]. Unlike general torque converters and mechanical transmissions, the HST unit transmits power hydraulically from an engine to a drive shaft.

A wheel crane comprises an upper slewing body having actuators for crane work/jobs and a lower traveling body containing a drive shaft. In a system that employs a torque converter or a mechanical transmission, almost all of the connections, from the engine to the output shaft, are made mechanically. Therefore, the engine must be placed in the lower body, and the actuators, located on the upper body, must receive the hydraulic power via a center swivel joint. The RK250-7, on the other hand, has its engine mounted on the upper slewing body to achieve downsizing while maintaining the lifting capacity of the crane. The power is transmitted from the engine to the drive shaft via the HST unit, allowing a high degree of freedom in the equipment layout.

As depicted in **Fig. 1**(a), the RK250-7 has three hydraulic systems: namely, a traveling system, crane-operating system and auxiliary system. In the traveling system (Fig. 1(b)), the engine drives a variable displacement pump via a power divider. The pump discharges oil to actuate a variable displacement motor that rotates an axle and tires to run the vehicle. The hydraulic circuit is closed such that the oil discharged from the motor is returned to the pump.

When the pump is operated at a constant discharge rate, an increase in the motor displacement increases the driving torque, while a decrease in the motor displacement increases the traveling speed. Increasing the pumping rate, on the other hand, increases the power input to the HST unit. In other words, the HST unit exploits the displacement controls of the pump and motor to control the increase and decrease of the driving torque and traveling speed.

1.2 Hydraulic system for crane operation

Fig.1(c) depicts the hydraulic system for operating the crane. The engine drives a variable displacement pump via a power divider. The oil discharged from the pump is delivered, via control valves, to a motor for winching up and down, a cylinder for telescoping the boom and a cylinder for hoisting the boom. The control valves select actuators to be supplied with hydraulic oil and control the moving direction and

(a) Hydraulic system configuration

(b) Traveling system

(c) Crane operating system

(d) Auxiliary system
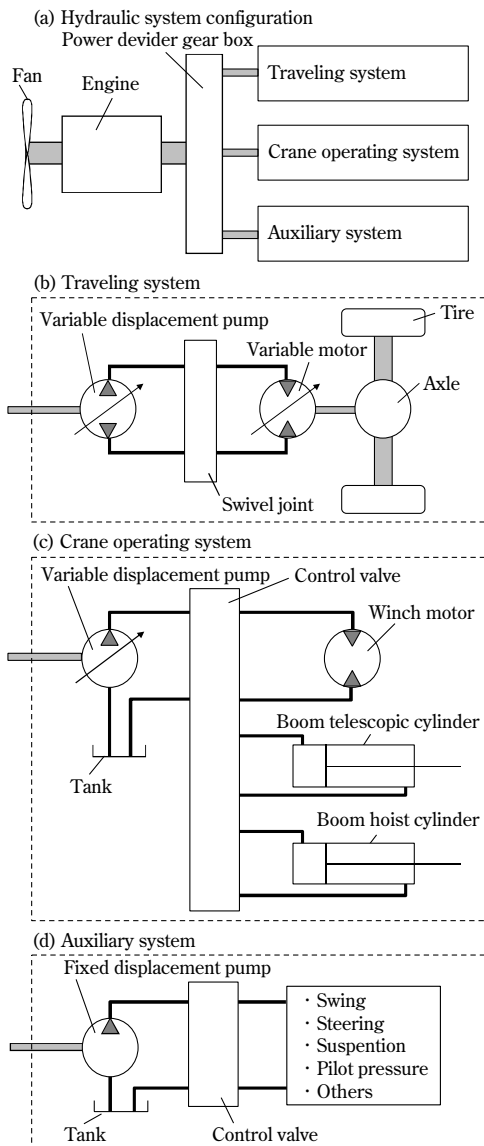
Fig. 1 Hydraulic system configuration of wheel crane

speed of the actuators. Unlike the oil in the HST unit, the oil discharged from the actuators passes through the control valves and returns to a hydraulic oil reservoir.
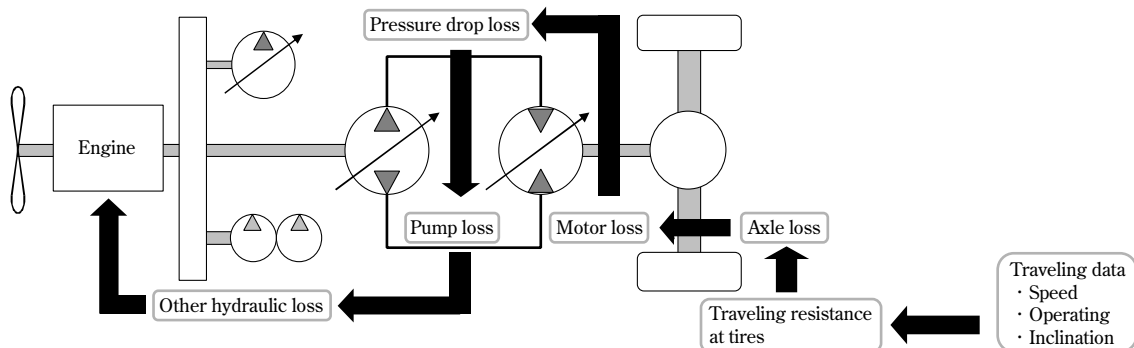
2. Predicting driving fuel consumption by simulation

Prediction by simulation is useful when adopting a new system and it also serves to shorten the time taken by development and specification changes. KOBELCO CRANES CO., LTD. developed a technology for predicting driving fuel consumption. The technology was, however, only applicable to simple running conditions, such as constant-speed driving. In reality, the running conditions are more complex, involving constant-speed driving, acceleration driving, inertia driving and uphill driving. This called for a simulation technology to predict the driving fuel consumption, using data measured on actual runs. Therefore, a new technique has been developed to calculate the fuel consumption of an engine on the basis of the load imposed on, and the loss caused by, each system device during actual traveling.

As shown in **Fig. 2**, actual measurement data for such factors as vehicle speed and road inclination are used to calculate the running resistance, and to this figure is added the loss caused by each system device. The resulting sum is used to determine the revolutions per minute (rpm) and torque required for the engine and thus to estimate the fuel consumption. Variable smoothing, corresponding to the traveling conditions, was performed on the traveling data to reduce noise, which has enabled the accurate analysis of fuel consumption. The losses caused by the pump and motor were determined by a recursive algorithm based on the Newton-Raphson method. For a pump, the following state equations, (1) to (3), hold:

$$W_p = W_{EG} - W_{add} \cdots\cdots\cdots\cdots\cdots\cdots\cdots\cdots\cdots\cdots \quad (1)$$
$$Q_p P_p = W_p \eta_m \cdots\cdots\cdots\cdots\cdots\cdots\cdots\cdots\cdots\cdots\cdots \quad (2)$$
$$Q_p = q_p N_p \eta_v \cdots\cdots\cdots\cdots\cdots\cdots\cdots\cdots\cdots\cdots\cdots \quad (3),$$

wherein W_p, W_{EG}, and W_{add} represent the power of the pump, engine and auxiliary pump, respectively; q_p is the pump displacement; P_p is the pump pressure; Q_p is the pumping rate; N_p is the rpm of the pump; and η_v and η_m are, respectively, the volume efficiency and mechanical efficiency of the pump. Calculations

Fig. 2 Flow of engine load calculation
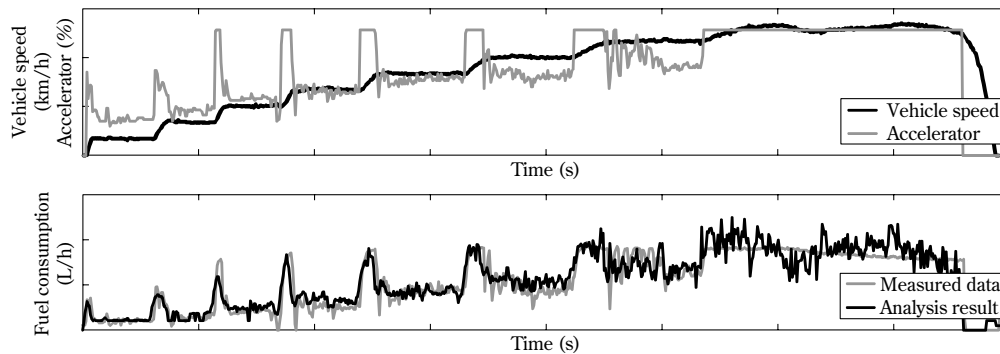
Fig. 3 Comparison of measured data and simulation

were conducted using the pumping rate Q_p as an evaluation function and revolution ω_p as a variable.

To verify the accuracy of this simulation model, the analysis results were compared with the data obtained from an actually running machine, as shown in **Fig. 3**. The traveling data in this figure were obtained for speed increased in a stepwise manner. The results indicate that the analysis accurately reproduces the fuel consumption during acceleration driving and constant-speed driving. The total fuel consumption deduced by the analysis deviates less than 5% from the actual value, verifying the validity of the technique.

3. Improvement of fuel consumption during driving

3.1 Pump displacement control [5)]

During travel, the engine drives not only the pump for the HST unit, but also the pumps and auxiliary pumps for cooling hydraulic oil, for assisting steering and for providing pilot pressure. These pumps are designed with the minimum possible capacities and run unloaded when they are not in use. However, power loss is inevitably caused by the pressure loss of oil as it passes the control valves and piping. **Fig. 4** shows the pressures of unloaded pumps rotating at various rpms. As shown in this figure, the pump pressure increases with an increasing rpm, which raises the burden on the pump. In addition, as shown in **Fig. 5**, the fuel efficiency of an engine is highest when the engine rotates slower than its rated rpm. Therefore, the fuel consumption is effectively reduced by decreasing the rpm. In consideration of these characteristics, a pump displacement control has been developed as described below.

For the pump in the traveling system, a displacement command value is determined for a given rpm according to a function as shown in **Fig. 6**(A). Here, the displacement command value increases with an increasing engine rpm. This is
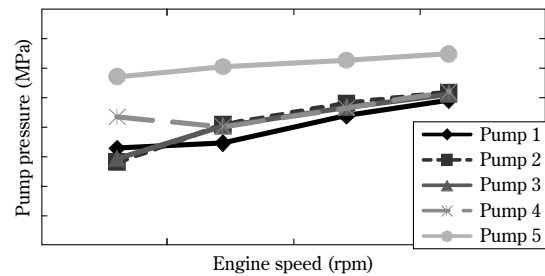
Fig. 4 Unloaded pump pressure
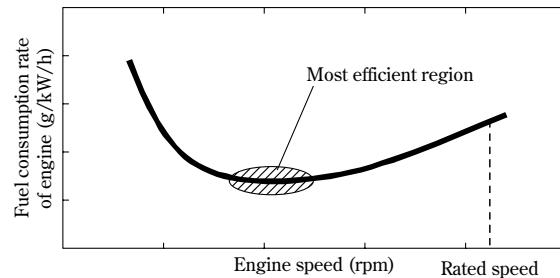
Fig. 5 Engine specific fuel consumption
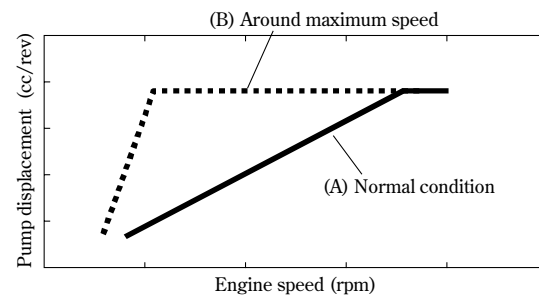
Fig. 6 Pump displacement control

because a large pump displacement at the time of engine start may cause an increased torque to be abruptly imposed on the engine, destabilizing the initial revolution and stalling the engine.

An engine generates increasingly greater power as its rpm increases. When full power is required during, for example, acceleration and uphill-traveling, the engine must operate at a high rpm. On the other hand, traveling on level ground at a constant speed imposes a small load and requires less power, and the engine can run at a low rpm.

The engine rpm, N_E, at a speed V is given by Equation (4).

$$N_E = \frac{q_m \, \varepsilon_{axle} \, \varepsilon_{pd}}{q_p \, \eta_p \, \eta_m} V \quad \cdots\cdots\cdots\cdots\cdots\cdots\cdots\cdots \quad (4),$$

wherein ε_{axle} is the reduction ratio of the axle, ε_{pd} is the reduction ratio of the power divider, q_m is the motor displacement, and η_m and η_p are the efficiencies of the motor and pump, respectively. Equation (4) indicates that decreasing the motor displacement and/or increasing the pump displacement decreases the engine rpm. However, if the pump displacement is controlled according to Fig. 6(A), the pump displacement decreases with the decreasing engine rpm, and the engine rpm may not be sufficiently decreased. Therefore, when the vehicle runs near or at the maximum speed, the pump displacement is controlled according to Fig. 6(B) so as to decrease the engine rpm.

The above control has been adapted not only for speed, but also for acceleration. A displacement control similar to Fig. 6(B) is applied to conditions such as inertia driving and low-speed driving that require a small amount of driving power. The engine rpm has thus been optimized for a wide range of speeds.

Fig. 7 shows the changes in vehicle speed and engine rpm during a test in which the vehicle was accelerated to its maximum speed. The pump displacement was controlled under two different conditions, i.e., the conventional condition (condition 1) and the condition depicted by dotted line (B) in Fig. 6 (condition 2). Although both conditions 1 and 2 yield almost the same vehicle speed, condition 2 resulted in a lower engine rpm for the maximum vehicle speed, which improved the momentary fuel consumption by 11%, verifying the validity of the newly developed control.

3.2 One-way clutch system [6]

A heavy vehicle such as a wheel crane requires a large torque during acceleration and uphill driving. Because the output torque of a motor increases proportionally to the motor displacement, an actual machine must be driven by a large displacement motor, which causes difficulty in mounting. Therefore, an HST unit includes more than one motor. On the other hand, low-load driving (e.g., constant-speed driving) requires only a small motor torque. Thus, a certain amount of energy can be saved by temporarily unloading at least one motor; however, as shown in **Fig. 8**, a loss torque remains even when the motor displacement is set to zero. Furthermore, resistance is caused by the gears rotating with the motor in the mechanical power combiner.

To reduce the idling loss of the motors that are not in use, we developed a system comprising a one-way clutch (hereinafter referred to as "OWC") on the motor axis connected to the mechanical power combiner (**Fig. 9**). The OWC transmits power from motor 2 only in the direction of the mechanical power combiner and prevents any power transmission in the reverse direction. When the displacement of motor 2 is turned to zero during running and no driving force is generated, the clutch is disconnected and the motor stops rotating. For uphill driving and acceleration, the clutch is coupled automatically to drive motor 2 and the power is transmitted in
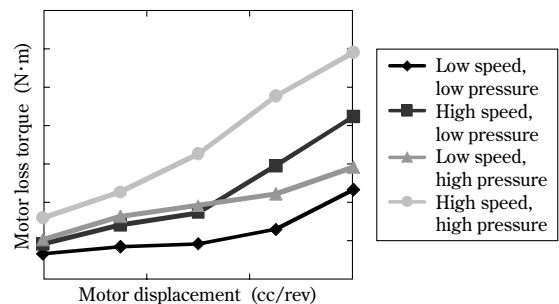
Fig. 8 Motor leak and mechanical loss
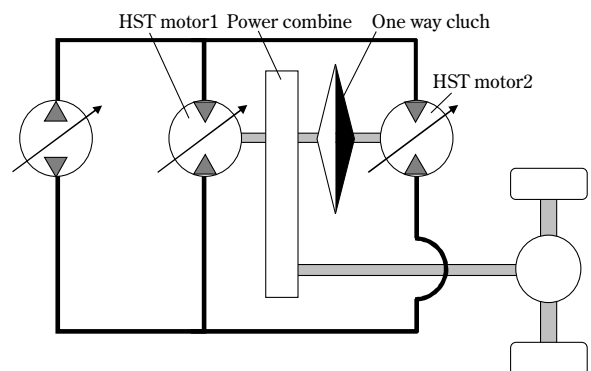
Fig. 9 OWC system configuration

Fig. 7 Effect of engine speed reduction

combination with the power from motor 1. Because the OWC requires neither an actuator, nor a control pressure, nor a signal, a conventional motor mechanism can be adapted for this power transmission system with minimum modification.

A bench test was conducted to verify the effect of the OWC. The result is shown in **Fig.10**. A motor was rotated with zero displacement at different rpms, and the drag torque was measured on the motor axis. The result indicates that the loss torque is decreased to approximately one third in the vicinity of the maximum speed.

The effect of loss reduction by the OWC system was incorporated into the simulation model discussed in Section 2 to analyze the fuel consumption during driving. The result is shown in **Fig.11**. Due to the characteristics of the device, the OWC has no effect until the motor displacement reaches zero, and no improvement is observed in fuel consumption in the low speed region. However, once the high speed region is reached, the motor with zero displacement stops, decreasing the loss and improving fuel consumption. According to a test pattern simulating city driving, the fuel consumption has been found to improve by about 15%. An actual running test

using a prototype vehicle equipped with the OWC resulted in an improvement of 12%, verifying the effectiveness of the system.

4. Improvement of fuel consumption during crane work

4.1 Positive control

During crane work, the speeds of actuators are controlled by control valves. The flow of oil to an actuator is determined by the stroke of a control lever. In a case such as that shown by the curve (C) in **Fig.12**, excess oil, which is discharged from the pump but not utilized for work, is returned to the reservoir. In the case of the conventional pump control (shown by the line of dashes (A) in Fig.12), the pump displacement is constant regardless of the lever stroke, causing a significant loss in the region where the lever stroke is small. A positive control (polygonal line (B) in Fig.12) increases the pump displacement according to the lever stroke, while reducing the loss.

4.2 Lever-sensitive control of engine revolution

Crane work involves the operation of control levers and an accelerator pedal to control the actuators' speeds. The acceleration is controlled according to the type of work and is usually fixed during a job. When a job is performed with full acceleration, the engine is maintained at its maximum rate of revolution regardless of the lever stroke. However, as described in Section 3.1, increasing the engine rpm increases the load imposed on the auxiliary pump, which can deteriorate the efficiency of the engine. Crane work, in particular, consumes a relatively small amount of power compared with traveling, and increased loss has a more significant impact on the fuel consumption.

With this background, a lever-sensitive engine

Fig.10 Shaft resistance in motor
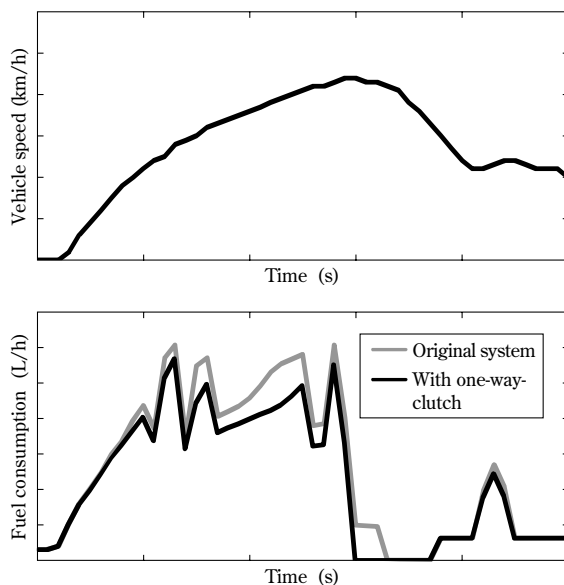
Fig.11 Simulation of OWC system
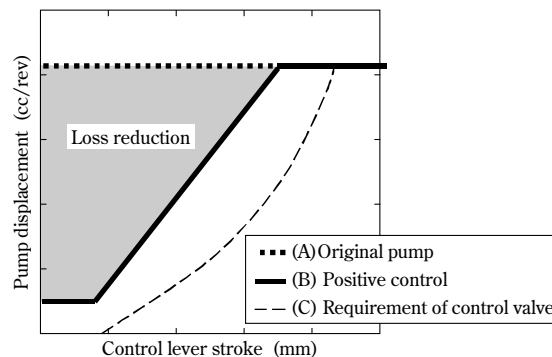
Fig.12 Pump displacement in positive control
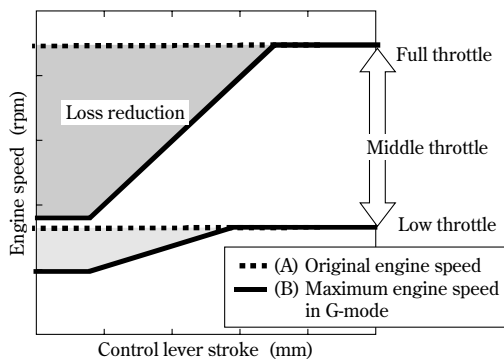
Fig.13 Engine speed in G-mode

Fig.14 Engine speed and fuel consumption in G-mode

revolution control, "G mode" (**Fig.13**), has been newly developed. The G-mode is designed such that the engine rpm can be controlled by small lever strokes and is useful for jobs that do not require speed. Conventionally, the engine rpm has been controlled by an accelerator pedal alone. The newly developed technology enables the levers to control the engine rpm. More specifically, the engine rpm is set either to the allowable rate of revolution corresponding to the lever stroke, or to the rate of revolution called for by the accelerator work, whichever is smaller. This enables the engine rpm to be reduced frequently in coordination with the lever operation, even during full acceleration. Another feature is that the operator can easily control and change the work speed at will, from low to high, simply by operating a lever without using the accelerator pedal.

Fig.14 shows the changes in engine rpm and fuel consumption during actual crane work (combining the operations of winching up/down, moving uphill/downhill and slewing). In this test, jobs other than idling were performed with full acceleration. Job (A) was performed with the lever in the full stroke position. In this case, the engine rpm is comparable with that of the conventional control. On the other hand, jobs (B) and (C) were performed with the levers in partial stroke positions. The result confirms that the engine rpm is decreased significantly by the G mode, and fuel consumption is improved by about 20%.

Conclusions

A new technology has been developed to control pump displacement for a traveling system to improve the fuel consumption of a wheel crane. A one-way clutch (OWC) system has also been developed to reduce motor loss, resulting in a 12% reduction in fuel consumption during driving.

On the other hand, a positive control has been introduced to improve fuel consumption during crane work. We have developed a lever-sensitive engine revolution control, "G-mode", that makes it possible to lower the engine rpm with the lever in a partial stroke position, reducing fuel consumption during crane work by 20%. We will continue to strive to improve the fuel consumption.

References

1) Kagoshima, et.al. *R&D KOBE STEEL ENGINEERING REPORTS.* 2007, Vol.57, No.1, p.66-69.
2) H. Shimokakiuchi. *Kensetsu no Sekou Kikaku.* 2007, No.683, p.37-40.
3) M. Umeda. *Hydraulics & pneumatics.* 1999, Vol.38, No. 5, p. 24-26.
4) S. Abe. *Construction machinery and equipment.* 2011, Vol.47, No.1, p.38-41.
5) *Jpn. Patent.* No.4589979.
6) *Jpn. Unexamined Patent.* No.2011-84094.

Electro-hydraulic Two-Axle Steering System for City Crane

Koichi SHIMOMURA*1, Takashi MORITA*2

*1 Engineering & Development Div. System & Component Development Dept., KOBELCO CRANES CO., LTD.
*2 Electronics Research Laboratory, Technical Development Group

This paper describes a new steering system for a city crane, the RKE450. Unlike conventional fully-hydraulic steering, the new system adapts a mechanical steering system for the front axle and an electro-hydraulic steering system for the rear axles, where the latter system is automatically controlled in accordance with the movement of the front axle. In addition to the safety feature carefully built into the control system, the new steering system also achieves low tire wear, better driving stability, and a smaller turning radius. As a result, the crane complies with the European regulations for driving on public roads at speeds as high as 80km/h and has several auxiliary functions for crane actions in the off-road mode at speeds below 25km/h, as required by the regulations.

Introduction

A new city crane, the RKE450 (**Fig. 1**), is now on the European market. When the machine was being developed, it was essential to make the steering mechanism comply with European regulations. The model that is the Japanese counterpart of this new crane has conventionally employed a hydraulic steering mechanism that does not comply with the European regulations. Therefore, a new system has been developed, comprising front and rear axles, in which the front axle is mechanically steered and the rear axles are automatically steered electro-hydraulically in accordance with the amount of steering done by the front axle.

This has led to the establishment of a new steering system that has been proven to be safe and that can be driven on European motorways, with its features of minimal tire wear, high running stability and a small turning radius. The following describes the details.

Fig. 1 Photograph of RKE450

1. Conventional steering mechanism for Japanese models

A standard city crane, which is classified as a large-sized special motor vehicle in Japan, is equipped with two steering modes: i.e., a normal mode that is used for driving on public roads, during which time the steering is performed only by the front axle, and a special mode (including "clamp", "crab" and "rear", as shown in **Fig. 2**), which decreases the turning radius when driving on non-public roads and on work sites. The cab, from which the steering is directed, is located on the crane's upper slewing body, while the mechanism that actually steers the axles is located in the lower traveling body. This steering configuration makes city cranes different from ordinary automobiles. We have adopted hydraulic steering systems (**Fig. 3**) along this line for over 30 years. Each hydraulic steering system comprises an all-hydraulic power-steering control unit, rather than using mechanically linked steering systems. The hydraulic control unit converts the driver's steering operation

Fig. 2 Steering mode

All hydraulic power steering control unit

Steering wheel

to tank | from pump

Swivel joint

Selector valve of steering mode
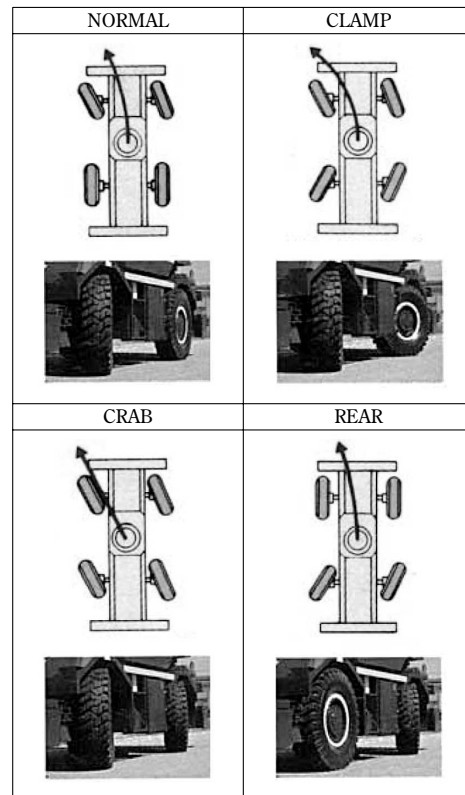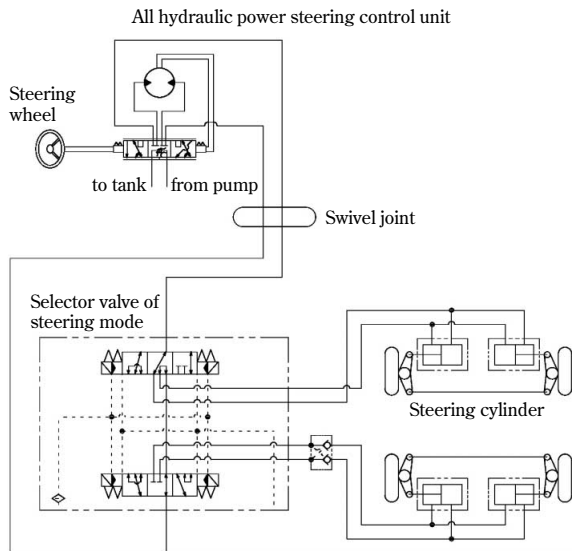
Steering cylinder

Fig. 3 Hydraulic Steerage mechanism

into oil pressure, transmits the pressure from the upper slewing body to the lower traveling body via a swivel joint, and, thus, hydraulically actuates steering cylinders to complete the steering. Switching between the normal mode and special mode is accomplished by an electromagnetic switching valve that changes the hydraulic circuit as the controller detects the driver's actions and makes a judgment in accordance with various switching conditions.

In the normal mode, the hydraulic circuit actuates only the front axle (while the rear axles are in a hold state). In the special mode, the hydraulic circuit actuates both the front and rear axles such that they cooperate in steering the vehicle. However, not having a mechanically-linked steering mechanism for driving on highways, this construction is deemed not strong enough to satisfy the requirements of European regulations for driving on public roads.

2. Steering mechanism for the newly developed RKE450

2.1 Construction of the steering mechanism

In the newly developed RKE450 (hereinafter referred to as the "present machine"), the front axle is mechanically linked, through a lower steering mechanism, with the steering wheel in the cab such that the driver's steering operation is directly transmitted through the link mechanism. The rear axles (i.e., second and third axles), on the other hand, are controlled and driven electro-hydraulically. Electromagnetic switching valves (hereinafter referred to as "check valves") are used to allow steering and related operations, while electromagnetic proportional valves are used to adjust the amount of steering based on the command from an electrical controller (**Fig. 4**). Steering angle sensors detect the angle to which the driver moves the front axle in steering. The controller automatically calculates the degree of steering for the rear axle(s) in accordance with each steering mode. The degree of steering applied to each rear axle is also detected by steering angle sensors, and the result is used to determine the command.

In the above construction, the front and rear axles are not linked, either mechanically or hydraulically; this increases the degree of freedom in rear-axle steering. Therefore, an adequate control can decrease tire wear and the turning radius, increasing the appeal of the product. This structure, however, is quite different from that of the conventional domestic model, whose front and rear axles are hydraulically linked and always have a synchronized relationship. In the new construction, a failure of the electronic control (due to some anomaly, or to component
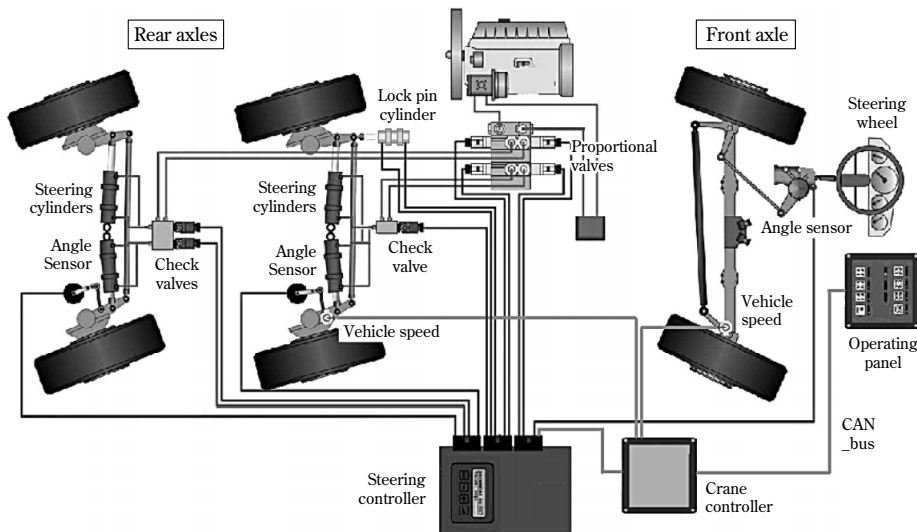
Fig. 4 Diagram of steering system of RKE450

failure) may cause an unsafe event, in which the rear axle steering does not cooperate with the front axle steering. Therefore, as described later, safety was given prime consideration in developing the present machine, resulting in the further enhancement of its safety over that of the conventional machine.

2.2 Steering modes

The present machine comprises a "highway mode" for running on public roads and an "off-road mode" for running on non-public roads.

The highway mode ensures the running stability required for high-speed driving of up to 80km/h and controls the steering of each axle independently to reduce wear on the tires on the rear axles. (The model that is its domestic counterpart does not have this independent steering control.) The second axle is kept in a neutral state, while the third axle is automatically steered in accordance with the steering angle of the first axle (**Fig. 5**).

In the low-speed range where the vehicle is moving at no more than 10km/h, steering is controlled such that the center of the turning circle always falls on the line that extends the axis of the second axle. This minimizes tire wear during steering and decreases the turning radius. The center of this turning circle is uniquely determined from the steering angles of the first and third axles and from the axial distance, pre-stored in the controller, of the actual machine. The controller calculates the steering angle of the third axle for the automatic steering control on the basis of the steering angle of the first axle, an angle that is constantly being changed by the driver's operation.

In the high-speed range where the speed of the vehicle is greater than 30km/h, running stability is ensured by keeping both the third and second axles in the neutral state, regardless of the steering angle of the first axle. This steering is specified on the basis of two aspects: The effect on tire wear is negligible in the high-speed range, and a small change in the steering angle significantly affects the direction (directional

stability) of the vehicle body and its safety. In order to suppress tire wear, the speed control is more advantageously switched at a higher threshold. The threshold speed of 30km/h, thus determined, is higher than that of the other vehicles already in the European market (25km/h), and its safety has been well established by demonstrations using actual machines.

In the mid-speed range above 10km/h and no higher than 30km/h, the steering angle of the third axle changes, proportionately to the speed, from the angle that has been set for the low-speed range, until it reaches the angle for the high-speed range. This change is made in such a way that the driver does not feel any difficulty in steering the rear axle.

The off-road mode, rather than limiting the vehicle speed to a maximum of 25km/h to comply with the European regulations, serves for special steering, including all-wheel steering, crab steering, and manual steering, thus ensuring mobility under the various limiting conditions of the work sites. This mode enables the second axle, which is kept in neutral when in highway mode, to steer the vehicle, thus taking full advantage of the steering performed by all the axles.

The all-wheel steering minimizes the turning radius. The steering angles of the second and third axles are automatically controlled such that the center of the turning circle always falls on a line extending from the center axis of the vehicle body. Crab steering optimizes the pull-over operation by automatically controlling the steering angles of the second and third axles so that they are equal on the basis of the steering angle of the first axle. Manual steering uses a switch that is separate from the steering wheel to steer the rear axle. The switch makes it possible to steer the second and third axles independently of the first axle such that the phases of the front and rear axles can be determined independently according to various limiting conditions (**Fig. 6**).

2.3 Safety considerations

2.3.1 State detection

Detecting the steering angle of each axle is extremely important in maintaining the accuracy, safety and reliability of the system. The detection of steering angles is particularly important from the aspect of safety. A mismatch between the detected and actual steering states can cause a steering operation that is totally unexpected and can immediately lead to a serious accident.
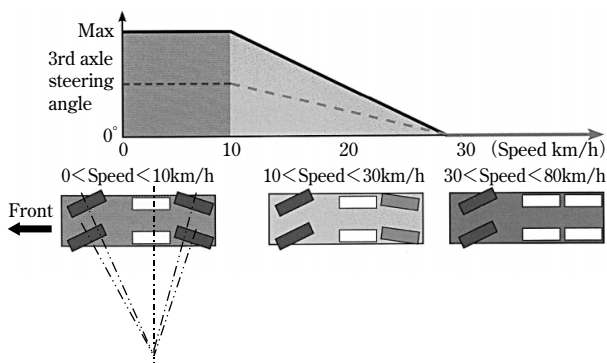
With this in mind, the detection of the steering

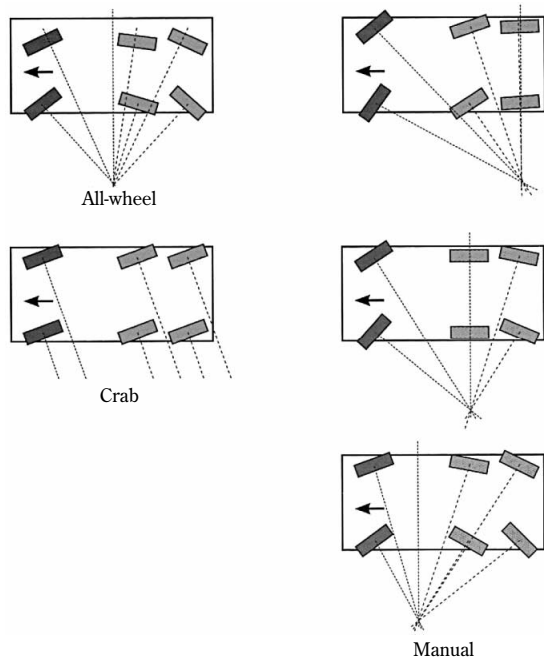Fig. 5 Steering system in on-highway mode

Fig. 6 Steering system in off-road mode

Fig. 7 Signal of steering angle sensor

angle has been devised with special care and taken to a higher level than that of the state detection in the conventional domestic model. As a natural procedure, a duplexed system is employed for signal detection in a manner similar to that of other critical state detections, such as the detection of accelerator operation. The duplexed signals, however, may both be distorted in the same manner by a disturbing factor. Redundancy by cross-sensing is adapted to prevent this problem from happening and to further improve reliability (**Fig.7**). There is a risk that one or both of the duplexed signals may not reflect the actual value even when the signals are in the normal range (or in a range that is beyond the upper or lower limit of the sensor voltage, but does not reach the failure range). This happens when, for example, something causes the supply voltage for the sensor and/or the electrical potential level of the grounding to deviate from the normal range. This problem happens also when unintended powering or a ground fault occurs on the signal line. The above configuration makes it possible to judge anomalies even when such problems occur. In the newly developed system, one of the duplexed signals is taken as a base. An anomaly is judged to have taken place when the other signal is converted into an angle that exceeds ±10% of the range of the base value. If this happens, the values are not used for the control, and the system is shifted to a failure procedure.

Vehicle speed signals from the speed detection sensors are also critical because they are used for calculating the steering angle and mode switching conditions when in highway mode. Vehicle speed

signals are used not only for the steering control, but also for other controls. In a conventional machine, two sensors are provided, i.e., a main sensor on the rear axle and a sub-sensor on the front axle. The steering controller receives input via dual channels, i.e., a direct input of pulse signals from the rear axle and an indirect input via a Controller Area Network (CAN) from the front axle, in which the signal passes through other controllers. Unlike ordinary anomaly detection, the signals from the dual channels are compared and an anomaly is judged to exist when the difference exceeds a predetermined value. The signals are not used by the control and are shifted over to a failure procedure.

2.3.2 Steering operation

Even if the above described state detection returns a normal result, a steering operation that is totally unmatched with the driver's steering actions may occur when there is an anomaly in the electrical output from the steering controller or in the hydraulic actuators receiving the electrical output. Therefore, special care has been taken to devise duplex channels, not only for the electrical system, but also for the hydraulic system (Fig.4).

The system is configured around the basic concept that the rear axle must never act on its own when in highway mode. (In particular, it must remain in neutral in the high-speed range.) This basic concept takes precedence over everything else. For each of the rear axles, i.e., the second and third axles, the steering operation is determined by the strokes of two cylinders whose movement is governed by the output from the steering control valve (proportional valve), which is actuated on the basis of commands from the steering controller. The proportional valves are disposed facing each other on both sides of each control valve and are constructed so as to maintain the steering state unless there is an electrical output. In other words, when the outputs from the

proportional valves are equal (including zero outputs), the control valve enters the neutral state and the steering cylinders are kept in the hold state.

Due to sticking (e.g., by seizure of the spools), or due to electrical anomalies, the hydraulic output of a steering control valve (proportional valve) may work on the unsafe side. In case of such an emergency, the steering state is maintained by the hydraulic circuit configured in a duplex manner. This enables the steering controller to detect an anomaly, and the check valves that are provided in front of the steering cylinders are actuated to shut down the circuit in order to maintain the state of the steering cylinders. These check valves themselves are configured to open the hydraulic circuit and to make the steering cylinders operable when an electrical signal is output. It should be noted that a check valve is provided for each steering cylinder of the third axle so that the steering cylinders are not actuated if one of the check valves fails to operate. For the second axle, only one check valve, common to both of the steering cylinders, is provided. Instead, to ensure a neutral state when in highway mode, a mechanical locking mechanism (including lock pins) conventionally used in the domestic model is provided, in addition to the hydraulic holding mechanism. A pneumatic lock cylinder actuates a pin to lock the steering cylinder.

As for the electrical aspect, the feedback from the proportional valve output is monitored as in the case of the domestic model, and the operation shifts to a failure procedure as soon as an anomaly is detected. The electrical output to each check valve is configured such that the outputs of both the high side (power supply side) and the low side (grounding side) come from the steering controller. As a result, there is only a negligibly small possibility of a check valve's failing to hold the steering cylinder due to an electrical problem.

2.3.3 Fail-safe procedure

A fail-safe procedure has been devised to prevent an unsafe event from happening in the event that an anomaly should occur in the state detection, steering controller, or output system. Anomalies are categorized in four levels, according to their importance, from Level 0 (minor) to Level 3 (major). The steering controls on the second and third axles are limited in certain ways, depending on the level, to prevent major unsafe events, while, as far as possible, keeping the steering function effective (**Table 1**).

In Level 0, the normal control is continued. In Level 1, an axle affected by an anomaly is steered by the driver until the axle goes into neutral and,

Table 1 Definition of fail-safe

Error level	Axle2				Axle3			
	No effect	Lock next center	Move to center	Lock actual	No effect	Lock next center	Move to center	Lock actual
System level0	○				○			
System level1		○				○		
System level2			○				○	
System level3				○				○
Axle2 level0	○				○			
Axle2 level1		○			○			
Axle2 level2			○		○			
Axle2 level3				○		○		
Axle3 level0	○				○			
Axle3 level1	○					○		
Axle3 level2	○						○	
Axle3 level3		○						○

thereafter, is held in neutral. In Level 2, only the axle affected by the anomaly is forcibly steered into the neutral state and, thereafter, held in neutral. In Level 3, the axle affected by the anomaly is immediately shifted to a hold state, while the axles that are not directly affected are steered by the driver until they enter the neutral state and, thereafter, are held in neutral.

2.3.4 Verification of safety

Just as in the case of conventional development, the new control system was established after the verification of control specifications by testing on bench and actual machines, as well as by a thorough confirmation of their behavior under each failure mode as defined by Failure Mode and Effects Analysis (FMEA). The typical verification items are as follows.

The steering mode performance for the operation of a normal system is verified. Above all, straight-line stability is regarded as an important factor. The specifications require that the rear axle in the neutral state must be aligned within +/- 0.3 degree. Testing on an actual machine under various conditions has proved that the actual alignment falls within +/- 0.15 degree.

It is most critical to verify the behavior under failure. Verification based on FMEA, including the effective use of accumulated data, was performed with the cooperation of a steering system manufacturer.

For the sake of safety and for compliance with European regulations, a swing-out test is a particularly important part of the verification process. The test includes checking the amount of swing-out when the rear part of the vehicle body sways from side to side due to an abrupt change in the steering angle of the third axle. This behavior of the third axle is regarded as the worst case in the

FMEA (unintended powering of the steering control proportional valve line). European regulations require the amount of lateral sway to be less than 10% of the vehicle width (or about 255mm for the present vehicle). On the other hand, the amount measured in the early stage of development was about 300mm, which was not acceptable. It took about 220ms from point at which the fail state of the proportional valve output was detected until the check valve was actuated to cease the steering operation of the third axle. During this period, the steering angle changed by about 5.4 degrees. A study of the response time revealed that the hydraulic response was dominant. Therefore, the specifications of the check valve and proportional valve were revised to improve the hydraulic response while maintaining steering accuracy under normal operation. In the resultant final product, the steering angle during the swing-out test has been held to 1 degree, with a thoroughly acceptable swaying amounting to several tens of millimeters.

Another test that is important from the aspect of safety and compliance with European regulations is the verification of the evacuation operation if the third axle should become locked at the maximum steering angle while in highway mode. This test verifies whether or not the vehicle can be driven for a certain distance for the sake of evacuation in the event that the third axle has been steered to the maximum angle and is locked there due to an anomaly. The present vehicle was set to the highway mode with its third axle fixed at its maximum steering angle of 19 degrees. In this state, the vehicle was driven straight, using only the steering operation of the first axle. Even though this was not easy, the evacuation of the vehicle was deemed to be possible (**Fig.8**).

Fig. 8 Fail test

Conclusions

Electronic controls will be increasingly used, not only for city cranes, but also for other mobile cranes, including crawler cranes, to improve their product competitiveness by providing high-function, high-performance features. Special care was taken during this development to assure fail-safety and reliability when constructing and implementing such a system, and such care will be essential in future development as well. We will continue to provide products having balanced features of function, performance, safety and reliability.

Technology for Evaluating Strength, Stiffness, and Riding Comfort of Crawler Crane Cabins

Kiyotsuna KUCHIKI*1, Hideaki HOSOI*1, Masashi KAWABATA*2, Yoshimune MORI*2
*1 Engineering & Development Div. System & Component Development Dept., KOBELCO CRANES CO., LTD.
*2 Mechanical Engineering Research Laboratory, Technical Development Group

Evaluation technology based on simulation analyses of the strength, stiffness and riding comfort of cabins has been applied in the development of wheel and lattice boom crawler cranes prior to production. This front-loading evaluation technology was found to be precise and effective in reducing the amount of backtracking necessary to finalize the structure. The technology has been developed in association with the Mechanical Engineering Research Laboratory, Technical Development Group, Kobe Steel, Ltd.

Introduction

In the recent tough economic climate, it has become increasingly important to develop low-cost, high-quality machines in a timely fashion. The mobile cranes (hereafter, "cranes"), as shown in **Fig. 1**, manufactured by KOBELCO CRANES CO., LTD. are not exceptions. Furthermore, transport regulations under the Road Traffic Act are becoming even more stringent, requiring the machines to be smaller and lighter.

To satisfy such requirements, the machines are given demanding performance goals on a per-element basis. Cabins are conventionally required to be lighter and stiffer. In addition, they are now required to have structures rationally designed for reducing material and fabrication costs. Lean and effective design is also required to shorten the lead time for development.

Appearance design, although important in making the products stand out in the market, often conflicts with the goal of lighter and stiffer structures. The key is to balance the appearance with the structure, while maintaining high quality.

It should be noted that the term, "cabins", as used in this paper, refers to the compartments located on the main bodies of cranes, where workers operate the machines.

One approach to developing a cabin is to build a mock-up, which is repeatedly modified until the requirements are met. Another approach includes a careful prior examination using a full numerical analysis to resolve issues to the extent possible before making a product, after which the performance is verified.

The mock-up approach was taken in the days when numerical analysis was still technologically immature, yielding unreliable results, and creating an analysis model took an enormous amount of time. The mock-up approach, however, may suffer from inefficiency when significant modifications of its structure are required and cannot be accomplished by simple alterations. In such cases, the mock-up must be rebuilt. Enormous time and money are required for this modification, which limits the thoroughness of the evaluation.

Lately, the advancements in computer performance and analytic technology have significantly improved the accuracy and reliability of analysis results. Recent preprocessors with improved performance and enhanced functions have enabled analysis models to be created easily and fast enough for practical applications. In addition, the trial-and-error method based on numerical analysis facilitates large-scale structural alteration to a greater degree than the mock-up approach. Although the performance verification of prototype machines is still necessary, the time and money required for the development, as a whole, have been significantly decreased. For this reason, more importance is being placed on prior evaluation based on numerical analysis, not only in the crane industry, but also in the manufacturing industry as a whole.

At this time, we have developed new cabins for wheel cranes and general-purpose crawler cranes by adopting prior evaluation technologies based on numerical analysis. These technologies have been developed in cooperation with the Mechanical Engineering Research Laboratories, Technical

Fig. 1 Latticed boom crawler crane

Development Group, Kobe Steel. The following introduces some case examples.

1. Performance requirements for cabins

A cabin must be strong enough to withstand the external forces that are applied during operation and transportation. Another requirement is riding comfort, which is determined by the vibration felt by the driver during the operation of the crane. Other important elements of performance include the operator's viewing field and the amenity of the cabin space. The strength performance of the cabin is best improved by constructing it with thick pillars and small windows. This construction, on the other hand, has adverse effects on operability and amenity for the operator. In other words, strength performance and riding comfort requirements conflict with the viewing field and amenity offered by the cabin space.

In order to achieve all that is required in the way of performance, it is necessary to satisfy all requirements at a high level of quality and in a balanced manner, with a sophisticated structure.

2. Evaluation procedure for cabins

Fig. 2 is a flow chart depicting the procedure followed in developing a cabin, to evaluate strength, stiffness and riding comfort.

The mainstream of conventional development practices relies on modeling based on bench tests and testing on actual machines. This new method of development attempts the front-loading of the evaluation process to enrich simulation analysis and evaluation.

The following explains the evaluation method followed for each developmental stage.
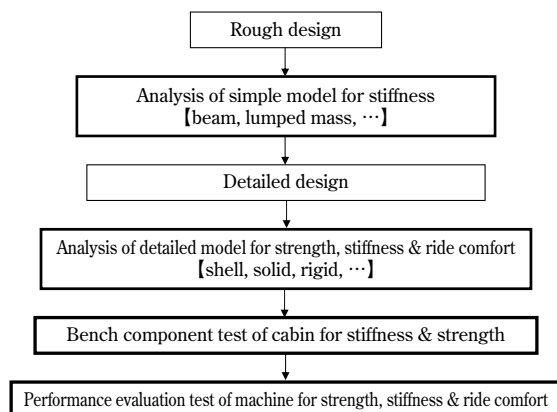
Fig. 2 Evaluation flow chart for cabin strength, stiffness & riding comfort

2.1 Unit test for cabins

2.1.1 Simplified analysis

A simplified analysis is used to evaluate the dynamic stiffness of the entire cabin system. After a machine design has been determined, dynamic stiffness is incorporated into the design. Prior to the detailed designing, and when the external dimensions have been determined, an eigenvalue analysis of the entire cabin system is performed using a simplified analysis model consisting of beam elements, concentrated mass and shell elements. This analysis provides rough estimates for the construction of main structural members and the cross-sectional performance required to achieve the target dynamic stiffness. The result of this analysis is used as a base for the detailed designing. The analysis employs a general purpose, finite element analysis code, MSC/NASTRAN.

Fig. 3 depicts a simplified analysis model, and **Fig. 4** is a result of an eigenvalue analysis.
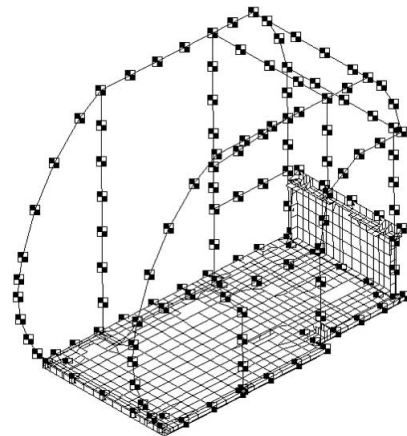
Fig. 3 Simple analytical model
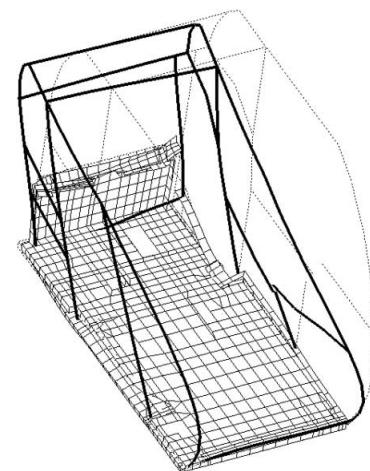
Fig. 4 Mode shape of cabin

2.1.2 Detailed analysis

The detailed analysis evaluates the dynamic stiffness of the entire cabin system, as well as the dynamic stiffness of panels and the fatigue strength.

KOBELCO CRANES CO., LTD. conducts detailed designing based on 3D modeling using a 3D-CAD system. The 3D modeling is used to prepare wire frame models, which shorten the time required for compiling the analysis data. The 3D-CAD system includes, in addition, an FEM analysis function. The analysis function may be used to further save time. In the case of the cabin, however, the types of available elements are limited, and there is no element that yields satisfactory accuracy for a structure consisting of plates and shells. Therefore, the MSC/NASTRAN is being used as an analysis tool for the moment.

The analysis model was prepared using various elements, such as shell elements, solid elements and rigid elements, as shown in **Fig. 5**. Spring elements are used for portions such as bolt joints and plate joints, which have non-linearity and are difficult to mold. Equivalent spring constants are provided based on the actual results of conventional analyses.

In the detailed analysis, the eigenvalue of the entire cabin system is first analyzed for structural validation to see if the natural frequency of the subject mode is no smaller than the target value (**Fig. 6**). The nominal strength of the main structure is usually obtained at this time. Also evaluated are the dynamic stiffness of the floor plate, which affects vibrations and, hence, the riding comfort, and the dynamic stiffness of the side and rear cabin panels, which affect the noise in the cabin (**Fig. 7**).

Next, the fatigue strength is evaluated by a static stress analysis, applying unit acceleration, and by a frequency response analysis, applying an external force that is deduced from the actual measured force acting on the cabin. In order to increase the accuracy of the evaluation, the stress is evaluated not only in an absolute value based on the S-N curve, but also in a relative value compared with the stress exerted on conventional cabins that are actually in use [1].

The analysis results are used to determine the shapes of detailed parts.

2.2 Dynamic stiffness analysis of entire mechanical system

A cabin is subjected to vibration across a wide frequency range. The vibration is transmitted from various sources, including the engine, which vibrates due to internal explosion and rotation, and pumps and other hydraulic devices that pulsate. Such vibration is transmitted to the operator through the
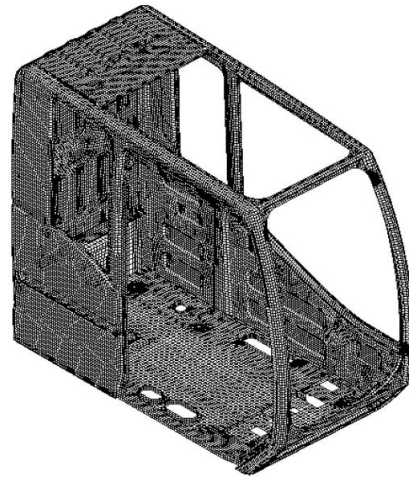

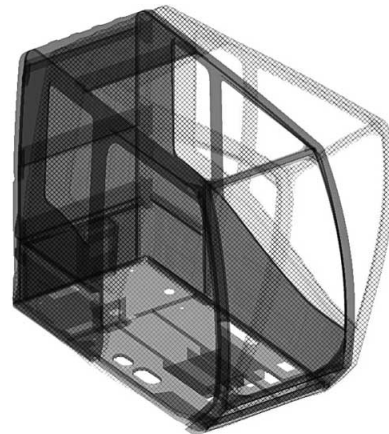
Fig. 5 Finite element model

Fig. 6 Mode shape of cabin

Fig. 7 Mode shapes of rear panel

seat and floor plate, shaking the crane operation lever, monitor, and panels and causing discomfort to the operator. To alleviate such discomfort, the cabin is attached to the crane body via an anti-vibration
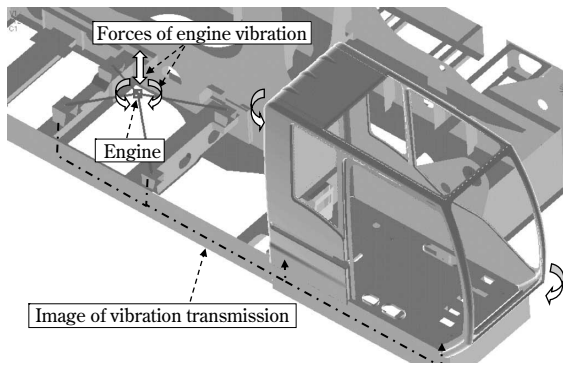
Fig. 8 Image of frequency response analysis

mount.

In order to dissipate the vibration transmitted to the cabin, the anti-vibration performance of the mount must be exploited. This is factored into the stiffness target for the entire cabin system. However, the stiffness of the cabin itself is not the only factor that counts in achieving the full potential of the anti-vibration performance. The stiffness of the frame of the crane's main body, which supports the cabin, is also important.

So far, the stiffness of the crane's main body has been evaluated statically (static stiffness evaluation). However, the requirements for weight reduction and the like, call for a more accurate assessment. In response to this need, a dynamic stiffness evaluation is being employed [2].

The dynamic stiffness evaluation includes a frequency response analysis to determine the response acceleration of the cabin that is subject to an exciting force at the position of a vibration source such as an engine (**Fig. 8**). The analysis model encompasses the entire system of the crane, including the cabin and mount.

There are a number of issues related to the analysis accuracy and evaluation technique in this analytical evaluation. The issues include:
・ the modeling area of elements existing in the machine;
・ nonlinear characteristics, such as back-lash and the mount; and
・ the quantification of the operators' sensory evaluation of the vibration.
Studies are being conducted to resolve these issues.

3. Test and evaluation

3.1 Stiffness and strength evaluations using a prototype cabin

Before assembling a prototype machine including the crane's main body, a prototype cabin is made for a bench test to evaluate its dynamic stiffness

and fatigue strength. For dynamic stiffness, a modal measurement is conducted using an impact hammer, as shown in **Fig. 9**. The natural frequency and eigenmode of the prototype cabin, thus obtained, is used to determine whether or not the target dynamic stiffness has been attained.

Fig.10 shows an example of the response results obtained by the impact test performed on the prototype cabin. **Fig.11** is a diagram showing the deformation in the vibration mode at the peak

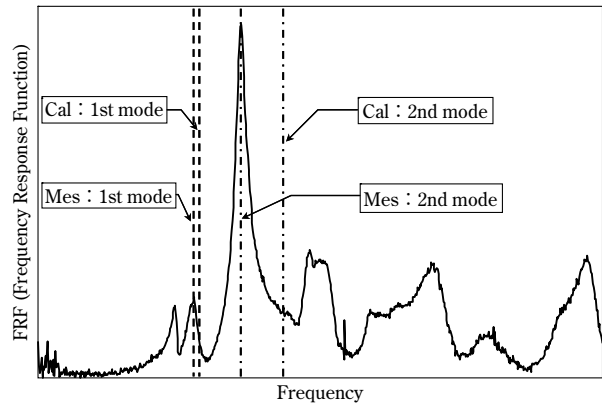Fig. 9 Impact hammer testing of cabin

Fig.10 Result of impact hammer testing
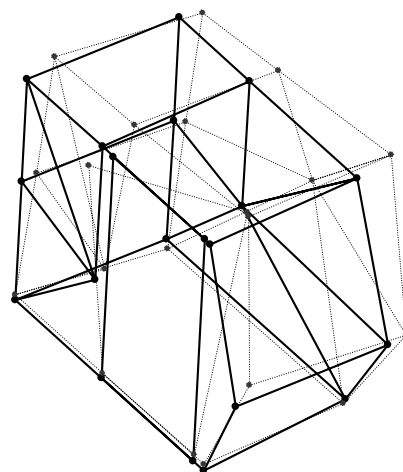

Fig.11 Mode shapes of cabin

Fig.12 Shaker testing of cabin

frequency. This result has been confirmed to match well, in terms of frequency and deformation mode, with the results (Fig. 6) of the analysis of a detailed model. Results that are consistent with the prior analysis were obtained for panel stiffness, such as that of the rear panel.

Next, a vibration bench test (**Fig.12**) using a shaker was conducted to evaluate the strength of the prototype cabin. In order to shorten the test time, an accelerated test was conducted under vibration conditions (time, vibrating force) that make the damage equivalent to the life-time damage estimated from the vibration data measured on an actual machine. Cracks were detected by color checks. For each location where the prior FEM analysis had indicated a concern about strength, stress was measured using a strain gauge to verify conformity with the results of the FEM analysis.

With the substantial prior analyses using FEM, the prototype machine passed the vibration durability test in its first trial without any modification.

3.2 Performance testing and evaluation using actual machine

Actual machine performance testing was conducted to confirm the dynamic stiffness (natural frequency and vibration mode) mainly by modal measurements, to measure the cabin vibration during actual operations and to evaluate the riding comfort as reported by the operator. In principle, the strength evaluation is completed during a bench test. For some machines, rough road durability tests are still being conducted to evaluate the strength of their cabins, but these tests are gradually being replaced by bench tests.

In this development, the evaluations of strength and stiffness were front-loaded. As a result, no problem was found during the actual machine performance testing–neither in the strength, nor in the riding comfort of the cabin. Furthermore, as a result of the prior evaluation of the dynamic stiffness of the panels, the interior noise of the cabin is kept within the development target without any modification, which has contributed to the shortened development time.

Conclusions

The advancement of simulation analysis technologies has enabled highly accurate evaluations of dynamic stiffness and fatigue strength in the designing stage of newly developed cabins. This has reduced the need for modifications after building prototype machines and shortened the development time.

The substantial front-loading has extended the time required for analytical evaluations; however, linking the evaluations with the 3D design has shortened the overall time.

The virtual prototype approach is now prevalent world-wide; it is an approach in which all factors, including behavior as a whole and component life, are evaluated by numerical analysis. The trend is toward going "prototype-less" and performing evaluations that do not involve prototype machines.

KOBELCO CRANES CO., LTD. will continue to strive to further improve analytical accuracy and to brush up the technologies for prior analytical evaluations by expanding the object scope to achieve "prototype-less" evaluation to the extent possible.

References

1) S. Kawabata, et al. *R&D KOBE STEEL ENGINEERING REPORTS.* 2007, Vol.57, No.1, p.58-61.
2) E. Imanishi, et al. *R&D KOBE STEEL ENGINEERING REPORTS.* 2001, Vol.51, No. 3, p.50-57.

Nondestructive Measurement of Earing Using an Electro-Magnetic Acoustic Transducer

Toshihide FUKUI[*1], **Yasuhiro WASA**[*1], **Kazutaka SHIGEOKA**[*2]

[*1] Production System Research Laboratory, Technical Development Group
[*2] SHINKO INSPECTION & SERVICE CO., LTD.

A highly accurate acoustic velocity measurement system using an Electro-Magnetic Acoustic Transducer (EMAT) has been developed in order to evaluate the texture of aluminum plates. A good correlation between acoustic velocity anisotropy and earing is found for various kinds of aluminum plates, and earing can be estimated to be at 0.5% by measuring the anisotropy of the acoustic velocity. This system is applicable to inline inspection and all-length inspection, and can replace the conventional offline destructive measurement.

Introduction

Many common products such as drinking cans, food container lids, pots and pans and aluminum hubcaps are made of deep drawn aluminum sheets. Since these products are made by embossing (cup-molding) aluminum sheets several times, uniformity and isotropicity in plastic deformation of aluminum sheets, in addition to sheet thickness, become crucial. Generally, cup edges develop unevenness called "ears." Since "earing" represents the dimensional ratio of an ear, it has correlations with product yield and potential production line troubles during and after molding processes. Therefore, it is counted as one of the quality assurance items for deep drawing materials.

Since texture in the material is the cause of earing, Kobe Steel, as a material manufacturer, has been striving to improve the material quality by controlling texture in relation to rolling and heat treatment conditions. However, the quality assurance cannot be extended to all units or all lengths, since the texture control is performed by offline observation and analysis. This report describes a technology we developed for predicting post-process "earing" by measuring ultrasonic anisotropy at high precision through non-contact ultrasound aided by an electromagnetic acoustic transducer.

1. Cause of earing

Once shipped, aluminum sheets are processed into designated cup shapes, by going through molding processes such as punching, deep drawing using dies and punches and ironing/spatula ironing. Retightenable bottlecans that came into the market recently are a typical example. **Fig. 1** shows the simplest deep drawing processing of aluminum sheets and a commonly used standard measurement method for ears and earing. A circular sample was punched out of an aluminum sheet and was deep-drawn, to measure an uneven ear at the edge of the can. Its height was measured at 45 degree angle increments, with the direction of rolling being 0 degree, to define value of the earing ratio using equation (1).[1]

$$\text{Earing} = \frac{(H_{45} - H_{0-90})}{(H_{45} + H_{0-90})/2} \times 100 (\%) \quad \cdots\cdots\cdots\cdots(1)$$

In this equation, H_{0-90} represents average ear height of four directions including directions of rolling and width directions, and H_{45} represents average ear height of four directions in increments of 90-degree angles starting at 45 degrees away from the rolling direction. There are two types of ears, namely "negative ear," an ear protruding in the rolling direction (0 degree) or its orthogonal direction (90 degrees), and "positive ear," an ear protruding in 90-degree increments starting from 45 degrees away from the rolling direction. Conceptual drawings of these two ear types are shown in **Fig. 2**.

Cause of earing is known to be texture in an aluminum sheet[2,3]. While atoms and molecules are lined up in an orderly fashion with monocrystalline materials, thereby causing anisotropy, with polycrystalline materials, its anisotropies end up cancelling out each other making the material isotopic on a macro level. However, even polycrystalline metal sheets may develop texture
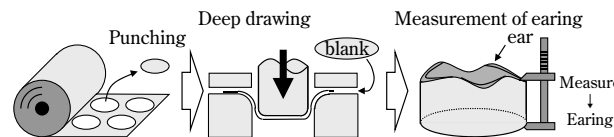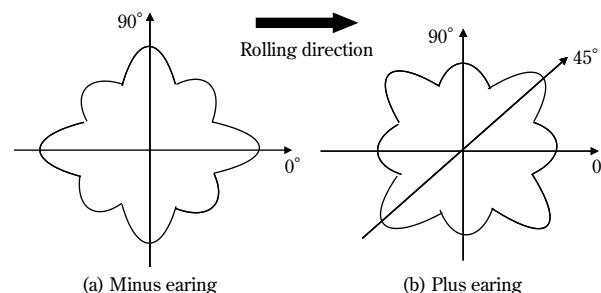

Fig. 1 Deep drawing and earing

(a) Minus earing   (b) Plus earing

Fig. 2 Two types of earing shape images

from developing skewed crystal orientation through processing and heat treatment during manufacturing processes. This texture causes anisotropy during deformation processes such as deep drawing, resulting in development of ears. Correlations between sheet processing and texture are as the following[4].

 [Annealing texture] (100) <001>: Cube orientation, (110) <001>: Goss orientation, etc.
 [Rolling texture] (123) <634>: S orientation, (112) <111>: C orientation, (110) <112>: Brass orientation, etc.

Since aluminum is a metal with a face-centered cubic structure, deformation proceeds along the slip system of slip surface (111)/slip direction <110> during plastic deformation. When a texture is deep drawn, anisotropy occurs in the direction of such an orientation. Correlation between texture and earing has been reported based on calculation for ear height, taking only stress equilibrium conditions at the flange part and cup wall part during deep drawing into consideration, using the finite element analysis of a polycrystalline model[4]. From the result of this analysis, we know that negative ears develop in 0-90 degrees for Cube and Goss orientations while positive ears develop in 45-degree directions for S and C orientations.

In actual materials, there is a mixture of multiple textures. An ear is formed as a result of a weight average distribution of textures. The final development of ears occurs from the conditions above as well as various additional deep-drawing conditions and material strength of the actual material.

2. Measurement principle

We have focused on the fact that texture distribution indicates ultrasonic anisotropy based in view of the correlation between texture and elastic anisotropy. Relationship between texture, plastic forming and elastic anisotropy is shown in **Fig. 3**. As mentioned above, ears developing during deep
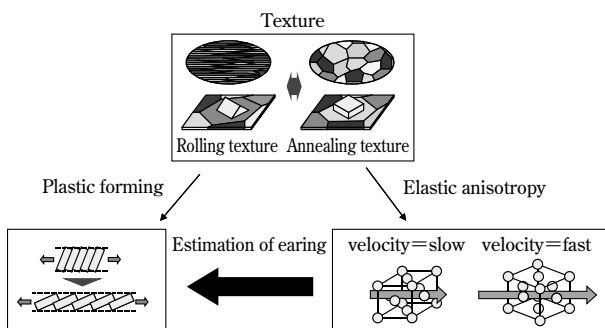
drawing processes are caused by textures, and their orientations are determined during the plastic deformation process of the deep drawing process. When ultrasound propagates, interatomic distances also fluctuate depending on directions, due to the unevenness in texture, resulting in fluctuation of the ultrasonic propagation speed, indicating acoustic velocity anisotropy. With the fracture method, earing is measured from plastic anisotropy upon its actual development. However, we have developed a method of measuring earing by focusing on the elastic anisotropy, and a device to measure ultrasonic anisotropy in various directions of an aluminum sheet[4].

In order to measure earing using the ultrasonic anisotropy, we may measure the difference in acoustic velocity depending on propagation directions of ultrasound, in other words, if the propagation distance is the same, fluctuation in propagation time may be measured. To this end, an evaluation value to evaluate the ultrasonic anisotropy was defined in equation (2).

$$E = (T_{-45} + T_{+45}) - (T_0 + T_{90}) \text{ (ns)} \quad \cdots\cdots\cdots\cdots(2)$$

Letting the rolling direction be 0 degree, T_θ is the propagation time for ultrasound propagating a set distance in a θ direction.

While there are many propagation types for ultrasound, such as longitudinal waves, transverse waves, and a mixture of these two wave types, a plate wave causing vibration in the entire sheet (Lamb wave) was applied so as to measure ultrasonic anisotropy in the entire target aluminum sheet. Several vibration modes are known to exist among plate waves, and each of the vibration modes indicates velocity dispersion depending on sheet thickness x frequency[5]. **Fig. 4** indicates the correlation between sheet thickness x frequency and velocity (calculated at 6,400m/s longitudinal wave and 3,040m/s transverse wave) for the ultrasonic propagation mode derived from theoretical calculation. In order to measure ultrasonic propagation time with stability and precision, it is necessary to have a method of measurement that can distinguish ultrasonic waveform of other vibration

Fig. 3 Relationship between texture, plastic forming and elastic anisotropy
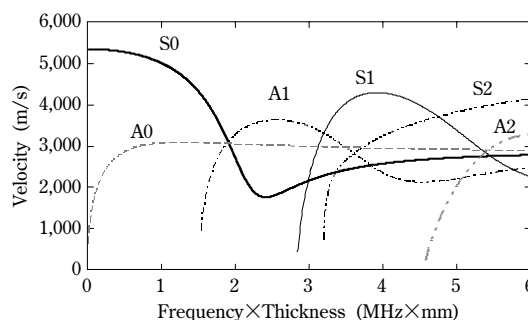

Fig. 4 Relationship between frequency, thickness and velocity

modes, and is capable of taking measurements in the low dispersion region. Based on such considerations, S0 mode without any overlapping vibration mode and having small velocity dispersion was selected.

When using a conventional piezoelectric device as an ultrasonic probe, a contact medium such as water or oil to propagate ultrasound in the target material becomes necessary. In such a case, measured propagation time would contain propagation time through the contact medium in addition to actual propagation time through the aluminum sheet. In other words, measuring texture-related ultrasonic anisotropy requires control of thickness of the contact medium at a submicron level, rendering it impractical. Therefore, an electro-magnetic acoustic transducer (EMAT)[6], without necessity of a contact medium, and capable of non-contact measurement useful in inline measurement, was selected.

Lorentz-type EMAT (its working principle is shown in **Fig. 5**) applicable to non-magnetic metals such as aluminum is used. It is comprised of a magnet and a coil. When a high-frequency current flows through a coil placed directly under a magnet, it excites an induced current in the material, generating ultrasound due to magnetostatic field and Lorentz force. The coil is a meander coil, making neighboring currents flow in opposing directions, causing Lorentz force to work in opposite directions as well, to develop a plate wave triggering vibration through the entire sheet. In terms of receiving ultrasound, the electromotive force induced in the coil is detected as the reception signal, from ultrasonic vibration on the material surface and the magnetostatic field based on the law of electromagnetic induction. Propagation time is measured in the direction of propagation in the aluminum sheet using this plate wave.
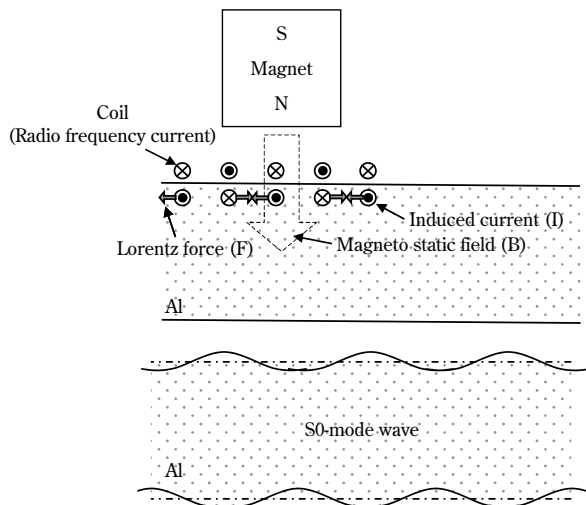

Fig. 5 Generation of S0-mode wave by EMAT

3. Equipment composition

3.1 EMAT sensor

From the plate wave dispersion characteristics shown in Fig.4, it is clear that frequency x sheet thickness must be less than 1.5 (MHz x mm) in order to solely generate the S0 mode. Meanwhile, it is more desirable for ultrasonic frequency to be high from the aspect of ultrasonic measurement precision. Therefore, target aluminum sheet thickness was designated to be less than 1mm for this equipment, and ultrasonic frequency was established to be 1.35MHz.

A plate wave in a specific mode must match its phase with an EMAT sensor for efficient transmission and reception. At the frequency above (1.35MHz) with the sheet thickness of less than 1mm, acoustic velocities range between 5,000 and 5,400m/s. Wavelength of S0 mode plate wave is determined to be 4mm judging from the correlation between the frequency and sheet thickness above as well as the equation where acoustic velocity = frequency x wavelength. Thus, the EMAT sensor coil was produced as a meander coil with opposing coil pitches of 2mm, the number of turns at 9, and the distance between transmission and reception coils of 90mm.

Layout of the EMAT sensor for earing measurement is indicated in **Fig. 6**. In order to evaluate composition ratios for annealing texture and rolling texture, sensors were placed in four directions namely 0 degree, + and − 45 degrees, and 90 degrees (T①-④: Transmission sensors and R ①-④: Receiving sensors) and the plate wave in S0 mode was propagated in four directions through the aluminum sheet.

3.2 System configuration

System configuration of the developed equipment is shown in **Fig. 7**. The function generator receives control signals from a PC to generate an ultrasonic oscillation waveform, which will be amplified by the RF power amplifier (RF power amp) with a maximum output of 5kW. Signal waveform is then sent to transmission EMAT sensor inside the sensor head via a channel switcher (Ch switch) to generate ultrasound in the target material (Al plate).

Ultrasound signal waveform received by the receiving EMAT sensor inside the same sensor head is sent to the receiver (Receiver) through a preamplifier (Pre-Amp). Received signals are converted to digital signals, and the propagation time is measured by performing a waveform analysis on a PC.

Ultrasonic propagation time in four directions

may be measured automatically by controlling with the channel switcher. Measurement time is about 2 seconds per location.

Fig. 8 shows the equipment appearance. A 19-inch rack houses both a measurement system and a signal processing system.
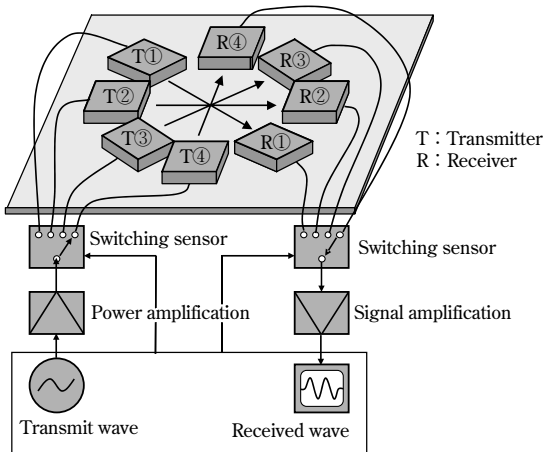
Fig. 6 Earing measurement by EMAT
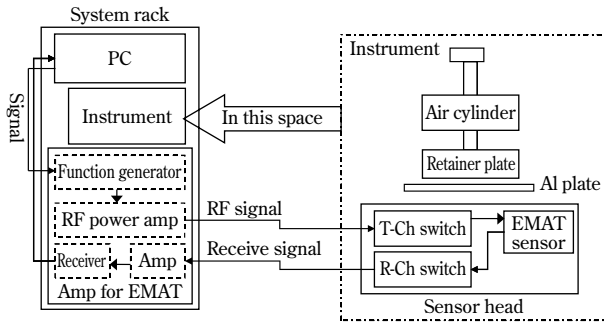
Fig. 7 System configuration
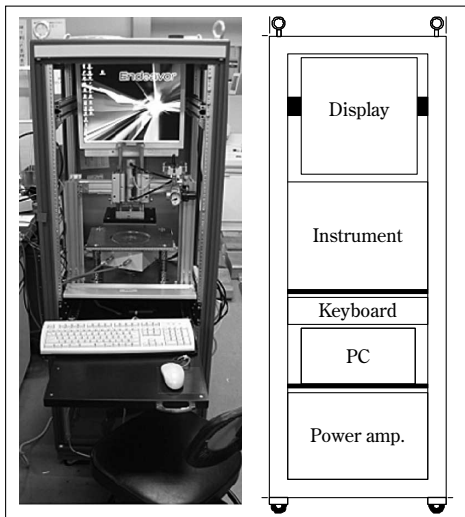
Fig. 8 Measurement system overview

4. Performance evaluation experiment result

4.1 Measurement result of ultrasonic anisotropy

An example of a received signal waveform measured by this equipment is shown in **Fig. 9**. According to Fig.9, the received signal is detected at approximately S/N=25. Also, **Fig.10** shows the difference in propagation time between rolling direction being the ultrasonic propagation direction and a 45-degree angle being the ultrasonic propagation direction. In this example, the difference in propagation time was about 30ns. Repeat accuracy for the earing measurement instrument is 0.1% for the earing. When calculating from the correlation between fracture method and measurement time of an EMAT waveform, the earing measurement instrument would need the time resolution of 2.5ns to measure the propagation time. Although pulse wave is suitable for detecting the difference in propagation time at high precision, it has a problem of being a single wave with insufficient signal strength. Therefore, burst wave was selected and arithmetic mean processing was used to improve S/N further. Also the difference in propagation time was calculated at high precision by taking cross-correlation with the reference waveform. Including the signal processing above, the measurement time for measuring four directions in one sample takes approximately 10 seconds.
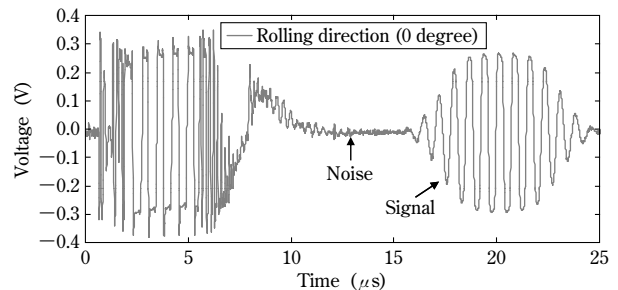
Fig. 9 Example of an ultrasonic waveform
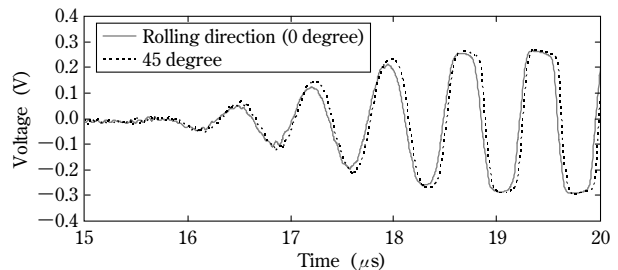
Fig.10 Difference of propagation time in various directions

4.2 Evaluation result of ultrasonic anisotropy and earing

Actual aluminum sheet samples were prepared with unique lot and charge for every product type by the MOKA PLANT, to conduct a confirmation experiment to evaluate if there was a correlation between the earing measured by fracture method and evaluation value E attained from the measurement by the EMAT earing measurement equipment. In order to make performance evaluation by the EMAT repeatable, an aluminum sheet from the same section was halved to be used for both the EMAT evaluation sample and for earing measurement by the fracture method. An example of correlation between earing by fracture method and ultrasonic anisotropy evaluation value E by EMAT for 3000 series (used for drinking can body material, etc.) grouped with keys such as corresponding material and sheet thickness is shown in **Fig.11**. Earing value by the fracture method is indicated on the y-axis, and evaluation value E by EMAT is indicated on the x-axis, and deviations from the calibration line are expressed as standard deviation. By grouping and calibrating measurement targets, it was confirmed from this result that evaluation values E and earing values have a linear relationship, and standard deviation σ (in earing %) became 0.05%. As a result, it was demonstrated that difference between the EMAT earing value and fracture method is within the target value of 0.5%, when using the evaluation value E for ultrasonic anisotropy shown by equation (2). Furthermore, it was confirmed that, in terms of stability, repeat measurement precision for three repetitions in one sample was 0.1%.

Measurement results for pure aluminum (1000 series: for condenser case application, etc.) are shown in **Fig.12**. Although the margin of error became greater when samples were grouped together as shown in Fig.12 (a), when they were categorized by heat treatment conditions as shown in Figs.12 (b) and (c), demonstrating a possibility of improving precision.
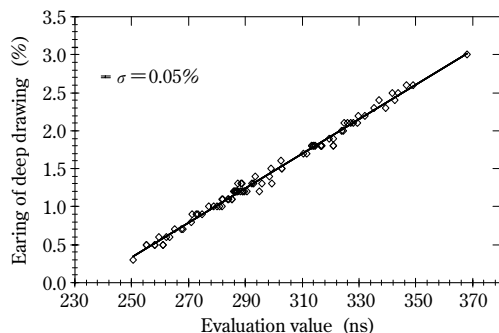
Fig.11 Correlation between earing of deep drawing and evaluation value

(a) No grouping

(b) Heat treatment condition 1

(c) Heat treatment condition 2
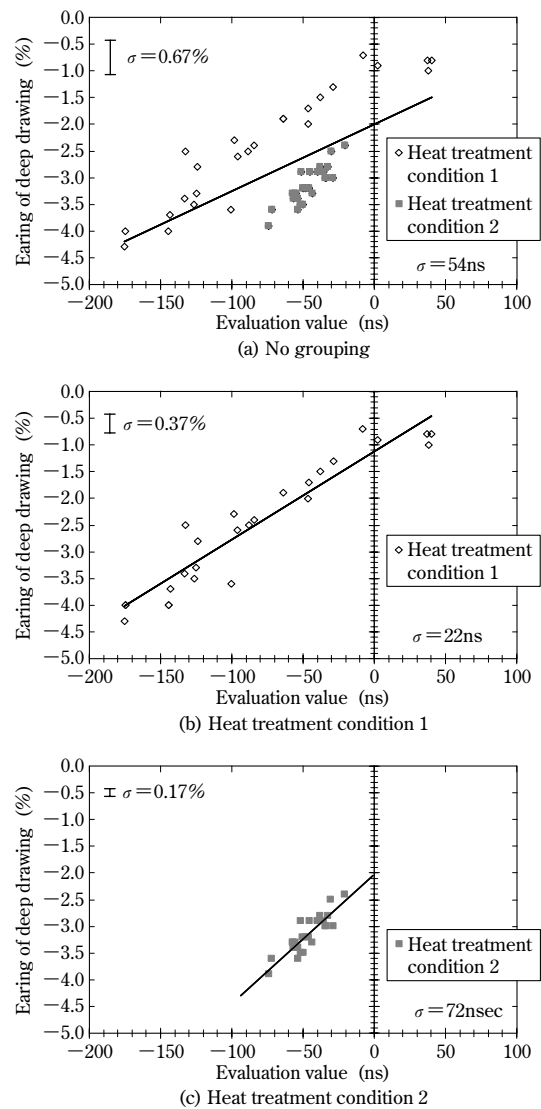
Fig.12 Correlation between evaluation value and earing occurring in the 1000 series

5. Consideration

Since a correlation between ultrasonic anisotropy and earing for various aluminum sheets with different product types and processes was observed, we may conclude that earing is strongly correlated with elastic anisotropy of initial texture. Therefore, there is a possibility that earing may be evaluated from the acoustic velocity measurement with universality by clarifying relationship between elastic characteristics and earing (plastic deformation).

However since plastic deformation for deep drawing fluctuate not only from the material, but also from processing conditions (such as lubricant and fold pressure) as well as from a combination of these conditions, it is considered more practical and realistic to calibrate in conjunction with materials and processing conditions. Calibration line for earing and evaluation value E for a 3000 series aluminum

sheet is expressed by the equation (3) in Fig.11.

Earing(%)=

0.0228 x evaluation value E (ns) − 5.361······(3)

Variance in the evaluation value E corresponding with variance of earing value at 0.5% was 22ns. Meanwhile, propagation time for transmission and reception by this equipment is transmission/reception distance (90mm)/acoustic velocity (5,000m/s) = 18,000ns. In order to evaluate earing with 0.5% resolution, acoustic velocity must be measured stably at 0.1% precision. As shown by the dispersion characteristics in Fig.4, acoustic velocity depends on the sheet thickness in addition to textures, fluctuation in sheet thickness contributes to creating an error. Unlike conventional piezoelectric sensors, ultrasonic frequency may be easily changed for EMAT, allowing for compensation of the sheet thickness fluctuation in frequency dependence of acoustic velocity.

Conclusions

Upon acquiring and confirming calibration data at the Quality Assurance Section of the MOKA PLANT, EMAT-based earing measurement equipment focusing on ultrasonic anisotropy was developed as a possible alternative technology for conventional earing measurement approach for plastic anisotropy in deep drawing processes. As a result, we have found that it is possible to predict earing by 0.5% (1 σ) of the fracture method, by establishing a calibration line for each set of product types and manufacturing conditions. We have also confirmed that 3000 series for drinking can bodies having a high production

volume may likewise be predicted for anisotropy at 0.05% (1 σ). We will continue to compare precision of EMAT earing measurement equipment against fracture test results for each of the product types in detail to consider the possibility of using it as a replacement technology for fracture tests.

The largest advantages of the developed equipment are absence of a contact medium and rapid measurements. This will not only allow for inspecting a larger number of locations, but will propose potential applications for all units or entire length inspections as well as inline monitoring at latter stage of manufacturing processes. We would also like to explore a larger scope of applications including implementations for steel and copper, as well as acoustoelastic measurement[7] of stress capitalizing on minute fluctuation in ultrasonic acoustic velocity caused by stress conditions of the medium.

References

1) The Japan Society for Technology of Plasticity. *Press Work Handbook.* Maruzen Co., Ltd., p.340.
2) D. Altenpohl. *Une introduction a la metallurgie structurale et a la transformation de l'aluminium.* 1971, p.94-95.
3) Naoyuki Kanetake et al. *Light Metals.* 1982, Vol.32, No.5, p.241-246.
4) Takeo Ogawa et al. *Proceedings of 7th Nondestructive Evaluation Symposium.* 2000, p.47-54.
5) The Nikkan Kogyo Shimbun, Ltd. *Ultrasonic Inspection.* p.65-71.
6) Riichi Murayama. *Nondestructive Testing.* 2009, Vol.58, No.7, p.262-268.
7) Hidekazu Fukuoka et al. *Introduction and Application of Acoustoelasticity.* Ohmsha, Ltd., 1993, 200p.

The Combined Effect of Pre-straining and Pre-aging on the Bake-hardening Behavior of Al-Mg-Si Alloy for Automobile Body Panels

Dr. Tetsuya MASUDA[*1], Yasuo TAKAKI[*1], Dr. Takeo SAKURAI[*2], Dr. Shoichi HIROSAWA[*3]

[*1] Aluminum Sheets & Coils Research Dept., Moka Plant, Aluminum & Copper Business
[*2] Technology Control Dept., Moka Plant, Aluminum & Copper Business
[*3] Graduate School of Engineering, YOKOHAMA National University

In order to develop a new Al-Mg-Si alloy for automotive body panels, the effect of pre-straining in combination with pre-aging on the bake-hardening behavior of an Al-0.6mass % Mg-1.0mass % Si alloy was investigated by means of the Vickers hardness test, electrical conductivity measurement, differential scanning calorimetry (DSC) and transmission electron microscopy (TEM). The hardness test and DSC analysis revealed that, with a pre-aging at 343K, a pre-strain as small as 3% was found to improve the bake-hardening response during final aging at 443K. The TEM observation confirmed that the improvement of the bake-hardening response is enhanced mainly due to the precipitation of the β" phase in the matrix. These results are explained by the consideration that dislocations induced by pre-straining reduce the concentration of quenched-in excess vacancies, resulting in both the suppressed clustering of solute atoms during pre-aging and the accelerated precipitation of the β" phase during final aging.

Introduction

Recently, aluminum alloys are being proactively used for automotive bodies to reduce the weight and to improve the fuel economy. Aluminum sheets for body panels are particularly required to have excellent formability and hemming performance. They are also required to have high strength after the paint-baking heat treatment (e.g., at 443K for 1.2ks). Al-Mg-Si alloys are commonly used for the body panels, because these alloys can have low proof strength in the stamping and hemming processes, exhibit excellent age hardenability during the subsequent paint-baking heat treatment to achieve high strength, and realize excellent surface quality and corrosion resistance simultaneously. The ability to undergo age hardening by a heat treatment at a relatively low temperature for a short time is herein called "bake hardenability". In this alloy system, the precipitation strengthening phase is primarily the β" phase, and Si rich Al-Mg-Si compositions are known to exhibit excellent bake hardenability[1]-[3].

The pre-aging, applied after the solid solution quenching and prior to the final aging, significantly affects the clustering behavior in the early stage of phase decomposition and the resulting bake hardenability[4]-[6]. Serizawa et al. showed that the clusters (Cluster (1)) formed at temperatures no higher than 343K and including room temperature, have a high thermal stability, decrease the distribution density of β" precipitates and suppress strengthening in the final aging, causing the negative effect of the two-step aging[7]. They also clarified the fact that the clusters (Cluster (2)) formed at higher temperatures (e.g., 373K) accelerate the formation of β" phase because of the continuous transformation into the β" phase, and that these two types of clusters (Cluster (1) and Cluster (2)) are formed competitively in this alloy system. In this paper, the clusters formed under various pre-aging conditions are referred to as either Cluster (1) or Cluster (2), according to the report by Serizawa et al.[7]

The pre-strain, applied after the solution heat treatment and prior to the final aging, largely affects the precipitation kinetics and process. In the case of Al-Mg-Si alloys, pre-straining is reported to decrease the activation energy for the precipitate growth and thus to accelerate the precipitation process[8],[9]. Matsuda et al. reported that the bake hardenability at 473K of an Al-0.37mass%Mg-0.62mass%Si alloy is improved, with increased peak hardness, by applying a pre-strain of 5% after pre-aging at 423K for 60ks[10]. Birol et al. reported that the application of pre-strain shortly after the solid solution treatment suppresses the formation of clusters at room temperature and accelerates the precipitation of β" phase during the final aging at 453K[11],[12].

These results suggest that a combined process of pre-straining and pre-aging is quite effective in improving the bake hardenability of the Al-Mg-Si alloys for automobile panels. It is considered that the amount of pre-strain and the conditions of pre-aging must be considered for optimization. This paper reports the effect of the process, combining pre-straining (0.5% and 3%) and pre-aging (at 298-343K), on the bake hardenability of Al-0.6mass%Mg-1.0mass%Si alloy for automobile panels.

1. Experimental method

Table 1 shows the chemical composition of the

alloy used for this study. The alloy ingot was homogenized, hot- and cold-rolled into a sheet having a final thickness of 1.0mm. This sheet was solid-solution-treated at 823K for 60s and was quenched into water. The average grain size, measured on the as-quenched material, was approximately 40μm as measured by the cross sectional method. The quenched samples were pre-strained for either 0.5% or 3% using a tensile testing machine. A sample without any pre-straining was also prepared as a reference.

These samples, with and without pre-straining, were aged isothermally at 298K, 313K and 343K (the aging hereinafter referred to as "one-step aging"). The samples were held at room temperature for 300s after quenching, until the start of the aging. The changes in hardness and electrical conductivity during the aging were measured by the Vickers hardness test (load 19.6N, holding time 15s) and eddy current method, respectively. Typical samples were subjected to the differential scanning calorimetry (hereinafter referred to as "DSC analysis") at a temperature rise rate of 0.17K/s. The bake hardenability was studied on the samples pre-aged at 298-343K for 7.2ks and subsequently final-aged at 443K for up to 1.2ks (the aging hereinafter referred to as "two-step aging"). **Fig. 1** shows the flow charts of the heat treatments. The microstructures of the typical samples were measured by transmission electron microscopy (TEM) at an accelerating voltage of 200kV.

Table 1 Chemical composition of the alloy studied

(mass%)

Si	Fe	Mn	Mg	Al
1.02	0.17	0.07	0.57	Bal.

(1) Single aging
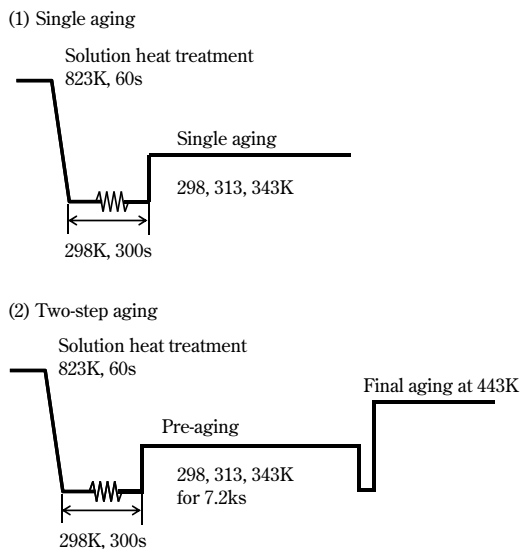
(2) Two-step aging

Fig. 1 Heat treatment flow charts

2. Experimental results

2.1 The effect of pre-straining on one-step aging behaviors

Fig. 2 shows the changes in hardness and electrical conductivity during one-step aging at 298-343K of the samples pre-strained for 0%, 0.5% and 3%. All the samples aged at 298K and 313K exhibit monotonic increase in their hardness. The hardness change of the samples aged at 313K is greater than that of the samples aged at 298K. Each sample aged at 343K increases in hardness in two stages, with a rapid increase in the second stage occurring at around 10^5s to 10^4s. For all the one-step aging conditions tested this time, the changes in hardness decreased with the increasing amount of pre-strain.

The electrical conductivity of the samples aged at 298K and 313K decreased as the aging time increased, while that of the samples aged at 343K increased slightly at around 3×10^3s and subsequently decreased rapidly. For all the one-step aging conditions tested this time, the electrical conductivity changed less with the increased amount of pre-strain. The change in electrical conductivity represents the change in the state of solid solution and precipitates in a sample. Therefore, the above results clearly indicate that pre-straining delays the age hardening behavior during the one-step aging under the current testing conditions.

Fig. 3 shows the results of DSC analyses conducted to clarify the phase decomposition process during the one-step aging. The endothermic peak (Peak 1) around 480K, the peak indicating the dissolution of Cluster (1)[2)-4)], becomes smaller with the increase in the aging temperature. The area of Peak 1 of the
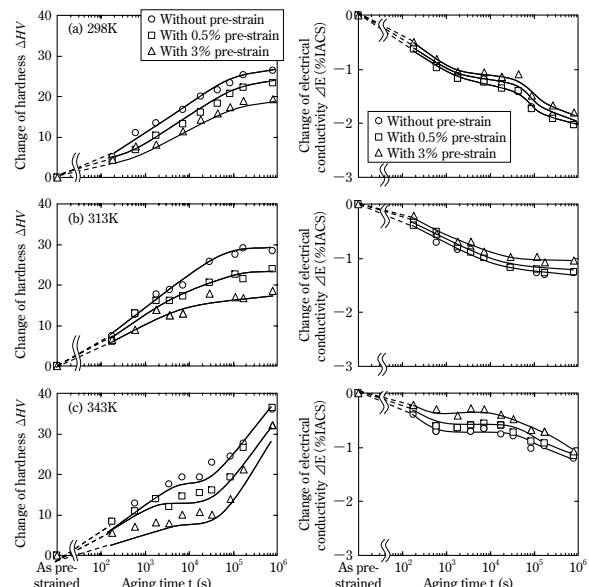
Fig. 2 Changes of hardness and electrical conductivity during one-step aging

Fig. 3 DSC curves

Fig. 4 Changes in hardness and electrical conductivity during final aging at 443K

Fig. 5 TEM bright-field images and selected area diffraction patterns

sample pre-strained for 3% has significantly decreased compared with that for the sample without pre-strain. These experimental results indicate that the area of Peak 1 (i.e., the amount of Cluster (1) formed during the one-step aging at temperatures no higher than 343K) is decreased, not only by the increased pre-aging temperature, but also by the application of the pre-strain. On the other hand, the exothermic peak (Peak 2) around 510K, the peak that indicates the formation of the β'' phase[2)-4), 13), 14)], was shifted towards the low temperature side by the application of 3% pre-strain for all the pre-aging conditions.
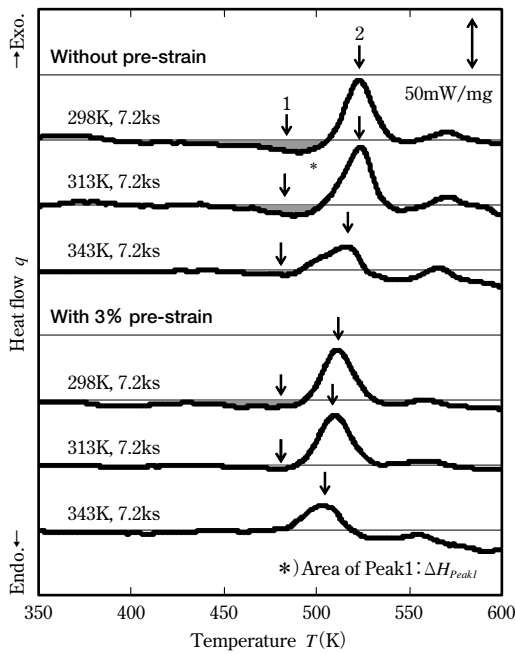
2.2 The effect of pre-straining on the final aging behaviors of two-step aged samples

Fig. 4 shows the changes in the hardness and electrical conductivity of the samples pre-strained for 0%, 0.5% and 3%, pre-aged under various conditions and final aged at 443K. All the samples exhibit hardness increase during aging at 443K. The increasing amount of pre-strain significantly improves the bake hardenability and also increases the change in electrical conductivity. The sample pre-strained for 3% and subsequently pre-aged at 343K for 7.2ks exhibits the most excellent bake hardenability (Fig. 4 (c)) with a change in electrical conductivity exceeding that of the sample without pre-aging. These results clearly indicate that an effective combination of pre-straining and pre-aging accelerates the phase decomposition process during the final aging at 443K and improves the bake hardenability.

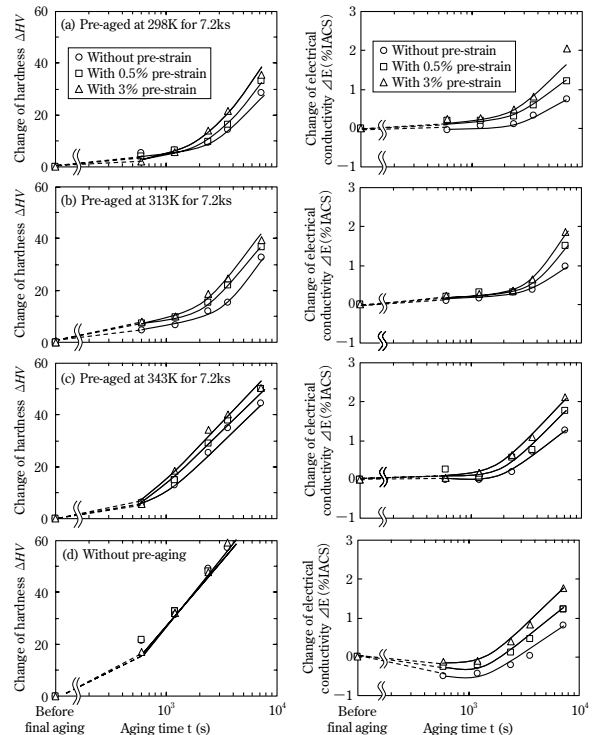**Fig. 5** shows the TEM bright field images and selected area diffraction patterns of the samples pre-strained for 0%, 0.5%, 3%, pre-aged at 343K for 7.2ks and final-aged at 443K for 3.6ks. It should be noted that the increased changes in hardness of the two-step aged samples that are pre-strained and pre-aged

(Fig. 4 (c)) are attributable to these microstructures. Observations at low magnifications confirmed an increase in dislocation density with the increasing amount of pre-strain. The spherical or needle-like precipitates observed by high-magnification TEM are considered to be β'' phase, judging from the streaks along the $[010]_{Al}$ and $[100]_{Al}$. The samples pre-strained for 0.5% and 3% exhibit stronger strain contrasts, implying the acceleration of the phase decomposition by the pre-straining.

From the above results, the improved bake hardenability achieved by the combined process of pre-straining and pre-aging is considered to be mainly attributable to the accelerated precipitation of β'' phase in the matrix. Although the dark field image shows some precipitates on dislocation lines, the majority of the precipitates are in the matrix because of the small amount of strain applied.

3. Discussion

3.1 The suppression of Cluster (1) formation by pre-straining

Serizawa et al[7]. reported, on the basis of their study using a three dimensional atom probe, that the hardness change during the room-temperature aging of an Al-0.95mass%Mg-0.81mass%Si alloy[6] is attributable to the formation of Cluster (1). A similar kind of cluster is considered to be formed during the one-step aging in the samples studied this time.

As shown in Fig.2, an increased amount of pre-strain decreases the changes in hardness and electrical conductivity during the one-step aging. The result indicates that the pre-straining suppresses the clustering of solute atoms, or the formation of Cluster (1), during the subsequent one-step aging. This is also confirmed by the DSC analysis result (Fig. 3), which shows that the increasing amount of pre-strain decreases Peak 1, which implies the dissolution of the Cluster (1).

The clustering behavior of the solute atoms in the early stage of phase decomposition is considered to be affected by the vacancy concentration in the alloy. On the other hand, the dislocations introduced by pre-straining are considered to act as sink sites for quenched-in excess vacancies[15]. The dislocation density, $N_{annealed}$, in a fully annealed metal is generally reported to be $1\times10^{11}-1\times10^{12}\mathrm{m}^{-2}$ [16]. Komatsu et al. reported that the increment of dislocation density, $\varDelta N$, caused by a deformation is expressed by the true strain, ε, and the change in electrical resistivity per unit dislocation density, $\varDelta\rho$, as the following equation[17]:

$$\varDelta N = A\varepsilon^n/\varDelta\rho \cdots\cdots\cdots\cdots\cdots\cdots(1),$$

wherein $A = 0.185\mathrm{n}\Omega\,\mathrm{m}$, $n = 0.648$ (in the case of Al-0.47mass%Mg alloy) and $\varDelta\rho = 3\times10-25\,\Omega\,\mathrm{m}^3$ (99.996% in the case of highly-pure aluminum)[18]. Assuming that these constants are applicable to the alloy system of the present study, the dislocation density, $N_{pre\text{-}strain}$, of the sample pre-strained for 3% ($\varepsilon = 0.0296$) is estimated to be approximately $1\times10^{14}\mathrm{m}^{-2}$, since $\varDelta N$ is sufficiently larger than $N_{annealed}$. On the other hand, the average distance between dislocations is given by[19]

$$L = 1/N^{1/2} \cdots\cdots\cdots\cdots\cdots\cdots\cdots\cdots\cdots(2),$$

which yields the average distances for the samples with 3% pre-strain and those without pre-strain to be $1\times10^{-7}\mathrm{m}$ and $1\times10^{-6}-3\times10^{-6}\mathrm{m}$, respectively. From the above, the lifetime, τ, at 298K, of the quenched-in excess vacancies until their annihilation into dislocations is given by the following expression[20].

$$\tau = L^2/D_v \cdots\cdots\cdots\cdots\cdots\cdots\cdots\cdots(3)$$

From the equation (3), the lifetime, τ, is calculated to be 7s and $4\times10^2-4\times10^3$s for the samples with 3% pre-strain and those without pre-strain, respectively. The diffusion coefficient of the vacancies, D_v, is given by the equation (4), wherein $D(T)$ is the self-diffusion coefficient of aluminum at the temperature, T, and $C_v(T)$ is the thermal equilibrium vacancy concentration[21].

$$D_v = D(T)/C_v(T) \cdots\cdots\cdots\cdots\cdots\cdots(4)$$

Here, the term $D(T)$ is expressed by equation (5), using the vibration frequency factor for the self-diffusion of aluminum ($D_0 = 1.37\times10^{-5}\mathrm{m}^2\mathrm{s}^{-1}$), activation energy ($Q = 123\mathrm{kJmol}^{-1}$) and gas constant ($R = 8.31\mathrm{Jmol}^{-1}\mathrm{K}^{-1}$).

$$D(T) = D_0 \exp(-Q/RT) \cdots\cdots\cdots\cdots(5)$$

The following equation is used to determine $C_v(T)$[22].

$$C_v(T) = \exp(2.4)\exp(-73.3[\mathrm{kJ\cdot mol}^{-1}]/RT) \cdots(6)$$

The quenched-in excess vacancies, introduced into the sample by the solution heat treatment, may possibly be annihilated into the defects other than the dislocations (e.g., grain boundaries); however, from the above estimation of the vacancy lifetime, τ, it is considered that the dislocations introduced by the pre-straining mainly, and more effectively, decrease the quenched-in excess vacancy concentration, delaying the diffusion of solute atoms. It is concluded that, as a result of the above, the formation of Cluster (1) during one-step aging is suppressed, which maintains the high supersaturation of solute atoms in the matrix.

3.2 The acceleration of β'' phase formation by pre-straining

As shown in Fig. 4, an effective combination of pre-straining and pre-aging improves bake hardenability during the subsequent aging at 443K,
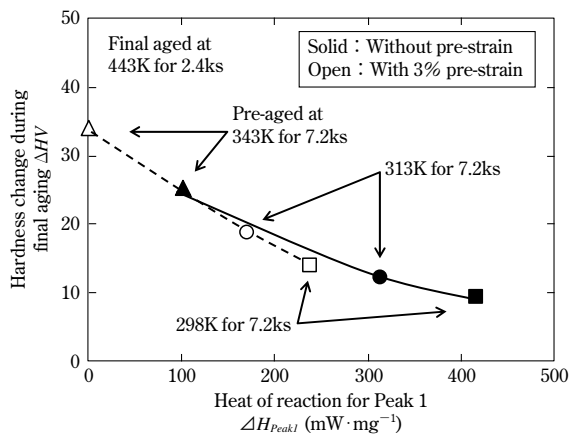
Fig. 6 Relationship between hardness change during final aging at 443K for 2.4ks; ΔHV, and heat of reaction for Peak 1; ΔH_{peak1}

and the effect of pre-straining is particularly enhanced in the sample pre-aged at 343K for 7.2ks. The improvement effect on the bake hardenability brought about by the pre-straining is also confirmed by the result of the DSC analysis (Fig. 3), which shows that Peak 2, an indication of β'' phase formation, shifts towards the low temperature side. These results suggest that a new process that combines pre-straining, as small as $0.5-3\%$, with pre-aging is effective in producing automobile panels with high strength without sacrificing their formability.

The acceleration of β'' phase formation by a combined process of pre-straining and pre-aging is explained by the difference in the amount of Cluster (1) formed, an explanation similar to the one that has been applied to the hardness change during the one-step aging (Section 3.1). **Fig. 6** shows the relation between the hardness change during final aging at 443K, ΔHV, and the heat of reaction determined from Peak 1, ΔH_{peak1}. The samples, some with 3% pre-strain and some without, were pre-aged under the various conditions shown in Fig. 4. The heat of the reaction was determined from the area surrounded by the DSC curves and base lines shown in Fig. 3. Referring to Fig. 6, the hardness change, ΔHV, increases with the decrease of ΔH_{peak1} regardless of the pre-straining. This indicates that the bake hardenability at 443K is mainly determined by the amount of Cluster (1) formed during the pre-aging. In other words, the suppressed formation of cluster(1) by pre-straining is attributed to the increased bake-hardening response at 443K due to the accelerated precipitation of the β'' phase from more supersaturated solute atoms.

Conclusions

A study was conducted on the effectiveness of a process that combines pre-straining and pre-aging to improve the bake hardenability of an Al-0.6mass% Mg-1.0mass%Si alloy for automobile panels. Hardness measurements, electrical conductivity measurements, DSC analyses, and TEM observations were used for the study. It has been clarified that an increasing amount of pre-strain decreases the amount of change in hardness and electrical conductivity during the subsequent one-step aging and the heat of reaction for endothermic peak around 480K in DSC traces. These results imply that an increasing amount of pre-strain decreases the amount of Cluster (1) formed during the one-step aging at temperatures no higher than 343K. On the other hand, the TEM observations and DSC analyses have clarified that the pre-straining promotes the precipitation of β'' phase during the final aging at 443K for 7.2ks. The effect of the pre-straining on bake hardenability depends on the subsequent pre-aging conditions, and a pre-straining of 3% has been found to be most effectively combined with a pre-aging at 343K for 7.2ks. These results can be explained by suppressed clustering of solute atoms during pre-aging and accelerated precipitation of the β'' phase from more supersaturated solute atoms during final aging, both of which are attributed to rapid annihilation of quenched-in excess vacancies at dislocations induced by pre-straining.

A part of this article was published in Materials Transactions[23].

References

1) J. Langerweger. *Aluminium Technol.* 1986, Vol.49, p.216-222.
2) W. F. Miao et al. *Scr. Mater.* 1999, Vol.40, p.873-878.
3) A. K. Gupta et al. *Mater. Sci. Eng. A.* 2001, Vol.316, p.11-17.
4) G. A. Edwards et al. *Acta Mater.* 1998, Vol.46, p.3893-3904.
5) M. Murayama et al. *Acta Mater.* 1999, Vol.47, p.1537-1548.
6) S. Hirosawa et al. *Mater. Sci. Forum.* 2005, Vol.475-479, p.357-360.
7) A. Serizawa et al. *Metall. Mater. Trans. A.* 2008, Vol.39A, p.243-251.
8) H-L. Lee et al. *Scr. Metall. Mater.* 1991, Vol.25, p.2165-2170.
9) R. S. Yassar et al. *Metall. Mater. Trans. A.* 2005, Vol.36A, p.2059-2065.
10) K. MATSUDA et al. *Journal of Japan Institute of Light Metals (in Japanese).* 1995, Vol.45, p.95-100.
11) Y. Birol. *Scr. Mater.* 2005, Vol.52, p.169-173.
12) Y. Birol et al. *Scr. Mater.* 2006, Vol.55, p.625-628.
13) I. Dutta et al. *J. Mater. Sci. Lett.* 1991, Vol.10, p.323-326.
14) N. Maruyama et al. *Scr. Mater.* 1997, Vol.36, p.89-93.
15) M. Murakami et al. *Philos. Mag.* 1970, p.1119-1126.
16) W. D., Jr. Callister. *Materials Science and Engineering, An Introduction. John Wiley & Sons,* 2007, p.166.
17) S. Komatsu et al. *Proceedings of ICAA-6.* 1998, p.991-996.
18) J. G. Rider et al. *Philos. Mag.* 1966, Vol.13, p.289-303.
19) J. Friedel. *Dislocations. Pergamon Press.* 1964, p.239.
20) G. ITO. *NETSU SHORI (in Japanese).* 1998, Vol.38, p.165-173.
21) R. O. Williams. *Acta Metall.* 1957, Vol.5, p.55-56.
22) R. O. Simmons et al. *Phys. Rev.* 1960, Vol.117, p.52-61.
23) T. Masuda et al. *Mater. Trans.* 2010, Vol.51, p.325-332.

Highly Functional Pre-coated Aluminum Sheets, the "KS700" Series

Tomoko TANAKA[*1], **Nobuo HATTORI**[*1]

[*1] Aluminum Sheets & Coils Research Dept. Moka Plant, Aluminum & Copper Business

The KS700 series of newly developed pre-coated aluminum sheets realizes surface functionalization and shortens the manufacturing process. The KS700 series enables the omission of some steps in the manufacturing process, such as degreasing, anodizing and plating, thus saving costs. Products using the KS700 series show good surface qualities and resist fingerprints, scratching and corrosion, among other things. This paper explains the features of the highly functional pre-coated aluminum sheets and introduces several examples of applications.

Introduction

It was in the 1970s that Kobe Steel started the surface treatment of aluminum sheets. The business at that time was limited to the color painting of construction materials and the painting of the coils for beverage cans[1]. In the 1980s, a hydrophilic treatment was put into use for air-conditioner fins; and in the 1990s, the development of lubricant pre-coated sheets, the forerunners of the "KS700" series, began[2]. Since the 2000s, the company has strengthened the product line-up of the KS700 series by adding various surface functions, not obtainable by untreated aluminum sheets, while maintaining superior lubricity[3].

This paper describes the features, concrete examples of use, and future trends of the highly functional pre-coated aluminum sheets of the KS700 series, whose applications are expanding, particularly in the field of electronics.

1. The advantage of using pre-coated aluminum sheets

Pre-coated aluminum sheets (hereinafter simply referred to as "pre-coated sheet(s)") are aluminum sheets that are coated before factory shipment. The primary purpose of pre-coating aluminum sheets is to provide various functionalities to the surfaces of the aluminum sheets and thus to add high value to the aluminum parts produced by press forming the sheets. The secondary purpose is to decrease the total cost by omitting steps in the process of producing the parts. This section explains the concept of the functional upgrading of aluminum sheets and the steps in the manufacturing process that can be omitted by using the pre-coated sheets.

1.1 The functional upgrading by pre-coating

1) The improvement of formability

Lubrication oil must be applied to the aluminum sheets to be press formed. Providing, in advance, high lubricity to an aluminum sheet surface homogenizes the flow of the aluminum sheet in the mold and prevents cracking and necking. This enables the forming of shapes that had been difficult to form using a conventional aluminum sheet.

2) The improvement of product appearance

Aluminum sheets must be handled with care because, unlike steel sheets, they have surfaces that are soft, can easily be scratched and are susceptible to fingerprints. The pre-coating protects the aluminum sheet surfaces and decreases the number of scratches caused by sliding against press forming molds[4]. Pre-coating also makes fingerprints much less noticeable during the manual handling of the press-formed parts, improving the product yield.

3) The improvement of corrosion resistance

When an aluminum sheet is left with salt and/or fingerprints on its surface for a long period of time, white rust forms at the places where the salt and/or fingerprints have adhered. In a normal environment, the white rust does not erode the internal portion of the aluminum sheet; however, it deteriorates the esthetic appearance. White rust can be prevented by applying an anticorrosion pre-coating.

Because the pre-coated sheets are presumed to be press formed, the corrosion resistance of, not only the flat sheet, but also the formed parts, is being considered[5].

4) The selection of electric non-conductance/conductance

Aluminum is an electrically conductive material; however, when an application calls for electric insulation, a non-conductive film can be pre-coated on the aluminum surface. Conversely, the pre-coated film can be provided with an electrical conductivity suitable for securing the grounding required for electronics products.

1.2 The omission of process steps, thanks to pre-coated sheets, and environmental considerations

1) The omission of the cleaning step

Fig. 1 shows an example of the processes for

Usual process

Bare aluminum → Oiling → Forming → → Drying → After coating

Pre-coated aluminum process

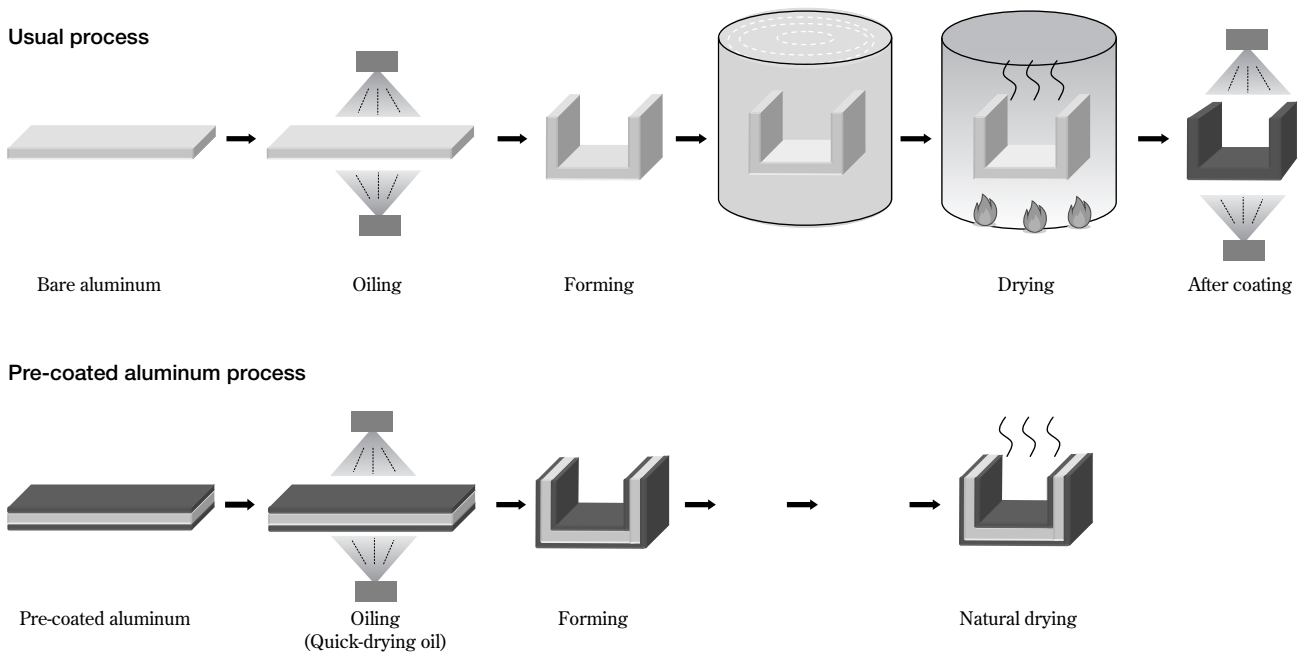Pre-coated aluminum → Oiling (Quick-drying oil) → Forming → → → Natural drying

Fig. 1 Production process omission

producing parts from aluminum sheets. In general, when an aluminum sheet is press-formed, lubrication oil is applied to the surface to facilitate the flow of the sheet in the mold, and the lubrication oil is removed by a cleaning step after the forming. Providing the aluminum sheet surface in advance with a lubricity sufficient to permit the flow of the material into the mold enables the use of a quick-drying oil that requires no cleaning after the forming, thus making the step of removing the lubrication oil unnecessary.
2) The omission of surface treatment

The functional upgrading of the surfaces of the aluminum parts can be achieved by surface treatments after forming. Treating the surfaces of the parts one by one in a batch process, however, may have the drawback of low productivity and high cost. In the case of pre-coated sheets, on the other hand, functional films can be continuously applied to the surfaces in advance, so as to omit steps such as the surface treatment after forming.

Therefore, the cost increase caused by pre-coating can be offset sufficiently by the omission of process steps such as cleaning and surface treatment.
3) Environmental considerations

The hydrocarbon detergents and chloride detergents used for cleaning, as well as the process liquid used for anodization and plating, are not environmentally friendly. The use of pre-coated sheets makes process steps such as cleaning, anodization and plating unnecessary and thus decreases the use of noxious liquids.

2. The development of the "KS700" series

2.1 The basic concept

The basic concept for the KS700 series is to provide lubricity sufficient to allow continuous forming using a quick-drying lubrication oil and thus to render unnecessary the cleaning steps in the customers' processes, decreasing their total production cost. There are 9 types of products in the KS700 series (**Table 1**), each having varied functionality, in addition to lubricity; they were developed in response to the various needs of customers. The following describes the features of these types of products and gives concrete examples of their uses.

2.2 Highly formable pre-coated sheet "KS705"

Products such as beverage cans and the casings for chip capacitors are deep-drawn / ironed and are usually painted, or are used with film laminates, after forming. The film laminates are materials consisting of thermoplastic films, such as nylon films and PET films, adhered together. Unlike the thermosetting resins generally used for the pre-coated sheets, the thermoplastic resins used for the film laminates have molecules that are not three-dimensionally cross-linked and are more flexible than the thermosetting resins. These thermoplastic resins, on the other hand, have lower heat resistance because of their thermoplasticity, are difficult to make into thin films and are more costly.

Table 1 Features of KS700 series

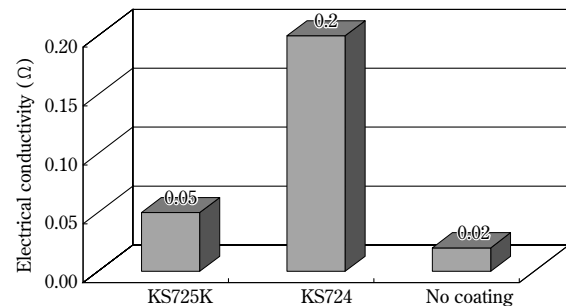|	KS705	KS725K	KS730	KS744	KS750	KS752	KS760	KS776	KS780	No coating
Lubricity	Good	Good	Good	Normal	Good	Good	Good	Normal	Good	Poor
Corrosion resistance	Good	Good	Good	Good	Good	Good	Good	Good	Good	Poor
Fingerprint resistance	Good	Good	Good	Good	Good	Good	Good	Good	Good	Poor
Scratch resistance	Good	Excellent~Good	Good	Excellent	Good	Good	Good	Good	Good	Poor
Electrical conductivity	Poor	Excellent	Poor	Poor	Good	Poor	Poor	Poor	Poor	Excellent
Hygienic	–	–	Excellent	–	–	–	–	–	Excellent	–
Heat release	Normal~Excellent	–	–	–	Excellent	Excellent	–	–	–	Poor
Peel-off adhesive tape	Poor	Poor	Poor	Poor	Poor	Poor	Excellent	Excellent	Poor	Poor
Scratch protection for optical disc	Poor	Poor	Poor	Poor	Poor	Poor	Poor	Excellent	Poor	Poor
Antibacterial	–	–	–	–	–	–	–	–	Excellent	–

The KS705 is an aluminum sheet with a pre-coat that is as flexible as the film laminates and can be deep drawn, unlike the conventional pre-coated sheets. **Fig. 2** shows the examples of $\phi 10 \times 20$mm hollow cylinders that are deep drawn. The film can be colored so as to realize heat radiation with an emissivity 15 to 20 times higher than that of the conventional aluminum sheet. The KS705 is expected to be used, for example, for the heat sinks of LEDs. These heat sinks have complicated shapes and are required to have high heat radiation. Our internal evaluation has confirmed that heat sinks made of the KS705 have a cooling performance that is comparable with that of the commercially available die-cast heat sinks[6].
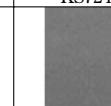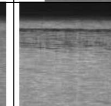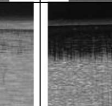
2.3 Conductive lubricant pre-coated sheet "KS725K"

Many electronics parts are required to be grounded on their surfaces to prevent malfunctioning due to electromagnetic noise and static electricity. Conventional pre-coated sheets, which have insulated surfaces, are difficult to use for such applications. Kobe Steel launched aluminum sheets such as KS720 and KS724, pre-coated with conductive lubricant, as groundable pre-coated sheets[7]; however, with further advances in the performance of electronic devices, there has come to be a need for pre-coated sheets with increased conductivity. The KS725K has an extremely high conductivity, which is comparable with that of the untreated aluminum sheet, a level of conductivity unprecedented in any existing products such as KS724, and has anti-scratch and anti-fingerprint properties that cannot be achieved by untreated aluminum sheets (**Fig. 3, Fig. 4**). This product can improve the product yield because it

	KS705 white	KS705 black	KS705 silver	No coating
Emissivity	>0.75	>0.80	>0.60	0.04
Formed cup appearance 10mm				–

Fig. 2 Emissivity and formed cup appearance of KS705

Fig. 3 Electrical conductivity of KS725K

Fig. 4 Fingerprint resistance and scratch resistance of KS725K

decreases the number of scratches due to sliding against the molds during press forming, as well as the scratches due to friction with the packaging materials during transportation. These characteristics of the KS725K have expanded its applications, including that of covers for optical disk drives.

2.4 Corrosion resistant, lubricant pre-coated sheet "KS730"

Parts for refrigerators and rice cookers may come in direct contact with food. Therefore, it is a prerequisite for the materials used in these parts that they be harmless to the human body.

The KS730 uses a raw material film that has been approved as safe by the Food and Drug Administration (FDA). The KS730 also passed testing according to the standards set by the Ministry of Welfare (back then) and has been safely used for food-related applications.[8] The product has excellent corrosion resistance, an important feature for food-related applications, and prevents the corrosion of the aluminum sheet by hot water and hot steam (**Fig. 5**).

Exploiting these features, the pre-coated sheet is applied to refrigerator trays, rice cooker parts, and the like.

2.5 Hard pre-coated sheet "KS744"

Untreated aluminum sheets and the conventional pre-coated sheets have soft surfaces and are easily scratched. Therefore, they are usually provided with hard anodized films or with post-process painting when they are used for sliding parts or for parts affecting the appearance.

The film of the KS744 has a high degree of hardness and no scratches are left when its surface is scrubbed with steel wool (**Fig. 6**). In addition, the film is not only hard, but also well-formable (**Fig. 7**). Therefore, the pre-coated sheet can replace the anodized products used for the exterior parts and sliding parts of electronic equipment.

2.6 Heat releasing pre-coated sheet, "KS750" and "KS752"

The heat generated by electronic equipment may cause the equipment to malfunction, so it must be released outside. Modern electronic devices, with their high performance, downsizing and emphasis on design, have complicated internal structures that call for more efficient heat radiation.

The film used for the KS750 (KOBEHONETSU aluminum) has an emissivity, an indicator of its infrared radiation characteristic, of 0.86, which is approximately 20 times higher than the emissivity of the untreated aluminum, which is 0.04[9]. A heat radiation test conducted internally on this KS750, with its superior heat releasing performance, demonstrated that the temperature inside a box simulating an electronic device is 5℃ lower than

KS730   No coating

(Whiting)
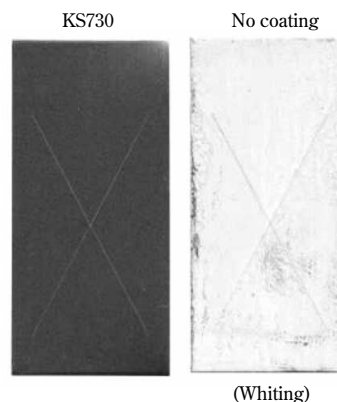
Fig. 5 Corrosion resistance of KS730 (JIS Z2371 SST500h)

KS744   No coating

20mm
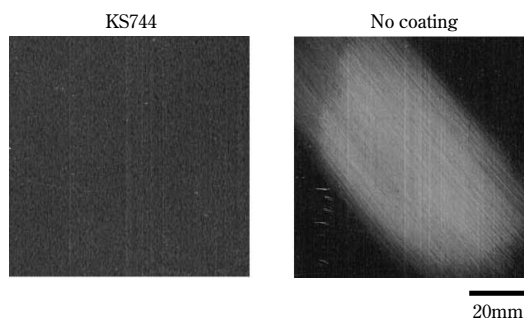
Fig. 6 Scratch resistance of KS744 (Rubbed with steel wool)

50mm
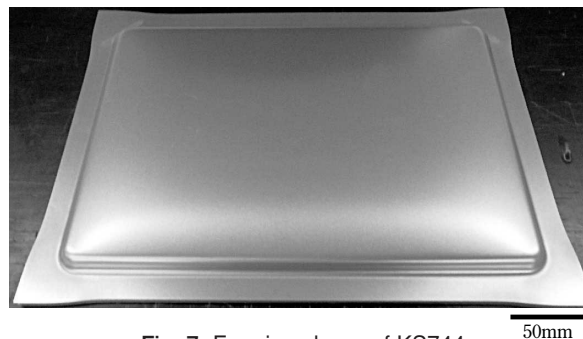
Fig. 7 Forming shape of KS744

50mm
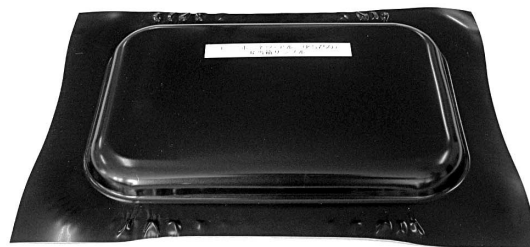
Fig. 8 Forming shape of KS750

that inside a box made of an untreated aluminum sheet.

Fig. 8 is an example of drawn-formed KS750. In addition to the conventional black conductive type, KS750 (KOBEHONETSU aluminum), a black insulation type, "KS752BK", and white insulation type, "KS752WT", have recently been commercialized,

allowing customers to choose the conductivity and color of their applications.

2.7 Non-adhesive pre-coated sheet, "KS760"

Personal computers with built-in optical drives have prevailed these days, enabling people to easily produce CDs and DVDs (hereinafter, optical disks) of their own at home. The trouble is that the labels affixed to user-made optical disks may adhere inside audio-visual apparatuses, making the disks difficult to unload. We have developed a non-adhesive pre-coated sheet, KS760, to prevent such troubles[10].

The KS760 has a film featuring a surface which does not readily permit adhesive materials such as labels to adhere to it. **Fig. 9** shows the test results confirming the non-adhesive nature of the KS760. The adhesive material on the KS760 was peeled off using one-fifteenth of the force required to peel it off the conventional coating. The surface is less likely to become smeared--with oil-based ink, for example-- and such smearing can readily be removed. The KS760 has won a fine reputation as a material for use in the internal parts of on-board auto-changers.

2.8 Anti-scratch pre-coated sheet "KS776" for optical disks

Repeated loading and unloading of an optical disk may scratch the disk at the points where it comes in contact with the optical disk apparatus, rendering the media no longer usable.

The KS776 adopts a film that is softer than the optical disks. With a decreased number of contact points between the disk and film, the number of scratches on the disk has been decreased significantly (**Fig.10**).

These characteristics have been highly rated, leading to the use of KS776 in the housings of the slot-in drives built into personal computers.
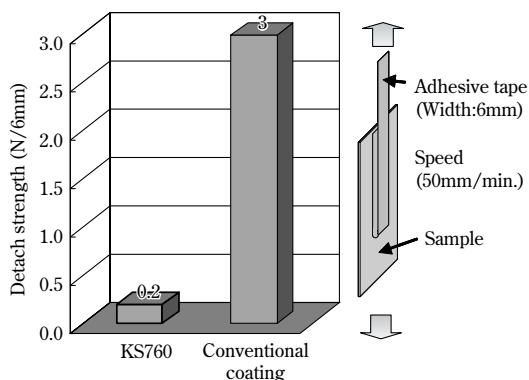

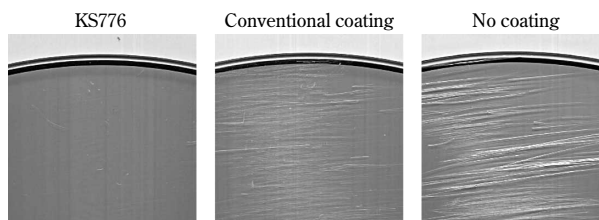KS776   Conventional coating   No coating

Fig.10 Scratch protection for optical disc of KS776
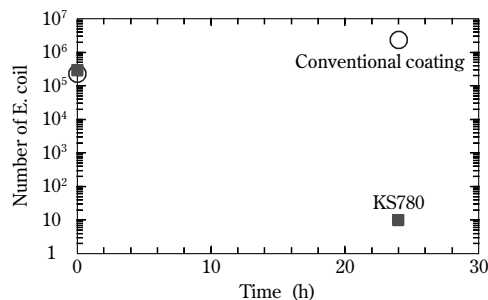
Fig.11 Anti-bacterial test result of S780

2.9 Antibacterial pre-coated sheet, "KS780"

Modern airtight buildings tend to have increased humidity and unventilated air, causing bacteria and mold to easily breed in the interior living environment. There has been an increasing interest in antibacterial and sterilizing measures.

The KS780 is a pre-coated sheet that exploits the antibacterial action of silver ion to prevent the breeding of Escherichia coli, Staphylococcus aureus, and the like. **Fig.11** shows an evaluation result for the sheet's antibacterial feature. The KS780 exhibits a number of E. coli a ten-thousandth of that counted on a conventional pre-coated sheet. The newly developed film retains its antibacterial feature after immersion in boiling water or retort sterilization. It also satisfies the standard of the Ministry of Welfare (at the time) and can be used safely in the fields of food, kitchens and cosmetics.

3. Future efforts

In order to make the pre-coated aluminum sheets stand out from steel and stainless sheets, the intrinsic features of aluminum, the base material, must be exploited, e.g., in applications that require weight reduction, thermal and electrical conductivity and/or corrosion resistance. Among other areas of interest, electronics will continue to be a major target, because, for example, notebook PCs and tablet devices are required to be smaller, lighter and more mobile, and advanced digital home electronics and LED lamps are required to have improved heat radiation.

In order to cultivate demand in the field of electronics, where the price competition is fierce, it

Fig. 9 Peel off strength of adhesion label of KS760

is necessary to develop new products that are conventionally unthinkable. Examples include: ① pre-coated sheet that achieves overwhelmingly low costs, ② pre-coated sheet that achieves major weight reduction, for example, by replacing die cast parts, ③ pre-coated sheet with superior designability, and ④ pre-coated sheet that can be used in an unexpectedly severe environment. The users' requirements are becoming more and more stringent every year. In response to such user needs, we will continue to develop new products that are attractive enough to offset the cost of the pre-coated sheets, which is slightly higher than that of untreated aluminum sheets.

Conclusions

The features and examples of the use of the pre-coated aluminum sheet "KS700" series, manufactured by Kobe Steel, have been summarized. The KS700 series is being employed, and its applications are expanding, in the field in which steel sheets, stainless steel sheets and untreated aluminum sheets have hitherto been used. With the lack of increase in the domestic demand for aluminum, as in the case of beverage cans, developing new applications of aluminum is a challenge not only for Kobe Steel, but also for the whole industry. Adding value by pre-coating is expected to be a useful approach for dealing with such a challenge. We will strive to develop technologies and products to cultivate new applications.

References

1) K. Hatanaka. *Journal of Japan Institute of Light Metals.* 2000, Vol.50, No.11, p.625-627.
2) K. Kamiya et al. *KOBE STEEL ENGINEERING REPORTS.* 2001, Vol.51, No.1, p.56-60.
3) N. Hattori et al. *KOBE STEEL ENGINEERING REPORTS.* 2002, Vol.52, No.2, p.94-98.
4) N. Fujiwara et al. *KOBE STEEL ENGINEERING REPORTS.* 2004, Vol.54, No.1, p.29-33.
5) N. Hattori et al. *Journal of Japan Institute of Light Metals,* 2008, Vol.58, No.4, p.157-161.
6) N. Hattori et al. *KOBE STEEL ENGINEERING REPORTS.* 2012, Vol.62, No.1, p.95.
7) N. Hattori et al. *KOBE STEEL ENGINEERING REPORTS.* 2001, Vol.51, No.2, p.82.
8) K. Kamiya et al. *KOBE STEEL ENGINEERING REPORTS.* 1998, Vol.48, No.3, p.91.
9) N. Hattori. *KOBE STEEL ENGINEERING REPORTS.* 2003, Vol.53, No.2, p.105.
10) N. Hattori. *KOBE STEEL ENGINEERING REPORTS.* 2006, Vol.56, No.1, p.78.

The Effect of the Extrusion Temperature on the Recrystallization Textures of an Extruded AA6005C Alloy

Dr. Kentaro IHARA[*1], **Takahiro SHIKAMA**[*2], **Keiji MORITA**[*3]
[*1] Technology Control Dept. Moka Plant, Aluminum & Copper Business
[*2] Aluminum Extrusion & Fabrication Plant, Chofu Works, Aluminum & Copper Business
[*3] SHINKO FAB TECH, LTD.

A study was conducted to determine the effect of the extrusion temperature on the recrystallized grain size and texture of an AA6005C alloy. Several extrusion tests were conducted at temperatures from 753 to 793K at an extrusion speed of 3m/min. A decrease in extrusion temperature from 793K to 753K was found to increase the average size of recrystallized grains from 170μm to 230μm and the volume fraction of cube-oriented recrystallized grains from 30% to 40%. A high-temperature compression test, conducted to elucidate the process of recrystallized grain formation, revealed that, compared with extrusion at 793K, extrusion at 753K yields fewer recrystallized grains immediately after the deformation, indicating that a larger amount of energy is stored in the un-recrystallized region. The increased stored energy is considered to have promoted the preferential growth of the recrystallized Cube grains.

Introduction

The 6000 series Al-Mg-Si alloys are used as extrusions mainly in the fields of transportation equipment, building materials and electronic equipment. The structural materials for transportation equipment, including automobiles, are required to have properties such as mechanical strength, corrosion resistance and weldability[1]. Generally, these materials are forcibly cooled after extrusion, aged at high temperatures to a T5 condition and used in the high strength condition with their fibrous structures extending in the extrusion direction. The mechanical properties of an extruded material depend on its recrystallization texture. For example, the texture, highly oriented in the Cube direction, {100} <001>, of a hollow profile is reported to improve impact resistance[2]. The report that the recrystallization texture of an extruded material depends on the extrusion temperature is based primarily on round bars[3], and not much has been reported concerning hollow profiles. This study aims to clarify the effect of the extrusion conditions on the formation process of the recrystallization texture in a hollow profile of AA6005C (JIS 6N01)-T5 aluminum alloy. A study was conducted on the recrystallization textures of the hollow profiles, extruded at various temperatures and T5 treated. The following is an outline of the study.

1. Experimental method

The tested samples were prepared from hollow profiles made of an AA6005C (JIS 6N01)-T5. Their chemical composition and the process of producing the samples are shown **Table 1** and **Fig. 1**, respectively. Each billet, having a diameter of ϕ155mm, was homogenized at 520℃ for 4h, reheated to a temperature of 480℃, 500℃, or 520℃, and hot-extruded at a rate of 3m/min with an extrusion ratio of 44. The extrusion exit temperature was approximately 15℃ higher than the reheating temperature, due to the heat of deformation. The extruded profiles were held for 20s after the extrusion and then water cooled. They were subsequently aged at 190℃ for 3h to prepare the T5 treated samples.

These samples were subjected to tensile tests,
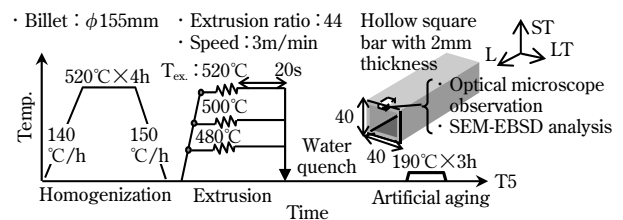
Fig. 1 Schematic view of the process for extruded 6005C alloys

Table 1 Chemical composition of studied Al-Mg-Si alloy (wt%)

	Si	Fe	Cu	Mn	Mg	Cr	Zn	Ti	Mn+Cr	Unspecified other elements	
										Each	Total
Specimen	0.40	0.20	0.15	—	0.80	—	—	0.02	—	—	—
AA6005C	0.40−0.90	0.35	0.35	0.50	0.40−0.80	0.30	0.25	0.10	≦0.50	0.05	0.15

optical microscopy observation, texture measurement and transmission electron microscopy (TEM) observation. Each tensile test was performed on a JIS13B specimen with its longitudinal direction parallel to the extrusion direction (L direction); the specimens each having a gauge length of 50mm. The tensile tests were conducted at a cross head speed of 2mm/min and at an initial strain rate of $7 \times 10^{-4} s^{-1}$. The crystal grain structures were observed under an optical microscope on the LT-ST cross sections of the samples etched by 5% sodium hydroxide. The texture measurement was conducted according to the electron back scattering pattern (EBSP) method using a scanning electron microscope (SEM). An LT-ST cross-section of each sample was electro-polished and was measured by an orientation imaging microscope (OIM), manufactured by TSL Solutions, that is mounted on an SEM (JEOL6500F), made by Japan Electro Optical Laboratory. The acceleration voltage was 15kV, and an area of $2 \times 2mm$ was measured with a step interval of $5 \mu m$. The TEM observation was conducted to measure the size of disperse particles and their spacing. In addition to the extrusion test, elevated temperature compression tests were conducted on the sample billets to clarify the initial formation process of the recrystallized structure. **Fig. 2** schematically depicts the testing conditions. Column shaped specimens, each having a dimension of $\phi 8 \times 12mm$, were machined from the billet homogenized at 520℃ for 4h. These specimens were subjected to the compression test at a strain rate of $10s^{-1}$ and a compression ratio of 75%. These high temperature compression tests were performed at the temperatures of 495℃ and 535℃, 15℃ higher than the respective extrusion temperatures of 480℃ and 520℃. This was to account for the deformation heat generated during the extrusion. The test employed the THERMECMASTOR-Z, made by Fuji Electronic Industrial Co., Ltd. After completing the deformation by compression, the samples were held for 2 and 5 seconds, respectively, before being water cooled. Then the microstructure at the center of each sample was observed on a section parallel to the compression axis, using the optical microscope and SEM-EBSD.
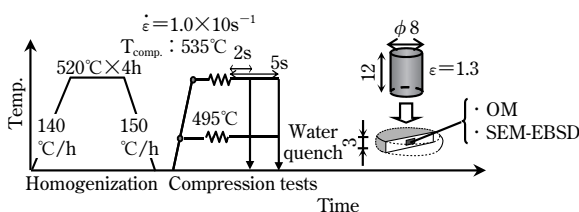
2. Experimental results

2.1 The tensile properties of the samples

The tensile properties in the extrusion direction of the sample, shown in **Table 2**, satisfy the requirements of JIS H4100 with a tensile strength and proof strength slightly higher than the standard values. The tensile strength and proof strength decreased with decreasing extrusion temperature.

2.2 The microstructures of the samples

2.2.1 Crystal grain structure

Fig. 3 shows the optical micrographs of the recrystallization structures of the samples. **Table 3** summarizes the results of the microstructure measurements performed on the materials extruded at various temperatures. For extrusion temperatures ranging from 480 to 520℃, the recrystallization occurred throughout the wall thickness. When the extrusion temperature was lowered from 520℃ to 480℃, the average size of the recrystallized grain in

Table 2 Tensile properties of extruded 6005C-T5 specimens

$T_{ex.}$ (℃)		TS (MPa)	YS (MPa)	El. (%)
520		278	255	12
500		277	252	12
480		266	241	12
Standard data of 6005C [12]	T5	265	225	14
JIS H4100	T5	≧245	≧205	≧8

Table 3 Summary of the measurement results

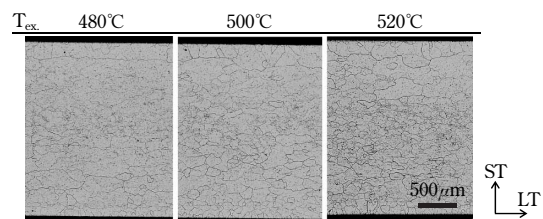| $T_{ex.}$ (℃)		480	500	520
Mean grain size (μm)	Surface layer	132	139	136
	Center layer	234	178	165
Area fraction of texture (%) (LT-ST cross section)	Cube	38	30	29
	Goss	8	8	9
	Brass	4	3	5
	S	3	2	6
	Cu	3	1	2
	{112}<110>	3	2	2
	{001}<110>	3	1	1
Mean dispersoids size (nm)		140	136	140
Mean dispersoids space (μm)		2.2	2.5	2.2

Fig. 2 Schematic view of the process of hot compression tests

Fig. 3 Optical microstructure of extruded 6005C-T5 alloys (Tex.: Extrusion temperature)

the center layer increased from 165 μm to 234 μm.

2.2.2 Crystal orientation distribution

Fig. 4 shows the crystal orientation distributions of the samples. Fig. 4 (A) is an inverse pole figure map showing the crystal orientation in the L-direction, with the orientations depicted by the color inside the stereographic triangle in the right hand side of the figure. Fig. 4 (B) is a color depiction of the distribution of the major texture orientations, i.e., the Cube orientation {001} <100>, Goss orientation {001} <100>, Brass orientation {011} <211>, S orientation {123} <634>, Cu orientation {112} <111>, {112} <110> orientation and {001} <110> orientation. The black solid lines in Fig. 4 (B) indicate boundaries with a misorientation of 15° or greater. These boundaries correspond to high-angle grain boundaries.

As shown in Fig. 4 (A), the center layer has a crystal orientation distribution that is different from that of the surface layer. The center layer has a structure oriented in the <001> direction, while the surface layer has an orientation distribution that is relatively random. The center layer is primarily dominated by the distribution of the Cube orientation, and subsequently dominated by the Goss orientation. In the surface layer, the {112} <110> orientation and {001} <110> orientation are distributed, but these orientations are non-existent in the center layer. These are the orientations that are the same as the ones[3)-5)] formed by the shear strain imposed on the extrusion surfaces. Also observed in the surface layer are the distributions of the Goss orientation, Brass orientation, S orientation and Cu orientation.

The center layer was separated from the surface

layer on the basis of the difference in the crystal orientation distribution shown in Fig. 4 (A). For each of these layers, the recrystallized grain size was measured from the average spacing of high-angle grain boundaries. The result is shown in **Fig. 5**. When the extrusion temperature was lowered from 520℃ to 480℃, the recrystallized grain size in the center layer increased from 165 μm to 234 μm. On the other hand, the recrystallized grain size in the surface layer remained in the range from 136 μm to 132 μm, showing little if any change. **Fig. 6** shows the relationship between the area fractions of the oriented grains and the extrusion temperature. The area fractions of the oriented grains were measured throughout the wall thickness in Fig. 4 (B). The major oriented grains, whose area fractions are affected by the extrusion temperature, are the Cube-oriented grains distributed in the center layer. The area fraction of the Cube-oriented grains increased from 29% to 38% as the extrusion temperature was
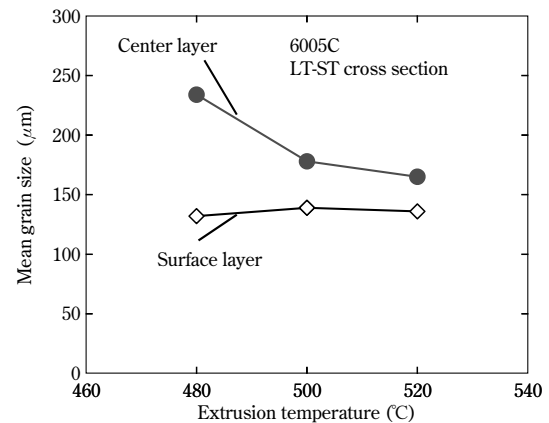

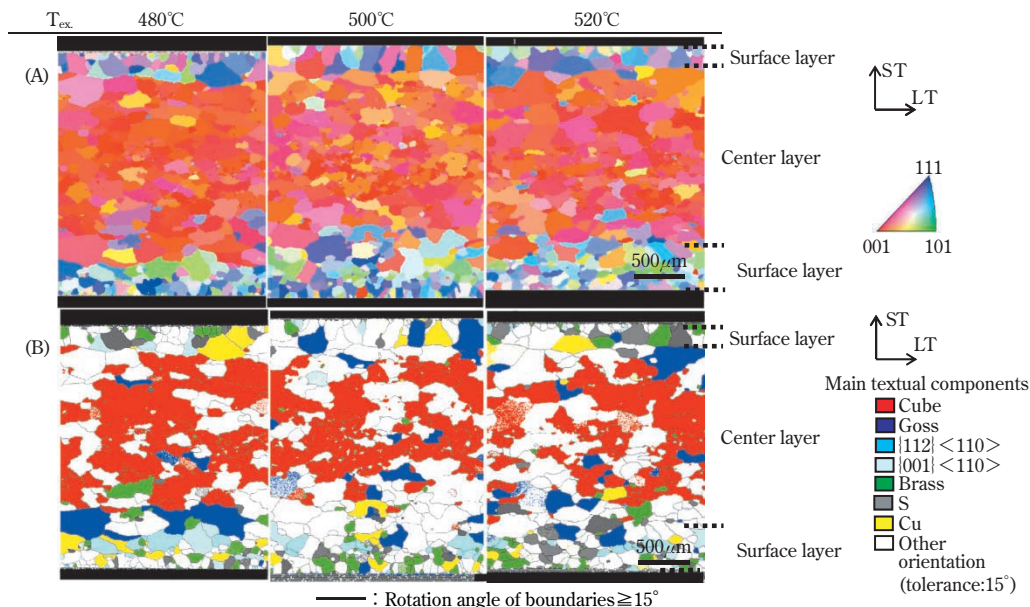**Fig. 5** Relationship of extrusion temperature and recrystallized grain size

Fig. 4 SEM-EBSD maps of extruded 6005C-T5 alloys (A: Orientation distribution, B: Main textual components)
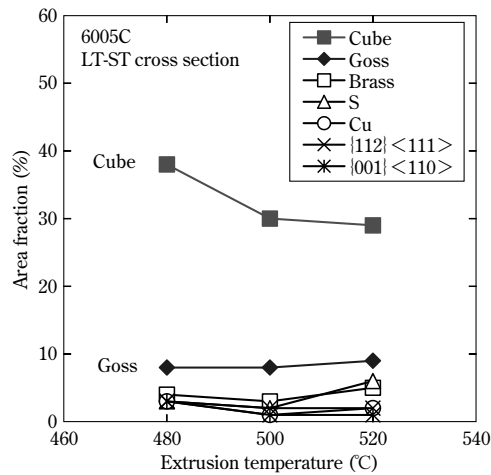
Fig. 6 Relation between area fraction of textual components and extrusion temperature

lowered from 520℃ to 480℃. The coarsening of the recrystallization grains in the center layer, which is due to the lowered extrusion temperature, corresponds to the increase in the area fraction of the Cube-oriented grains. It has been reported that, in the case of extruded round bars of the 6063 alloy, lowering the extrusion temperature from 520℃ to 400℃ decreases the ratio of <100> fiber from 53% to 27% in the recrystallization texture at a working ratio of 92%[6]. A similar tendency has also been reported for the case of extruded round bars of pure aluminum, for which the extrusion temperature was lowered from 480℃ to 290℃[7]. These studies include the temperature range in which the materials are not fully recrystallized with a significant amount of <111> fiber structure still remaining. Therefore, these results cannot be compared with the results of the present study, in which a fully recrystallized sample shows a tendency for the area fraction of the Cube-oriented grains to increase from 30% to 40% as the extrusion temperature is lowered from 520℃ to 480℃.

The area fractions of the major oriented grains, other than the Cube-oriented grains, remained almost unchanged regardless of the extrusion temperature. As the extrusion temperature increases, the area fraction of the Cube-oriented grain decreases. On the other hand, the total area fraction of the other oriented grains, excluding the major oriented grains measured, has increased. This implies that the higher extrusion temperature facilitates the recrystallization and growth of the grains having various orientations. It is reported that, in the case of rolled sheets, the bendability improves with the increase of the Cube-oriented grains[8), 9)]. To confirm this, a bending test according to the V-block method (JIS Z2248) was conducted in the LT direction of the samples. The result shows that
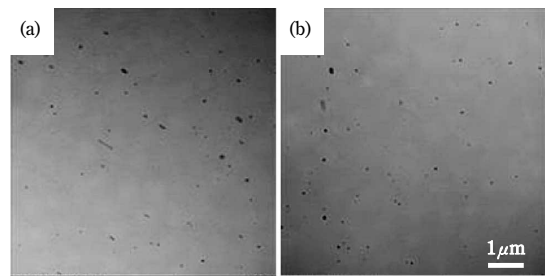
Fig. 7 Dispersoids in 6005C alloys extruded at (a)480℃, (b)520℃

decreasing the extrusion temperature from 520℃ to 480℃ decreases the critical bending radius from 1.5mm to 0.3mm, indicating that the higher the area fraction of the Cube-oriented grains, the better the bendability.

2.2.3 Dispersoids

Fig. 7 shows the TEM micrographs of the dispersoids in the samples extruded at the different temperatures. Both samples were homogenized at 520℃ for 4h, and almost no difference was found in the particle size and spacing of the Al-Fe-Si dispersoids. Thus, the dispersoids are not the cause of the increasing recrystallized grain size and the increasing area fraction of the Cube-oriented grain that are observed with a decreasing extrusion temperature. Rather, the change in the recrystallized grain size and texture is attributable to the extrusion temperature.

3. Discussion

3.1 Deformation temperature and the amount of accumulated strain

In order to clarify the recrystallization process of the samples, the microstructure of each sample was observed in the early stage of recrystallization during the elevated temperature compression test. **Fig. 8** shows the stress-strain curve. It is known that the deformation stress during elevated temperature

Fig. 8 Stress-strain curves for 6005C alloys compressed at (a)495℃, (b)535℃

deformation is proportional to the 1/2 power of the dislocation density, as in the case of ambient temperature deformation[10]. In the case of the present compression test, the material deformed at 495℃ 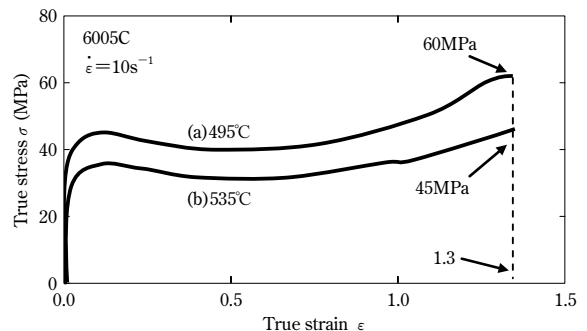exhibits a deformation stress approximately 30% greater than that of the material deformed at 535℃, indicating that its dislocation density is approximately 70% higher.

3.2 The crystal grain structure in the early stage of recrystallization

Fig. 9 shows the optical micrographs in the centers of the samples at 2 and 5 seconds have elapsed after they were compressively deformed for 75% at 535℃ and 495 ℃. When 2 seconds have elapsed, crystal grains having diameters of approximately 10 to 20 μm are observed in the deformation structures, elongating in the transverse direction, for both the sample deformed at 535℃ and the one deformed at 495℃. These crystal grains are considered to be recrystallized grains because they are equiaxed. At the point where 5 seconds have elapsed, both of the samples, deformed at 535℃ and 495℃, exhibit the propagation of recrystallization throughout the region observed, with the growth of the recrystallized grains. The sample deformed at 495℃ exhibits a recrystallized grain size after the grain

growth that is larger than that for the sample deformed at 535℃.

3.3 The crystal orientation distribution in the early stage of recrystallization

In order to confirm the formation of preferential orientation in the early stage of recrystallization, an SEM-EBSD analysis was conducted at the center of each of the samples 2 seconds after it had been compressively deformed. The results are shown in **Fig.10**. Fig.10 (a) shows the inverse pole figure maps in the compression axis direction with the orientations
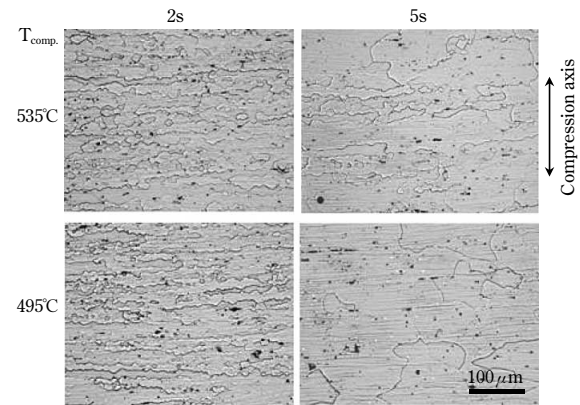

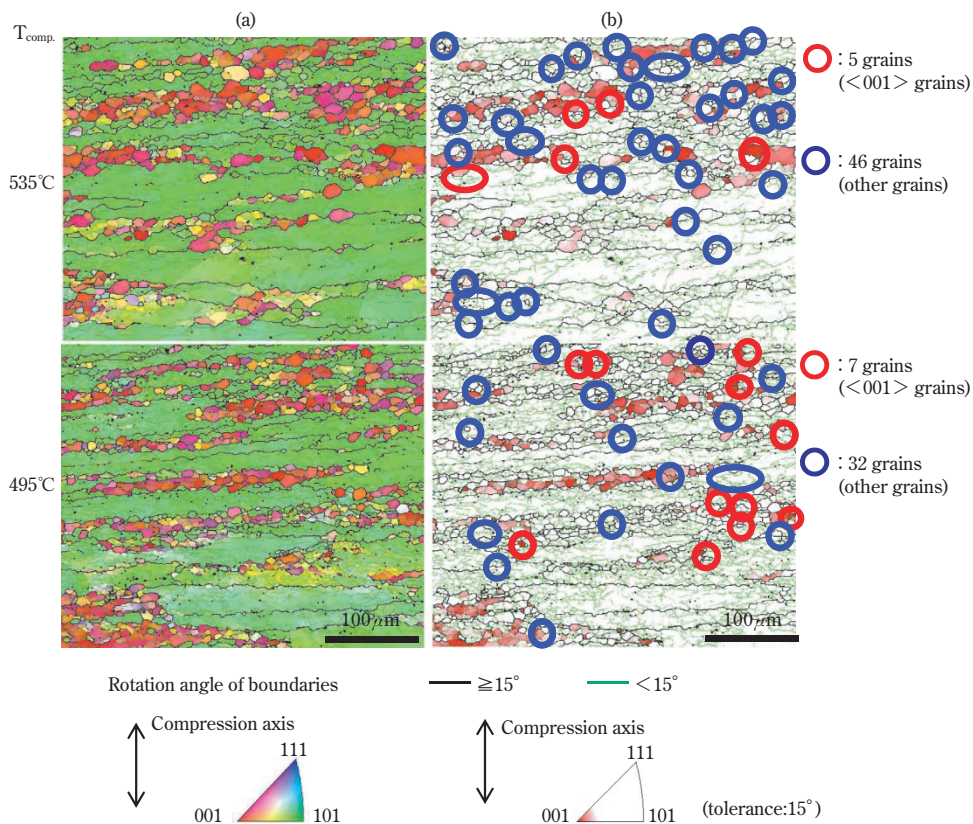Fig. 9 Optical microstructure in center of compressed 6005C alloys

Fig.10 SEM-EBSD maps in center of compressed 6005C alloys
(a) orientation distribution of compression axis, (b) distribution of <001> grain

depicted by the color in the stereographic triangle below. The red region in the map is the area where the compression axis direction is oriented in the <001> direction, while the green region is the area where the compression axis direction is oriented in the <110> direction. The grains in these areas are herein referred to as "<001> grains" and "<110> grains", respectively. In Fig.10 (b), only the <001> grains are shown in red (tolerance: 15°), in which the black lines correspond to high-angle grain boundaries and the green lines to low-angle grain boundaries. The equiaxed crystal grains, surrounded by high-angle grain boundaries, but not including a low-angle grain boundary inside, are regarded as recrystallized grains. Among these recrystallized grains, the <001> grains are surrounded by red circles, while grains other than the <001> grains are surrounded by blue circles. The number of recrystallized grains in the measured field was found to be 51 for the sample deformed at 535℃ and 39 for the sample deformed at 495℃. Thus, the sample deformed at 495℃ has fewer recrystallized grains. The number of <001> grains was found to be 5 for the sample deformed at 535℃ and 7 for the sample deformed at 495℃. Thus the sample deformed at 495℃ has a higher ratio of <001> grains in the recrystallized grains.

3.4 The mechanism for the preferential growth of Cube orientation grains in the sample

The <110> orientation is considered to have a large Taylor factor for compressive deformation and a greater accumulated energy, while <100> is the orientation with a small Taylor factor for compressive deformation and has a smaller accumulated energy[11]. Therefore, the <001> grains shown in Fig.10 are considered to have an orientation that easily recovers and preferentially grows, the orientation which corresponds to the Cube-oriented in the center layer of the extruded material. The material deformed at 495℃ has fewer recrystallized grains, in the early stage of recrystallization, than the material deformed at 535℃ and has a larger ratio of <001> grains. In addition, the material deformed at 495℃ has a greater accumulation of strain energy in the un-recrystallized region, which increases the growth rate of the <001> grains that can preferentially grow. This is considered to result in the increased area fraction of the recrystallized grains, such as Cube-oriented grains, that can preferentially grow.

A phenomenon similar to that observed for the above described material that is compressively deformed at elevated temperatures is considered
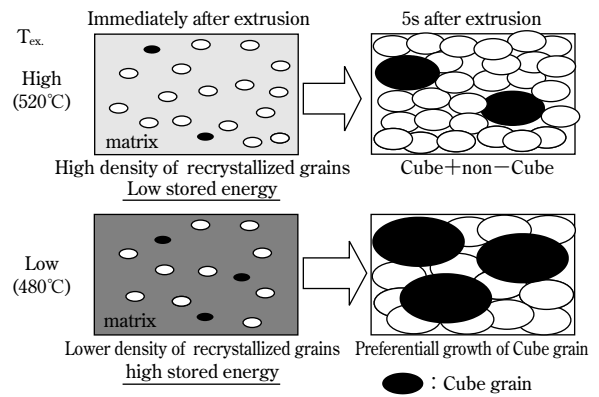
Fig.11 Schematic view of recrystallization in 6005C alloy

to be occurring in the extruded samples. **Fig.11** schematically illustrates the phenomenon. When the extrusion temperature is as low as 480℃, the number of recrystallized grains immediately after the deformation is small. However, the occupation rate of the Cube-oriented grains, which can easily recover, is considered to be high. In the un-recrystallized region, where there is a large accumulation of strain energy, the Cube-oriented grains, having a high growth rate, grow preferentially, increasing the area fraction of the Cube-oriented grains in the recrystallization structure after extrusion.

Conclusions

The change in recrystallization texture was studied in the T5 treated hollow profiles of a 6005C aluminum alloy, while lowering the extrusion temperature from 520℃ to 480℃. Elevated temperature compression tests were also performed to clarify the recrystallization process. The following conclusions were drawn:
・ By lowering the extrusion temperature from 520℃ to 480℃, the average size of recrystallized grains increased from approximately 170 μm to approximately 230 μm, with the occupancy rate of the Cube-oriented grains increased from approximately 30% to approximately 40%.
・ When the extrusion temperature is as low as 480℃, the number of recrystallized grains immediately after the deformation is small. However, the ratio of the Cube-oriented grains, which can easily recover, is considered to be large. This is considered to indicate that, in the un-recrystallized region, where there is a large accumulation of strain energy, the Cube-oriented grains, having a higher growth rate, grow preferentially, increasing the area fraction of the Cube-oriented grains in the recrystallization structure after extrusion.

References

1) T. Aiura et al. *KOBE STEEL ENGINEERING REPORTS.* 2002, Vol.52, No.3, p.83.
2) T. Furu et al. *Mater. Sci.* For. 519-521, 2006, 1421.
3) H. Inoue. *Journal of Japan Institute of Light Metals.* 2002, Vol.52, No.11, p.525.
4) J. Baumgarten et al. *Z.Metallkd*, 72 (1981), 162.
5) J. Baumgarten et al. *Z.Metallkd*. 72 (1981), 75.
6) T. Takahashi et al. *Journal of Japan Institute of Light Metals.* 1969, Vol.19, No.1, p.17.
7) J. Grewen et al. *Metall.* 12 (1959), 523.
8) S. Ikawa et al. *Journal of Japan Institute of Light Metals.* 2011, Vol.61, No.2, p.53.
9) A. Hibino et al. *Proceedings of the Japan Institute of Light Metals, 106th Spring Conference.* 2004, p.89.
10) F. R. Castro-Fernandes et al. Mats. Sci. and Tech. 6 (1990), 453.
11) H. Jeong et al. *Journal of Japan Institute of Light Metals*, 52 (2002), 525.
12) Japan Aluminium Association. *Aluminum Handbook 7th edition.* 2007, p.49.

A Technology for Manufacturing Magnesium Alloy Components with Excellent Heat Resistance

Ryoji ASAKAWA[*1], Kenichi HIRUKAWA[*1]
[*1] Daian Plant, Aluminum & Copper Business

Magnesium alloy forgings have been attracting attention for use in next-generation components with light weight and high heat resistance. A two-step process consisting of casting small diameter rods and forging them offers a viable solution for reducing the cost of forged Mg alloy products. To establish the process, we have developed technologies for continuously casting small diameter rods and for forging Mg alloys with low deformability.

Introduction

As a measure against global warming, various industries are promoting the reduction of the weight of transportation equipment to improve the fuel economy. In such an effort, Kobe Steel is carrying out the development of heat-resistant wrought Mg alloys that are applicable even for engine parts, and the development of their manufacturing technologies.

In general, Mg alloys are light in weight, but their melting and casting require a means to prevent the combustion of the molten metal. In addition, the alloys, with their close packed hexagonal crystal structures, are more difficult to deform plastically, compared with Al alloys having cubic crystal structures. Because of this, the conventional production process (Casting of large-diameter bar → Extrusion → Forging) requires many forming steps, which increases the production cost. In order to expand the applications of Mg alloys, their production cost must be decreased.

With this background, we have developed a new technology for producing forging stocks with fine crystal grains that are effective in improving plastic formability, by continuous casting with excellent productivity (i.e., Casting of small-diameter bar → Forging).

This paper introduces the forging characteristics of the cast alloy and the technology for continuously casting the small-diameter bars.

1. The characteristics of Mg alloys having long-period stacking ordered structure

Lately, a Mg alloy with an adequate addition of rare earth elements and Zn has been discovered to have an atomic arrangement called the long-period stacking ordered structure and has become the subject of studies[1]. This long-period stacking
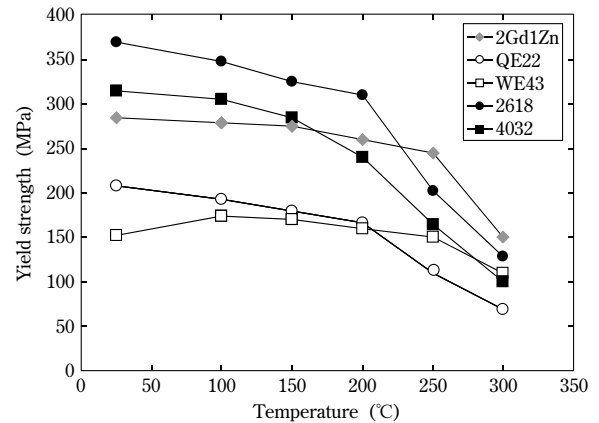
Fig. 1 Yield strengths of various Mg and Al alloys

ordered Mg alloy consists of two phases, one being a phase with a long period stacking ordered structure that accompanies the concentration modulation precipitated by heat treatment at an elevated temperature, and the other being the α-Mg phase. The phase with the long period stacking ordered structure is thermally stable and exhibits excellent mechanical properties as a result of kink deformation caused by plastic forming. Kobe Steel participated in the "Collaboration For Regional Entities for the Advancement of Technological Excellence (Basic Technology Research and Development of Next-generation Heat-resistant Magnesium Alloys)", led by the Japan Science and Technology Agency (JST) from 2006 to 2011, and aims at making a long-period stacking ordered Mg alloy, Mg-2Gd-1Zn [at%] (Mg-11.5Gd-2.4Zn [wt%]), into a product[2].

Fig. 1 shows the data comparing the proof strengths of the conventional heat-resistant Mg alloys, QE22 and WE54, and heat-resistant aluminum alloys, 2618 and 4032, with the newly developed alloy. The newly developed alloy has greater strength than those of the conventional heat-resistant Mg alloys in the range from the ambient temperature to 300℃ and, above 250℃, becomes superior to the heat-resistant Al alloys, whose strength starts to decrease at that temperature. The newly developed alloy is expected to be used for parts that require heat resistance and light weight.

2. The effect of grain size on the formability and strength of the newly developed alloy

The newly developed alloy, Mg-2Gd-1Zn-0.2Zr

[at%], was melted and cast to study the effect of grain size, an influential factor in formability. Forging stocks with different grain sizes were prepared by changing the cooling rate and addition of Zr, a grain refining agent. The forging stocks were heated at 520℃ for 2h, quenched in 80℃ water, and subsequently held at 400℃ for 1h (a process hereinafter referred to as "pre-forging heat treatment"). The materials were used to study the effect of forging conditions on formability and strength.

2.1 The effects of the cooling rate and grain refining agent on the grain size

Forging stocks of different grain sizes were prepared at four levels; i.e., two levels of cooling rate (sand mold and copper mold) and two levels (the addition and non-addition) of a grain refining agent (hereinafter referred to as "Zr"). The sand mold and copper mold each had an inner diameter of 65mm and a height of 200mm. **Fig. 2** shows the cooling curves during casting using the sand mold and copper mold. A sheathed thermocouple with a diameter of ϕ 1mm was used for the temperature measurement and the cooling rate was defined by the solidification rate of the liquid phase. The cooling rates were 0.017℃/s for the sand mold and 0.34℃/s for the copper mold. **Fig. 3** shows how the cooling rate and the addition / non-addition of Zr affects the grain size. **Fig. 4** shows the microstructures (grain size) of the materials cast at the different cooling rates with/without Zr. As the effect of the increased cooling rate, the grain size decreased from 2,800μm to 840μm for the material without Zr, and from 130μm to 57μm for the material with Zr added. The size of the coarse primary crystals (Mg3Gd phase), observed at the triple points of the grain boundaries, was largely affected by the cooling rate and decreased from approximately 25μm to approximately 7μm with the increase of the cooling rate from 0.017℃/s to 0.34℃/s.

Fig. 3 Effect of cooling rate and Zr on grain size
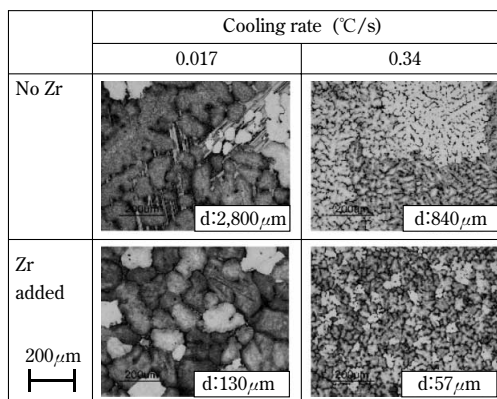
Fig. 4 Microstructures for each cooling rate and Zr addition (as-cast)

2.2 The effect of the cooling rate and grain refining agent on formability

Forging tests were conducted on solid cylindrical samples having a diameter of ϕ 60mm. Each sample was upset-forged by a hydraulic press in its axial direction with three levels of reduction ratios, 50%, 65%, and 80%, at a forging temperature of 380℃. The formability was evaluated by the appearance of each sample after the forging on three levels. **Table 1** summarizes the results of the formability evaluation, in which "×" designates the fact that at least one crack was observed on the top/bottom surface(s); "△", that at least one crack was observed on the lateral face; and "○", that no crack was observed. The formability was found to be improved by increasing the cooling rate from 0.017℃/s to 0.34℃/s. The addition of Zr also turned out to improve the formability.

Microscopic observation was performed to clarify the effects of the cooling rate and Zr addition on the microstructure. **Fig. 5** shows the microstructures of the samples after the pre-forging heat treatment. Although the primary crystals at the grain boundaries have been dissolved into the solid solution by the pre-forging heat treatment, they have

Fig. 2 Cooling curves of sand mold and copper mold

been refined by the increased cooling rate; the same phenomenon was observed in the as-cast material. On the basis of the fact that the fracture surface of the heat-treated material after forging exhibits grain boundary cracks (**Fig. 6**), the primary crystals remaining on the grain boundaries are considered to be the factor influencing formability. In other words, the refinement of the grain size and primary crystals on the grain boundaries, the refinement caused by the increased cooling rate, is considered to prevent the cracks from originating at the primary crystals in the pre-forge heat treated sample, leading to improved formability. It is also considered that, even though the effect of the Zr addition on the size of the primary crystals on the grain boundaries is smaller than that of the cooling rate, its grain refining

Table 1 Influence of cooling rate and Zr on formability

Cooling rate (℃/s)	Grain refiner	Reduction ratio		
		50%	65%	80%
0.017	No Zr	Good	Poor	Poor
	Zr added	Excellent	Excellent	Poor
0 34	No Zr	Excellent	Poor	Poor
	Zr added	Excellent	Excellent	Good
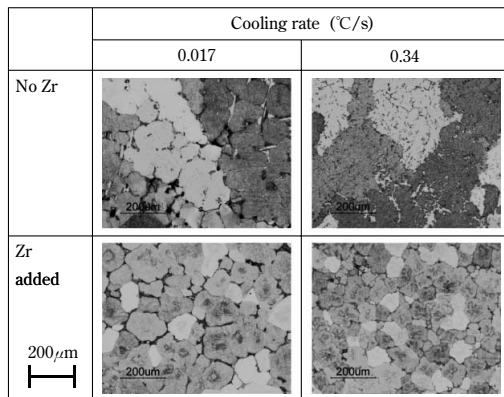
Fig. 5 Microstructures for each cooling rate and Zr addition (heat treated)

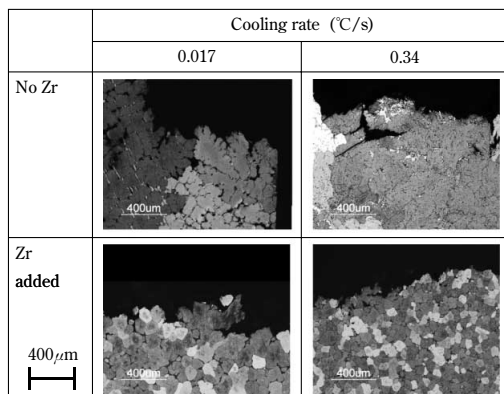Fig. 6 Fracture surfaces for each cooling rate and Zr addition (heat treated)
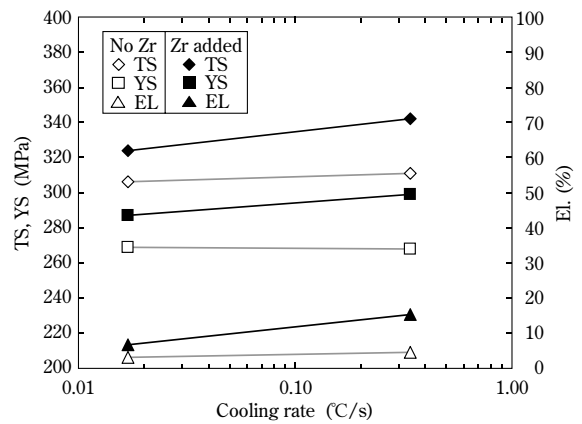
Fig. 7 Effect of cooling rate and Zr on mechanical property (forged)

effect has increased the ductility, further improving the formability.

2.3 The effect of the cooling rate and grain refining agent on strength

Fig. 7 show the results of tensile tests conducted on the samples, with and without Zr, solidified at different cooling rates and forged at a reduction ratio of 80%. An increased cooling rate caused the samples without Zr to exhibit a slight increase in tensile strength and elongation, while it caused the samples with Zr to significantly improve in proof strength, as well as in tensile strength and elongation. For example, in the case of the material with Zr, an increase in the cooling rate from 0.017℃/s to 0.34℃/s caused the proof strength to increase slightly from 287MPa to 299MPa, while causing the elongation to increase significantly from 6.6% to 15.4%. This effect exerted on the elongation by the cooling rate and Zr addition agrees with their effect on formability as described in Section 2.2.

3. The effect of the forging condition on the formability and strength of the newly developed alloy

Because most Mg alloys have close-packed hexagonal crystal structures with only one sliding plane, (0001), at ambient temperature, they are less formable than aluminum alloys and copper alloys having cubic crystal structures[3].

Hence, a study was conducted on the effect of the forging condition on the formability and strength of the newly developed alloy. A billet of the newly developed alloy was prepared by copper mold casting. The billet was heated at 520℃ for 2h, quenched in water at 80℃ and subsequently heat treated at 400℃ for 1h before forging.

3.1 The effect of the pressing speed on formability and strength

In order to confirm the effect of the pressing speed, forging tests were conducted using a mechanical press and hydraulic press at a forging temperature of 350℃ for three levels of reduction ratio, 30%, 50% and 80%. The pressing speed was 250mm/s for the mechanical pressing and 5mm/s for the hydraulic pressing. **Table 2** summarizes the result of the formability evaluation performed in the same manner as described in Section 2.2. With a pressing speed of 250mm/s, cracking occurred at a reduction ratio as small as 30%, while, at a pressing speed of 5mm/s, the forging continued without cracking, up to a reduction ratio as high as 50%. **Fig. 8** shows the results of the tensile test conducted on the samples pressed at different speeds with a reduction ratio of 30%. It should be noted that the elongation value of the sample pressed at 250mm/s was excluded because the sample failed outside the gauge length. The sample pressed at 250mm/s has a strength lower than that of the sample pressed at 5mm/s.

3.2 The effect of the forging temperature on formability and strength

Fig. 9 shows the photographs of samples hydraulically pressed at 300℃, 350℃ and 400℃ under a constant reduction ratio of 80%. Cracking occurred throughout the surface of the sample forged at 300℃, while the sample forged at 400℃ exhibited cracking on only its lateral face, indicating improved formability with increasing forging temperature. **Fig.10** shows the mechanical properties of the samples hydraulically forged at 350℃ and 400℃ with a reduction ratio of 80%. The effect of the forging temperature on the elongation is small, and the lower the forging temperature, the higher the tensile strength and proof strength. The proof strength of the sample forged at 400℃ is approximately 240MPa, while that of the sample forged at 350℃ increases to approximately 290MPa.

3.3 The effect of the reduction ratio on formability and strength

Fig.11 shows the samples hydraulically pressed at a constant forging temperature of 350℃ with varying reduction ratio of 30%, 50% and 80%. The sample was forgeable without cracking, up to the reduction ratio of 50%, however, it exhibited cracking at the reduction ratio of 80%. **Fig.12** shows the results of the tensile tests conducted on the

Table 2 Effect of press speed on formability

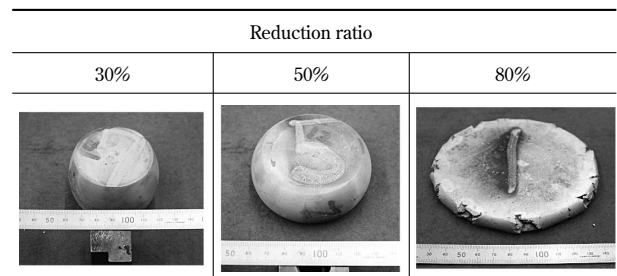| Press speed (mm/s)	Reduction ratio		
	30%	50%	80%
250	Good	Poor	—
5	Excellent	Excellent	Poor
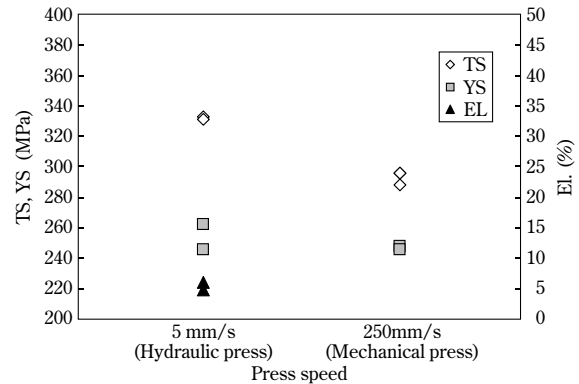
Fig. 8 Effect of press speed on mechanical property

Fig. 9 Effect of forging temperature on formability

Fig.10 Effect of forging temperature on mechanical properties

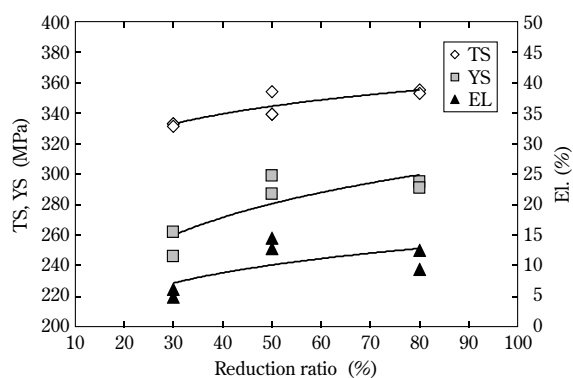Fig.11 Effect of reduction ratio on formability

Fig.12 Effect of reduction ratio on mechanical properties

samples forged at different reduction ratios. The reduction ratio tends to have a proportional relationship with the mechanical properties, with the proof strength being approximately 260MPa for the reduction ratio of 30% and increasing up to approximately 290MPa for the reduction ratios of 50% and 80%.

4. Continuous casting technology

Continuous casting is roughly classified into the vertical type and the horizontal type. The vertical type is a method in which the casting is done in the direction of gravity. As a result, this method is less likely to cause macro segregation, yields superior internal quality, and can be used to cast billets with large diameters. On the other hand, the horizontal type allows cutting of the billet during casting, enabling fully continuous operation, improving the yield and productivity. Above all, this method is less costly because it requires less expensive equipment without the need for a pit. The horizontal type was adapted to develop the technology for producing small forged parts because, in terms of cost, this method is more advantageous for the mass production of billets with small diameters. **Fig.13** schematically shows the horizontal type continuous casting machine used for the prototype production.

The following compares the continuous casting technology for the newly developed Mg alloy and the continuous casting technology for Al alloys that has been developed and used for production by Kobe Steel.

4.1 Melting yield

Unlike Al alloys, molten Mg alloys are extremely reactive and easily react with oxygen in the air and burn. In order to prevent the metal loss caused by the burning and by the carrying of the metal by covering flux, the molten metal is protected by inert gas from the holding furnace to the tundish. Ensuring the airtightness of the furnace and tundish, as well as ensuring an adequate inert gas replacement, has achieved a melting yield no lower than 95%.

4.2 The casting speed and surface quality

The casting speed directly affects productivity, and the higher the speed, the better. The process of continuous casting, however, requires a balance between the casting speed and the solidification rate of the molten metal cooled by the mold, which limits the casting speed. A casting speed that is low enough in comparison with the solidification rate enables casting. However, an excessive cooling capacity of the mold increases the surface rippling of the billet; this problem is intrinsic to horizontal type continuous casting, which increases the stock removal by peeling.

Table 3 compares the physical properties of Mg and Al. Magnesium has a specific heat greater than that of Al and also has a density that is far smaller than that of Al, which makes the volumetric specific heat of Mg somewhat smaller. In order to ensure a reasonable casting speed and smooth cast surface, the mold must be designed to have a cooling capacity that matches the properties of Mg alloy and must be built with a carefully selected material. **Fig.14** shows

Fig.13 Horizontal continuous casting machine

Table 3 Physical properties of Mg and Al

Material	Density (kg/m^3)	Specific heat (J/kg/K)	Volumetric specific heat (J/m^3/K)	Latent heat (kJ/kg)
Mg	1,738	1,050	$1,825 \times 10^3$	368
Al	2,700	920	$2,484 \times 10^3$	385

Mold type	A	B	C
Surface appearance 10mm			
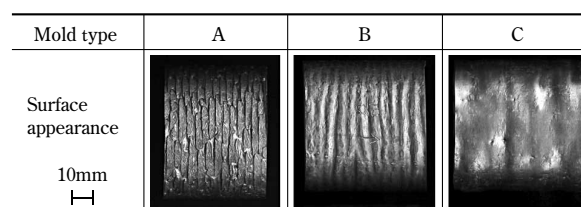
Fig.14 Influence of mold material on billet surface appearance

examples of the surface appearance of billets cast in three types of molds made of different materials. Mold A, which has a higher cooling capacity, results in a deeply rippled surface, while mold C, having a lower cooling capacity, results in a smoother surface.

4.3 The formability of the continuously cast billets

In order to confirm the formability of the continuously cast material, the newly developed alloy was cast into billets with diameters of ϕ 65mm and ϕ 168mm. The billets were pre-forging heat treated as described previously and forged at 380℃ with three reduction ratio levels, 50%, 65%, and 80%. A hydraulic press was used for the forging. **Table 4** summarizes the results of the formability evaluation conducted according to the method previously described. Compared with the larger diameter billet, ϕ 168mm, the smaller diameter billet, ϕ 65mm, has a better formability almost equal to that of the material cast in the copper mold with the addition of Zr, the material that exhibited the highest formability, as described in Section 2.2. **Fig.15**

Table 4 Effect of each continuous casting diameter on formability

Casting diameter	Reduction ratio		
	50%	65%	80%
ϕ 65mm	Excellent	Excellent	Good
ϕ 168mm	Excellent	Good	Poor

	Casting diameter	
	ϕ65mm	ϕ168mm
×100 200μm	d：42μm	d：50μm
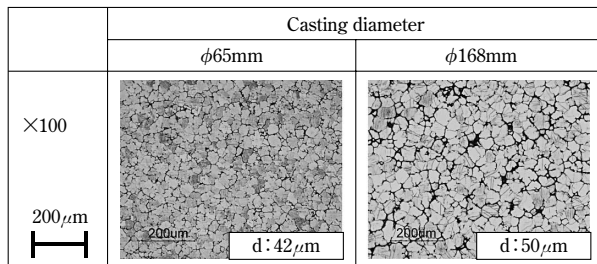
Fig.15 Microstructure for each continuous casting diameter (as-cast）

shows the microstructures of the cast billets having diameters of ϕ 65mm and ϕ 168mm. The grain size is rather small, as small as approximately 50μm, regardless of the billet diameter; however, the size of the primary crystals on the grain boundaries has been decreased from 11μm to 6μm by reducing the diameter from ϕ 168mm to ϕ 65mm. This is considered to have caused the improvement in formability by preventing cracks originating from the remaining primary crystal as an effect of the pre-forging heat treatment described in Section 2.2.

Conclusions

This paper describes a heat-resistant Mg alloy newly developed for transportation equipment. In particular, attention was focused on the alloy's characteristics, its forging technology, the continuous casting of small diameter billets for low cost production, and the formability of the billets. Kobe Steel recognizes the newly developed Mg alloy as a future weight reduction material ranking next to aluminum alloys and strives to resolve issues, including cost, to satisfy the users' needs and to expand the scope of its application.

References

1) Y. Kawamura. *Journal of Japan Institute of Light Metals.* 2004, Vol.54, No.11, p.503-504.
2) Japan Science and Technology Agency. *Basic Technology Research and Development of a Next-generation Heat-resistant Magnesium Alloys.*
   http://www.jst.go.jp/chiiki/kesshu/kadai_shoukai/c-h18-kumamoto/c-h18-kumamoto.pdf (accessed 2012-03-05).
3) The Japan Magnesium Association. *Handbook of Advanced Magnesium Technology. 1st Editi*on. Kallos Publishing Co. Ltd., 2000, p.490.

A New Copper Alloy, CAC5, with Excellent Stress Relaxation Resistance for Automotive Electrical Connectors

Dr. Koya NOMURA [*1]
[*1] Copper Rolled Products Plant, Chofu Works,. Aluminum & Copper Business

Many studies have been made of the Cu-Ni-Sn-P alloy system to develop a copper alloy for automotive electrical connectors because the scraps of the alloys are recyclable in the automotive electronics market. One remaining issue is that of controlling stress relaxation resistance in this alloy system. We have studied the effect of each alloying element on the stress relaxation resistance. The Cu-Ni-P alloy exhibits a higher resistance than either the Cu-Ni alloy or Cu-P alloy. This is probably because pairs that are formed between P and Ni atoms cause a drag force on moving dislocations. Annealing the P containing Cu based alloy for stabilization has improved the stress relaxation resistance. The result indicates that P, segregated at dislocations, decreases the density of mobile dislocations. A suitable combination of these effects enables the copper alloy, CAC5, to be used for automotive connectors even after long exposure to a high temperature environment.

Introduction

The packaging densities of electrical and electronic devices have been continuing to increase as the devices become smaller and their performance is multi-functionalized and upgraded. In line with this trend, connectors are required to be smaller. The greatest factor in downsizing the connectors is the performance of the conductive springs that form electrical contacts inside the connectors. When copper alloy springs are used in automotive environments, they are exposed to temperatures higher than the ambient temperature, which promotes stress relaxation and decreases the holding force of the springs. As a result, year by year there has been an increasing need for copper alloys with high resistance against stress relaxation for use in electrical terminals.

We have developed a copper alloy, CAC5, having stress relaxation resistance that satisfies the current requirements for automotive mounting. The newly developed alloy contains elements such as Ni, Sn, and P, which have conventionally been added to copper alloys, and it achieves said feature by the combination of an optimum composition and heat treatment. This paper reports on the mechanism at work as these additional elements increase the stress relaxation resistance.

1. The stress relaxation phenomena of electrical terminals

Fig. 1 schematically shows the cross-sectional front view and side view of a typical female box terminal. A connector consists of an array of such terminals in a housing. In the case of the example shown in the figure, a copper sheet is press punched and bent into a box shape. The surface of the copper sheet may be coated with a metal such as tin or gold, depending on the use environment and purpose.

The most important function when putting together terminals to be used as a connector is to maintain the contact force of the spring contact for an extended period of time for stability in keeping as low as possible the contact electrical resistance between the spring contacts and male terminal tabs.

The contact force, however, may decrease as time elapses, even when the displacement of the spring contact (*d-t* in Fig. 1) remains constant, as in the case where a male tab is inserted into the spring beam of the female (Fig. 1). This is due to the decreasing stress inside the spring exerting the contact force. The major factors accelerating this decrease in stress are the temperature and the amount of stress in the initial state. In the example shown in Fig. 1, the pre-use clearance, *d*, increases with the passage of time and approaches the thickness, *t*, of the male tab. This phenomenon, called "stress relaxation", requires special attention when using parts such as automotive connectors in high temperature environments.

The resistance against this stress relaxation must be increased for stability in keeping the contact electrical resistance as low as possible. The electrical contact resistance, R_c, is roughly expressed as $R_c \approx \rho \sqrt{\dfrac{H}{F_N}}$, wherein ρ is the electrical conductivity of
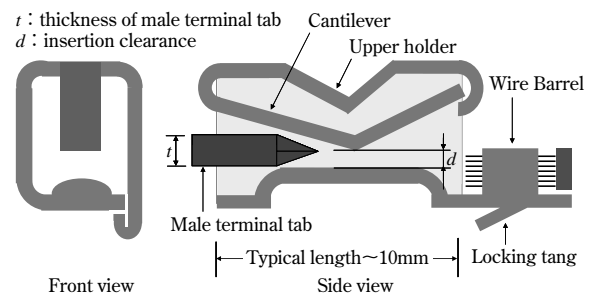

t : thickness of male terminal tab
d : insertion clearance

Fig. 1 Cross section shape of female terminal

the material constituting the surface, F_N is the vertical reaction force (contact force) pressing the contact against the surface, and H is the hardness of the surface. In the example shown in Fig. 1, F_N is approximated as $F_N = -k(d-t)$, in which t is the thickness of the male terminal tab, d is the insert clearance of the female terminal and k is the spring constant.

The testing methods for the stress relaxation characteristic are standardized in ASTM E328, EMAS3003 and in Japan Copper and Brass Association Technical Standard (hereinafter JCBA-T309)[7]. Methods for directly measuring the change in contact force are available; however, in most cases, the ratio of the permanent deflection displacement against the initial deflection displacement of a spring contact is used to calculate the stress relaxation rate. **Fig. 2** depicts the most common cantilever method for testing the stress relaxation characteristic. A copper alloy specimen has a thickness, t, Young's modulus, E, determined from the cantilever deflection, and 0.2% proof strength, $\sigma_{0.2}$. The specimen deflects d in the span of l, deflected, for example, by a spacer, and is heated. Typically, the test is conducted at 150℃ for 1,000 hours. An acceleration test, used, for example, for alloy development, may be conducted at 180℃ for 24 hours. When the specimen is mounted, l and d are adjusted such that the maximum stress of the outermost surface becomes approximately 80% of the proof strength[7]. The specimen is dismounted after a predetermined heating time. The permanent deflection displacement, δ, remaining in the specimen at this time, is the change caused by the stress relaxation, and the stress relaxation rate, SRR(%), is defined by $SRR = \dfrac{\delta}{d} \times 100$: the smaller the stress relaxation rate, the higher the stress relaxation resistance and the better the performance of the spring.

In the initial state, the deflection displacement of the beam does not contain the permanent deflection displacement, δ. Therefore, the deflected beam returns elastically to the original state as soon as the male
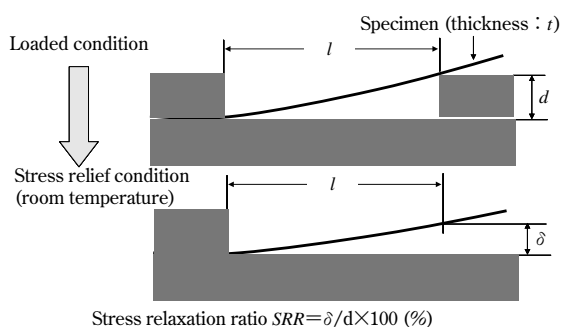
tab is pulled out. Once the stress relaxation occurs, however, the deflected beam does not return to the original state even when the male tab is pulled out, leaving a permanent deflection displacement. This indicates deterioration in the elastic performance of the spring that is expected to exert a force proportional to the deflection displacement of the beam. The amount of the stress relaxation is determined by converting this permanent deflection displacement to the stress.

2. The background of the development of the CAC5 alloy

Age-hardenable copper alloys, such as beryllium copper alloy, have an excellent stress relaxation resistance[1, 2]. However, copper alloys used for automotive applications are required to be recyclable and easy to manufacture on a mass scale. The conventional copper alloys, such as brass, which has been widely used in this field, and phosphor bronze, which has been used mainly in European vehicles, have become unable to respond to the recent need for the stress relaxation characteristic[3-5].

It was with this background that Kobe Steel started to develop technologies for increasing the stress relaxation resistance of copper alloys that contain Ni, P and Sn as major alloying elements. Such an alloying composition allows melting and reusing, as-is, of the recycled scraps of tin plated sheets, especially the highly heat-resistant tin plated sheets with Ni underplating, and helps to conserve resources. CAC5 is an alloy in which the major alloying elements described above are optimized for balancing stress relaxation resistance, mechanical properties and electrical conductivity. The alloy has the typical composition of Cu-0.8wt% Ni-1.2wt% Sn-0.07wt% P.

3. How elements contained in CAC5 affect the stress relaxation phenomenon

3.1 The effect on the stress relaxation resistance

The addition of Sn to the copper alloys increases the stress relaxation resistance, but not to the extent of satisfying the requirement for automotive mounting[6]. This effect is considered to be caused by the Cu and Sn atoms, which have a large atomic radius ratio and form the Cottrell atmosphere that pins dislocations[5]. As for the addition of Ni, attempts were made to improve the stress relaxation resistance, and it has turned out that the ratio between the additive amounts of Ni and P is important in realizing that characteristic. When the stress relaxation rate is

Fig. 2 Schematic illustration of cantilever stress relaxation test

Loaded condition

Specimen (thickness：t)

l

d

Stress relief condition (room temperature)

l

δ

Stress relaxation ratio $SRR = \delta / d \times 100$ (%)

small, as in the case of CAC5, yield points were found to appear at both the ambient temperature and a temperature (200℃) that is close to the automotive mounting environment. In this case, serrated flow is also found to appear. **Fig. 3** shows the stress-strain relationships at these two temperatures for various Ni and P composition ratios. It should be noted that these stress-strain curves were measured on specimens that had been fully recrystallized such that the yield points and the serrated flow appeared clearly. The stress relaxation rates in the figure are values obtained by measuring the final products. The stress relaxation resistance improves in certain ranges of Ni and P addition and their ratio for a given amount of Sn. On the basis of the discovery described above, a study was conducted on the effect of the addition of Sn, Ni and/or P on the stress relaxation characteristic.

3.2 Experimental method

The following compositions were prepared: 99.99% Cu, Cu-1.5% Ni alloy, Cu-1.5% Sn alloy, Cu-0.75% Ni-0.75% Sn alloy and the same alloys with a 0.14% addition of P. The alloys not containing P are hereinafter referred to as "alloys without P", and the alloys containing P, as "alloys with P". All percent (%) designations represent the atomic percent. The cast metals were homogenized, cold rolled by 50% and annealed at 650℃ for 5 min. After the annealing, all the alloys exhibited recrystallization structures with a grain size of approximately 10μm. The annealed samples were cold rolled further by 40%, and some

of the samples were subjected to a low temperature annealing at 300℃ for 30s.

Transmission electron microscope (TEM) specimens were prepared from the samples annealed at 650℃ for 5 min, and the TEM observation was conducted at an accelerating voltage of 200kV. The conductivity represents the average of ten values measured by a conductivity meter using an eddy current method.

Plate-type tensile specimens, each having shoulders and a parallel portion with a dimension of $20^l \times 6^w \times 0.25^t$ mm, were prepared from the samples such that the longitudinal direction of the parallel portion became parallel to the rolling direction. These specimens were tensile tested in a temperature range from 20℃ to 250℃ at an initial strain rate of 3×10^{-3} s^{-1}. Also prepared was another set of specimens, each having a span length of 30mm and a longitudinal direction parallel to the rolling direction. These specimens were subjected to the stress relaxation test in accordance with the cantilever method of JCBA-T309[7]. Each of these specimens was initially deflected such that its surface stress became equivalent to 80% of the 0.2% proof strength at the ambient temperature. These specimens were held in a nitrogen atmosphere at 180℃ for 24h, and the stress relaxation rate was determined by measuring the permanent deflection displacement.

3.3 Experimental results

3.3.1 Strength and conductivity

Table 1 shows the mechanical properties and

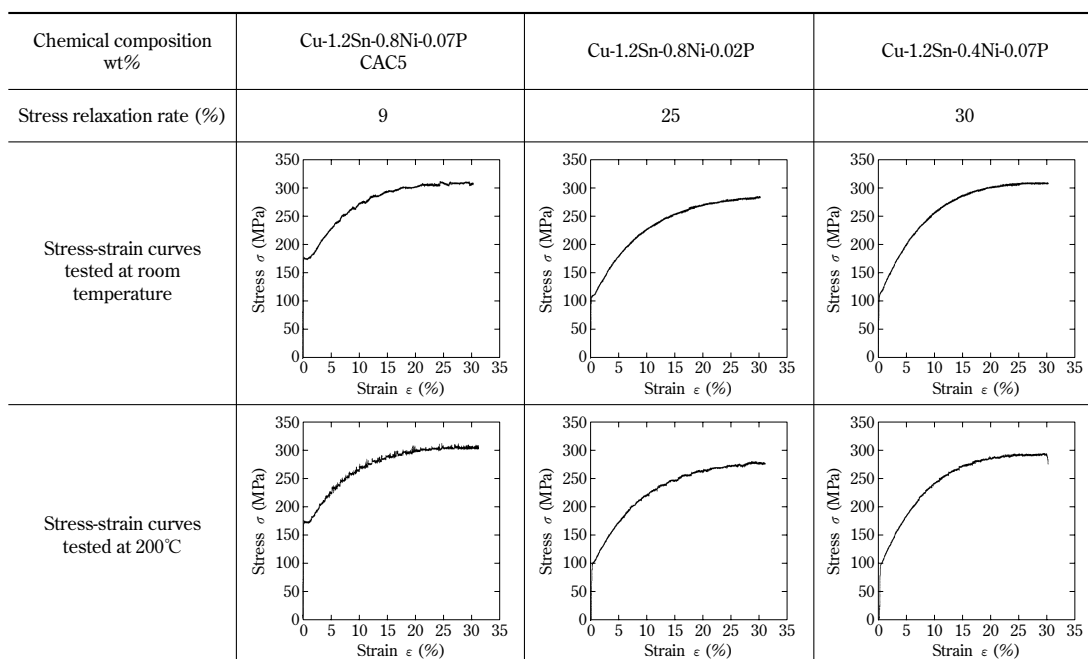| Chemical composition wt%	Cu-1.2Sn-0.8Ni-0.07P CAC5	Cu-1.2Sn-0.8Ni-0.02P	Cu-1.2Sn-0.4Ni-0.07P
Stress relaxation rate (%)	9	25	30
Stress-strain curves tested at room temperature			
Stress-strain curves tested at 200℃			

Fig. 3 Relationships between stress relaxation rates and stress-strain curves for annealed CAC5 and similar composition alloys, tested at room temperature and 200℃

Table 1 Mechanical properties and electrical conductivity of specimens

Specimen	0.2% proof stress (MPa)	Elongation (%)	Electrical conductivity (%IACS)
Cu-(0.14P)	150 (290)	10 (8)	100 (65)
Cu-1.5Ni-(0.14P)	350 (380)	4 (4)	48 (41)
Cu-0.75Ni-0.75Sn-(0.14P)	370 (410)	6 (6)	36 (33)
Cu-1.5Sn-(0.14P)	410 (470)	8 (8)	28 (25)

Fig. 4 TEM image of $Ni_{12}P_5$ particles in Cu-1.5Ni-0.14P alloy before cold rolling by 40% reduction

conductivity of the alloys with and without P. Each value in parenthesis represents the measurement result for each alloy containing P. The addition of Sn to pure Cu results in a solid solution strengthening, and the amount of this strengthening is greater than that contributed by the Ni addition. The combined addition of Ni and Sn results in an intermediate value. The addition of P to the pure Cu and to the three alloys increases their proof strengths. The elongation is decreased by the addition of Ni and/or Sn, with Ni addition resulting in a greater decrease than Sn addition. The combined addition of Ni and Sn results in an intermediate decrease. The conductivity of the alloys without P decreases with the increasing amount of Sn and Ni additives. The contribution per unit concentration of Sn to the resistivity of Cu is $2.8 \times 10^{-8} \Omega$m, which is greater than that of Ni, $1.2 \times 10^{-8} \Omega$m[8]. The conductivity of the alloys without P, estimated from these values, substantially matches the experimental values shown in Table 1. The addition of P to these alloys decreases their conductivity.

In the metallographic structure observation using a TEM, spherical particles having a diameter of approximately 15nm were observed only in the alloy containing both Ni and P (**Fig. 4**). The analysis based on energy dispersive X ray spectroscopy and selected area diffraction patterns has clarified that these particles are an intermetallic compound of $Ni_{12}P_5$[9]. The volume fraction of the $Ni_{12}P_5$ phase is estimated to be approximately 0.002, from the conductivity measurement and the contributions of Ni and P to the resistivity of Cu. This indicates that approximately 1/3 of the 0.14% of added P is contained in the precipitated phase. On the basis of the fact that the volume fraction of the $Ni_{12}P_5$ particles is rather small and their sizes are relatively coarse, the contribution that the $Ni_{12}P_5$ particles make to the strength is considered to be small.

According to Fleischer and Friedel's theory concerning solid solution strengthening, the increment, τ_m, of the critical shear stress of a binary alloy exhibiting solid solution strengthening depends on the solute atom concentration, c, and the atomic radius ratio, ε, of the solute atom against the matrix atom, and is expressed by the following equation[10), 11)]:
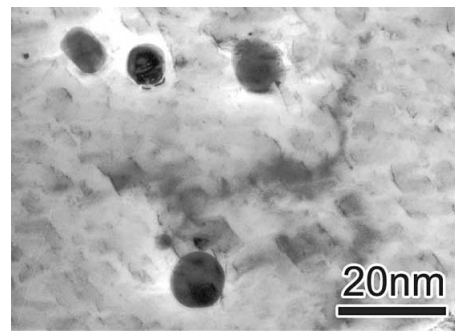
$$\tau_m \propto |\varepsilon| c^{1/2} \quad \cdots\cdots\cdots\cdots\cdots\cdots\cdots\cdots\cdots\cdots (1)$$

The atomic radius ratios of Sn and Ni against Cu are +13.8% and −2.3%, respectively[12)], the atomic radius ratio of Sn being greater than that of Ni. This explains the results, shown in Table 1, that an increase in the additive amount of Sn increases the amount of solid solution strengthening. The atomic radius ratio of P against Cu is large, −14.8%[12)], hence the strength improvement brought about by the addition of P is considered to be mainly attributable to the solid solution strengthening by P.

3.3.2 Stress relaxation characteristic

The stress relaxation rates of the alloys with and without P are shown in **Table 2**. The values in parentheses in the left column represent the amounts of P added to the test materials, while the ones in the middle and right columns represent the stress relaxation rates of the alloys with P. The middle column shows the stress relaxation rates of the as-cold-rolled materials, while the right column shows the stress relaxation rates of the material annealed at 300℃ for 30sec after the cold rolling. Comparing the values in the middle column, the single addition of Ni to pure Cu has almost no effect on the stress relaxation rate, while the addition of Sn, as well as the combined addition of Ni and Sn, decreases the stress relaxation rate. The addition of P to pure Cu, or to the alloy with Ni, significantly decreases the stress relaxation rate. The stress relaxation rate of the alloy with the single addition of Sn remains unchanged regardless of the addition of P. As far as the effect of the additive elements is concerned, these tendencies seen in the right and middle columns are almost the same. A comparison is made between the middle and right columns. After annealing, the stress relaxation rate decreases regardless of the composition; however, the rate for the alloys without P changes less, before and after the annealing. When P is added, the stress relaxation rate is smaller after annealing than it was before annealing.

Stress relaxation phenomena are considered to be creep phenomena caused by the movement of dislocations for relatively short distances[13], and are largely affected by the mobility of the dislocations. The mobility of dislocations generally decreases once the Cottrell atmosphere is formed by the solid solution atoms. This is known to often cause a serrated flow to appear on the stress-strain curves[14, 15]. The serrated flow, as shown in Fig. 3, is considered to be caused by the Cottrell atmosphere formed by the Sn, Ni and P atoms in the solid solution. Hence, the tested materials are also expected to exhibit a serrated flow in their stress-strain curves. With this in mind, the cold rolled material of the each alloy was tensile tested at 180℃. The results are shown in **Fig. 5** and **Fig. 6**. The alloy added with Ni alone does not show any serrated flow. While the alloys containing Sn show serrated flow and the increasing amount of Sn addition causes the stress amplitude of the serrated flow to increase. On the other hand, the addition of P to Cu causes no serrated flow to appear, and the addition of P to the Cu-Sn alloy has almost no effect on the stress

Table 2 Stress relaxation rate of specimens before and after annealing at 300℃ for 30s, tested at 180℃ for 24h

Specimen	Stress relaxation rate (%)	
	Before annealing	After annealing
Cu-(0.14P)	50 (34)	45 (32)
Cu-1.5Ni-(0.14P)	45 (20)	42 (16)
Cu-0.75Ni-0.75Sn-(0.14P)	28 (23)	26 (15)
Cu-1.5Sn-(0.14P)	23 (23)	20 (18)

Fig. 5 Stress-strain curves of specimens tested at 180℃

Fig. 6 Stress-strain curves of specimens tested at 180℃

amplitude of the serrated flow. However, Ni and P, coexisting in the alloy, cause the serrated flow to appear. Therefore, the improvement brought about in the stress relaxation resistance by the addition of Sn, as well as the combined addition of Ni and P, is considered to be caused by the formation of the Cottrell atmosphere, which increases the viscous resistance against the movement of dislocations.

3.4 Discussions

3.4.1 The effects of Ni and Sn

As described in Section 3.3.2, the addition of Ni to pure Cu has almost no effect on the stress relaxation rate, and the addition of Sn improves the stress relaxation characteristic. This is understood to be caused by the formation of the Cottrell atmosphere, contributing to an increase in the viscous resistance, on the basis of the fact that the Cu-Ni alloy does not show any serrated flow during the tensile test at 180℃, while the Cu-Sn alloy shows a serrated flow. The drag resistance, τ, exerted on the dislocations and caused by the Cottrell atmosphere, is given by the following equation[16]:

$$\tau = \frac{\alpha A^2 cv}{bDkT\Omega} \quad \cdots\cdots\cdots\cdots\cdots\cdots\cdots\cdots \quad (2)$$

wherein α is a constant, Ω is the volume per solute atom, b is the magnitude of Burgers vector, c is the concentration of the solute, D is the diffusion constant of the solute atom, v is the velocity of mobile dislocations, k is the Boltzmann's constant, T is the temperature, and A is given by the following:

$$A = \frac{4(1+\nu)}{3(1-\nu)} Gb\varepsilon R^3 \quad \cdots\cdots\cdots\cdots\cdots\cdots\cdots \quad (3)$$

wherein ν is the Poisson's ratio, R is the radius of the solute atom, G is the modulus of rigidity, and ε is plastic strain. According to Equations (2) and (3), τ depends on ν, c, ε and D.
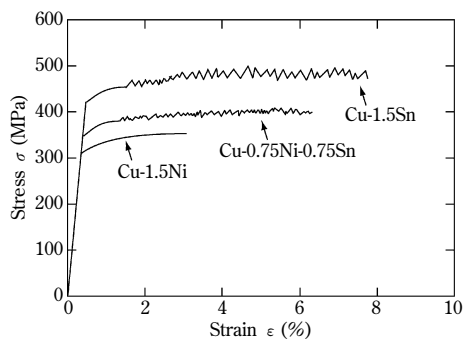
The stress, $\Delta\sigma$, which is parallel to the longitudinal direction of the specimen and is relaxed during the stress relaxation test, is expressed as follows, using the Young's modulus, E, and the plastic strain, ε, caused by the plastic strain:

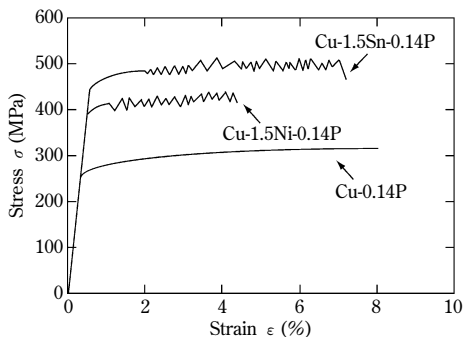$$\Delta\sigma = E\varepsilon \quad \cdots\cdots\cdots\cdots\cdots\cdots\cdots\cdots\cdots \quad (4)$$

Now, the stress providing the initial deflection displacement and the stress required for providing the permanent deflection displacement are calculated to determine $\Delta\sigma$ from the difference between them. The Young's modulus, E, is determined to be 128GPa from the slope of the elastic region in the stress-strain curve of each alloy. These values were used to determine the average plastic strain rate, ε, and v was roughly estimated from the relationship, $\varepsilon = \rho bv$. Here, the initial dislocation density, ρ, was assumed to be

the same for all the alloys and to be $\rho = 10^{15} \text{m}^{-2}$. The magnitude of the Burgers vector was assumed to be $b = 2.6 \times 10^{-10}$m. The result indicates that the velocity, v, of the mobile dislocation is in the order of 10^{-16}ms^{-1} regardless of the types of the alloys.

A comparison is made between the drag viscous resistances of the Cu-Ni and Cu-Sn alloys. Values are placed in the above described v and Equations (2) and (3); i.e., $\nu = 0.33$; $G = 5.2 \times 10^{10}$Pa; and, for the atomic radii (R) of Sn and Ni, 1.41×10^{-10}m and 1.25×10^{-10}m are used, respectively[12]. Using the atomic radius ratio, ε, in Equation (1) gives $A = 1.37 \times 10^{-30}$ Nm^2 and $A = 1.14 \times 10^{-29}$Nm^2 for Cu-Ni and Cu-Sn alloys, respectively. Using these values, as well as the diffusion constants in Cu at 180℃ of Sn and Ni, $D = 2.31 \times 10^{-27} \text{m}^2\text{s}^{-1}$, $1.65 \times 10^{-31} \text{m}^2\text{s}^{-1}$ [4, 12], $\alpha = 4$, $c = 0.015$, $k = 1.38 \times 10^{-23} \text{JK}^{-1}$, and the aforementioned b, gives the drag viscous resistance at 180℃, $\tau = 1.1 \times 10^{33}$Pa for the Cu-Sn alloy and $\tau = 3.4 \times 10^{36}$Pa for the Cu-Ni alloy. As shown, the Cu-Ni alloy has a greater drag viscous resistance. On the other hand, the Cottrell atmosphere is formed only when the velocity, ν, of a mobile dislocation is greater than the critical velocity, v_0, as expressed by the following Equation 5 [17].

$$v \leq v_0 \equiv \frac{3 + 2\sqrt{2}}{2} \frac{AD}{kTb^2} \quad \cdots\cdots\cdots\cdots\cdots\cdots\cdots (5)$$

From Equation (5), v_0, at 180℃ is estimated to be $1.8 \times 10^{-16} \text{ms}^{-1}$ for the Cu-Sn alloy and $1.6 \times 10^{-21} \text{ms}^{-1}$ for the Cu-Ni alloy. Comparing these values with $v \approx 10^{-16} \text{ms}^{-1}$ obtained from Equation (4), the Cu-Sn alloy yields a similar value, while the Cu-Ni alloy yields a v_0, value that is significantly smaller. This indicates that, in the Cu-Sn alloy, the Cottrell atmosphere is formed by the Sn solute atoms, providing resistance to the movement of dislocations, while in the Cu-Ni alloy, no Cottrell atmosphere is formed. The reason for this significant difference is that the Sn atoms diffuse in the Cu matrix much more easily than do the Ni atoms. The Sn atoms move at a velocity in the same order of magnitude as the velocity of mobile dislocations, so that their chances for interaction are much greater than those of the Ni atoms that are essentially immobile.

From the above, it is understood that, at 180℃, the Ni solute atoms in the Cu-Ni alloy do not exert any drag resistance against the movement of dislocations and make little contribution to the improvement of stress relaxation resistance. It is concluded, on the other hand, that the Sn solute atoms in the Cu-Sn alloy cause the Cottrell atmosphere to be formed, decreasing the stress relaxation rate.

As shown in Fig. 5, an increasing additive amount of Sn increases the stress amplitude of the serrated flow. According to Russell[18], the stress amplitude of the serrated flow is proportional to the solute concentration. Also, Equation (2) shows that the drag resistance, caused by the Cottrell atmosphere and exerted on dislocations, is proportional to the solute concentration. Hence, it is understood that an increased additive amount of Sn increases the viscous resistance of dislocations and, as a result, improves the stress relaxation resistance.

3.4.2 The effect of P

The addition of P to Cu slightly improves the stress relaxation resistance; however, it does not cause the serrated flow to appear (Fig. 6). The v_0 value for the Cu-P alloy was estimated in a manner similar to that previously described. On the basis of $A = 6.42 \times 10^{-30}$Nm^2, the diffusion constant at 180℃ of P in Cu, $D = 6.33 \times 10^{-23} \text{m}^2\text{s}^{-1}$ [4], and the above described values for b and k, the v_0 value at 180℃, $v_0 = 2.8 \times 10^{-12} \text{ms}^{-1}$, was obtained. This v_0 value is greater than the aforementioned $v \approx 10^{-16} \text{ms}^{-1}$. Hence it is judged that, at 180℃, the Cottrell atmosphere is formed by the P atoms in the Cu-P alloy. However, the drag resistance, τ, of the Cu-P alloy is given as $\tau = 2.7 \times 10^{28}$Pa, which is remarkably smaller than the $\tau = 1.1 \times 10^{33}$Pa of the Cu-Sn alloy. This implies that the drag resistance provided by the P atoms and exerted on dislocations is very small, making the P atoms move along with the dislocations. If this is true, a serrated flow is expected to appear on the stress-strain curve obtained from the tensile test conducted on the Cu-P alloy at a temperature lower than 180℃. With this in mind, the Cu-0.14% P alloy was tensile tested at 50 and 100℃; however, no serrated flow appeared on the stress-strain curve. Since this result was considered to be attributable to the small additive amount of P, an alloy with an increased additive amount of P, Cu-1.5% P alloy, was tensile tested at temperatures of 50, 100 and 180℃. The resultant stress-strain curve is shown in **Fig. 7**. The serrated flow appeared only at 100℃, with no serrated flow observed at 50℃ and 180℃. At 180℃,
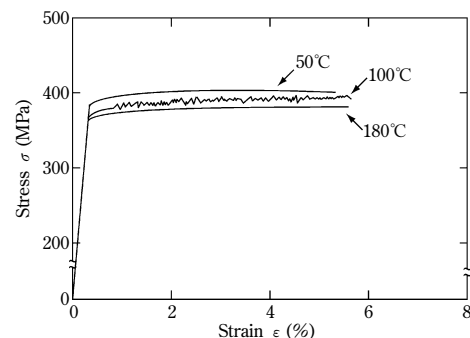
Fig. 7 Stress-strain curves for Cu-1.5P alloy, tested at 50, 100 and 180℃

the P atoms diffuse faster than mobile dislocations. As the temperature lowers, chances increase for the P atoms to interact with dislocations, causing the serrated flow to appear. When the temperature becomes even lower, the diffusion rate decreases, decreasing the opportunity for the atmosphere to form around the dislocations, making the serrated flow less likely to appear. Because of the small drag resistance, the addition of P is regarded as making a small contribution to the improvement of stress relaxation resistance.

The single addition of Ni or of P to Cu has little effect on the stress relaxation characteristic (Table 2). On the other hand, the coexistence of Ni and P in Cu significantly improves the stress relaxation characteristic, causing serrated flow to appear on the stress-strain curve (Fig. 5). It has been known that Ni and P form various compounds in Cu[19] and, as described in Section 3.3, $Ni_{12}P_5$ precipitates were confirmed to be formed in the present alloy. Hence, it is considered that, with P and Ni having strong affinity in Cu, the P atoms moving with dislocations and the Ni atoms in the solid solution provide resistance against the movement of dislocations through their chemical affinity[20]. Precipitates can be the source of resistance against dislocations that have just started to move. The stress relaxation, however, has already started to occur at this point in time; thus, the precipitates are considered to contribute almost nil to the improvement of the stress relaxation resistance of the present alloy.

3.4.3 The effect of the final heat treatment

In the case of the alloy without P, annealing at 300℃ for 30s after the 40% rolling does not cause any significant improvement in the stress relaxation resistance. On the other hand, the alloy with P shows a remarkable improvement (Table 2). As described previously, stress relaxation phenomena are regarded as creep phenomena caused by dislocations moving for short distances[13], and the stress relaxation characteristic depends significantly on the density of mobile dislocations. At 300℃, P has a greater D compared with Ni or Sn and also has a large atomic radius ratio, ε. Hence it is considered that dislocations are pinned by the P atoms during the annealing. It is reported that solid solution type Al-Mg alloys exhibit yield points on their stress-strain curves due to the pinning of dislocations by Mg[21]. With this in mind, the alloys with P were tensile tested at 180℃ before and after the annealing. **Fig. 8** shows, as an example, the stress-strain curves of the Cu-1.5% Ni-0.14% P alloy before and after the annealing. A yielding point is observed for the
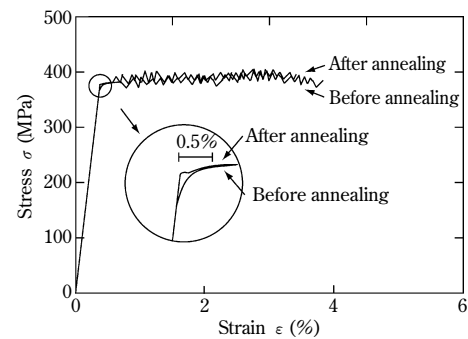

Fig. 8 Stress-strain curves for Cu-1.5Ni-0.14P alloy before and after annealing at 300℃ for 30s, tested at 180℃

specimen after annealing, while no yielding point is observed for the specimen before annealing. Hence, it is understood that dislocations are pinned by the P atoms during the short-time annealing, decreasing the number of mobile dislocations, leading to the improvement of the stress relaxation resistance.

3.4.4 Summary

(a) The improvement of stress relaxation resistance by the addition of Sn to Cu is attributable to the Cottrell atmosphere increasing the drag resistance of dislocations.
(b) The combined addition of Ni and P into Cu greatly improves the stress relaxation resistance. This is considered to be caused by P and Ni, the later having a strong affinity with P, pinning dislocations and producing a large drag resistance.
(c) For the Cu alloy with P addition, a low temperature annealing increases the stress relaxation resistance. This is considered to be caused by the pinning of dislocations by the P atoms during the annealing and the decreased mobile dislocation density.

Conclusions

In order to clarify the cause of the improved stress relaxation resistance of solid solution strengthening type Cu-Ni-Sn-P alloys, a study was made on the effect of each solid solution element on the dislocation drag resistance. The drag resistance was found to increase, particularly when Ni and P are added in combination. The stress relaxation rate is decreased by the final brief annealing at a low temperature. This is considered to be due to the P, in the solid solution, pinning the dislocations and decreasing the density of mobile dislocations. The above knowledge has been adapted for optimizing the actual production process, which has enabled the development of the CAC5 alloy. The alloy does not

require any heat treatment, such as the precipitation aging required by beryllium copper and Corson system copper alloys, but achieves the same level of stress relaxation resistance as the levels achieved by these alloys.

We will continue to strive to respond to the increasingly sophisticated needs by developing alloys exploiting the special characteristics of the materials.

References

1) T. Usami et al. *J. JCBRA.* 2001, (40), p.294-300.
2) M. Mizuno et al. *J. JCBRA.* 1999, (38), p.291-297.
3) M. Nishihata et al. *Bull. Insti. Metals.* 1993, (32), p.334-336.
4) A. Sugawara et al. *Materia Japan.* 1998, (37), p.271-273.
5) T. Ogura. *J. JCBRA.* 1999, (38), p.274-280.
6) K. Nomura. *J. JRICu.* 2002, (41), p.192-196.
7) Japan Copper and Brass Research Association. *Standard methods for stress-relaxation test for materials and structures.* 2001.
8) S. Komatsu. *J. JRICu.* 2002, (41), p.1-9.
9) M. Murayama et al. *J. Electron Mater.* 2006, (35), p.1787-1792.
10) R. L. Fleischer. *Acta Metall.* 1963, (11), p.203-209.
11) J. Friedel. *Dislocation.* New York, Pergamon Press, 1964, p.378-384.
12) Japan Institute of Metals. *Kinzoku data book,* Maruzen, 2004.
13) E. Sato et al. *J. JILM.* 2005, (55), p.604-609.
14) R. Monzen et al. *Mater.* Sci. Eng. 483-484, 2008, p.427-432.
15) C. Watanabe et al. *J. Mater.* Sci. 2008, (43), p.813-819.
16) S. Takeushi. *Phil. Mag.* 1979, (40), p.65-75.
17) H. Yoshinaga et al. *Phil. Mag.* 1970, (22), p.1351-1365.
18) M. C. Chen et al. *Metall. Mater.* Trans. A. 1994, (27A), p.1691-1694.
19) Y. Yamamoto et al. *J. JRICu.* 2006, (45), p.153-157.
20) The Japan Institute of Metals. *Gendai no Kinzokugaku, Zairyouhen 4, Tekkou Zairyo.* 1985, p.193-195.
21) R. Horiuchi et al. *J. Japan Inst. Metals.* 1965, (29), p.85-92.

Dissimilar Metal Joining Technology Using Newly Developed Aluminum Flux-Cored Wire (FCW) to Join Aluminum Alloy and Steel

Tsuyoshi MATSUMOTO[*1], Tetsu IWASE[*1], Kazumasa KAITOKU[*1], Seiji SASABE[*2], Masatoshi IWAI[*3], Masao KINEFUCHI[*4]

[*1] Technology Control Dept. Aluminum & Copper Business
[*2] Technology Control Dept. Aluminum & Copper Business (currently Japan Light Metal Welding & Construction Association)
[*3] Sheet products Development Dept., Research & Development Lab., Iron & Steel Business
[*4] Materials Research Laboratory, Technical Development Group

We have developed a technology for joining dissimilar metals, an aluminum alloy and steel, using MIG and laser welding equipment. A newly developed aluminum flux-cored wire has been found to suppress the formation of brittle intermetallic compound in the bonding interface and to realize a joint strength that compares with the strength obtained by a similar joint of the aluminum alloy. The corrosion resistance of the welds was evaluated. The butt joint was found not to exhibit any electrolytic corrosion. This technology was used to build prototype car structure members to evaluate their strength and the applicability of the technology.

Introduction

In an effort to reduce global warming, there is an accelerating trend toward automotive weight reduction. To achieve this purpose, it is desirable to use the right material for the right parts so that the intrinsic features of each material are fully exploited. Such use of materials requires an extensive deployment of elemental technologies, including joining, forming and analyzing. Dissimilar metal joining between aluminum alloy and steel is one such elemental technology and is an area where much effort has been made[1]. When joined by conventional welding methods, aluminum alloy and steel form a brittle intermetallic compound (hereinafter, "IMC") of Fe-Al at the joint interface, which deteriorates the joint characteristics. Thus, the joining used to rely on other methods such as mechanical fastening and adhesive bonding.

We have studied the technology for fusion joining between aluminum alloy materials and steel sheets, such as galvannealed steel sheets (hereinafter, "GA steel sheets") and cold-rolled steel sheets (hereinafter, "CR steel sheets"), which are commonly used for automobiles[1]. This paper reports a newly developed technology for joining dissimilar metals, an aluminum alloy and steel, by fusion joining[2]. The technology employs an apparatus for conventional welding, such as metal inert gas (MIG) welding and laser welding, and still produces a joint strength as high as that obtained for the similar joint of aluminum alloys.

1. A study on an aluminum flux-cored wire

1.1 Problems with the conventional flux cored wires

When an aluminum alloy material is welded to a steel material, a brittle IMC is formed at their joint interface, which decreases the joining strength. Therefore, the formation of the IMC must be suppressed to improve the strength properties.

Previous studies on a laboratory scale show that the formation of IMC is somewhat suppressed when conventional aluminum flux-cored wires (hereinafter, "aluminum FCWs") for brazing are used for MIG[3] and laser[4] welding. In those cases, the tensile shear strengths have been achieved that compare with those obtained for the similar joint of aluminum alloys. However, the practical application of aluminum FCWs to the dissimilar metal joint between aluminum alloy and steel has been considered to be difficult due to the buckling of the wires, instability of droplet transfer, excessive slag formation and the lack of joining strength.

We therefore started to solve these problems by developing a new aluminum FCW that is feasible for industrial applications.

1.2 Samples tested

The following samples were tested. For the aluminum materials, aluminum alloy sheets of AA6022P (thickness, 1.0mm and 2.0mm) and extruded shapes of 6061S alloy (wall thickness, 2.2mm and 2.5mm) were used. For the steel materials, a 590MPa class GA steel sheet (thickness, 1.2mm), a 590MPa class CR steel sheet (thickness, 1.2mm), and a 980MPa class CR steel sheet (thickness, 1.4mm) were used. Welded joints were formed mainly by lap fillet welding, in which an aluminum alloy material is placed on a steel sheet and is melted such that the aluminum material forms a joint with the steel sheet. In addition, butt welding joints were made between the aluminum alloy and steel. These joining processes are herein called "braze welding" because they melt the aluminum alloy, but not the steel. To study the suitable sheath
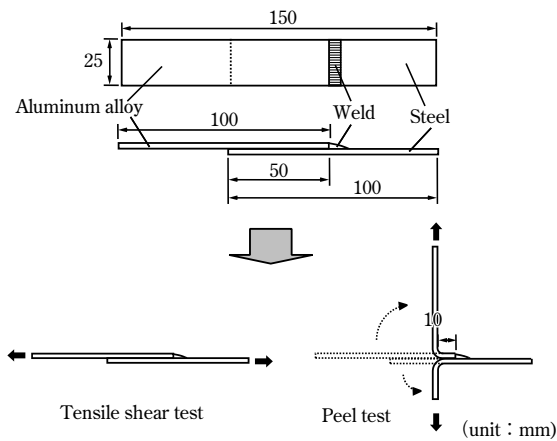
Fig. 1 Methods for evaluating the joint strength[2]

Fig. 2 Comparison of joint strength by the types of aluminum solid wire[2]

Fig. 3 Macro and micro structures of weld shape and interface[7]

composition for the aluminum FCW, solid wires were used to emulate the sheath material, and the aluminum alloy and steel materials were pre-coated with flux. The solid wires used were A5356-WY, A4043-WY and A4047-WY. A new composition was also used as a solid wire. This new solid wire has a composition with decreased Mg and additional Si, the former element being known to preferentially react with fluorides in the flux and result in poor joint quality, and the latter element being expected to improve the wettability of the molten metal.

Next, a lap fillet weld joint was produced between the AA6022P sheet (thickness 1mm) and the 590MPa class CR steel sheet (thickness 1.2mm) by laser braze welding. The welded material was used to prepare the specimen, shown in **Fig. 1**, for joint strength evaluation. The tensile shear strength was evaluated on a joint specimen having an elongated rectangular shape with a width of 25mm, in which the welding bead lies in the transverse direction. The peel strength was evaluated on a specimen prepared from the welded material, in which each elongated rectangular sheet is bent to a right angle at a position 10mm away from the welded end. Both the strengths were evaluated by the breaking load per unit welding length.

1.3 A study on aluminum FCWs

Fig. 2 shows the results of joint strength evaluation. In the comparison of solid wires, the solid wire with the new composition resulted in the highest joint peel strength, while the A5356-WY (Al-Mg series) resulted in the lowest joint strength.

Fig. 3 shows the macrographs of the joint cross-sections and the optical micrographs of the IMC layers formed at the joint interfaces. The weld formed by the A5356-WY exhibited the thickest IMC layer in the present comparison and also exhibited needle-like IMC inside the aluminum welding metal. On the
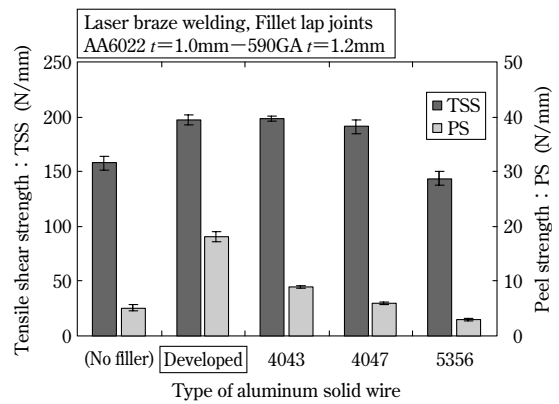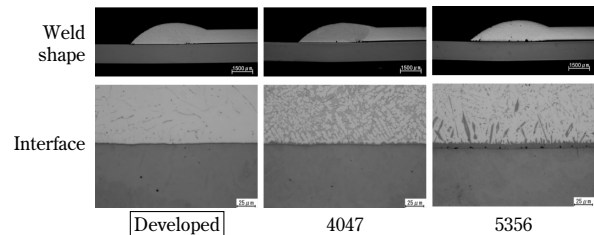
other hand, the A4047-WY and new composition resulted in IMC layers that are thin throughout the interface. In particular, the solid wire with the new composition has been found to distribute the IMC layer the most thinly with an average thickness of approximately $1\,\mu$m.
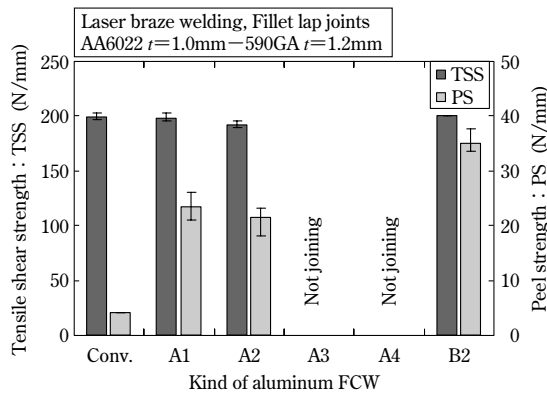
A similar evaluation was conducted on joints formed by MIG braze welding. It turns out that the new composition exhibits the highest joint strength with the thickness of its IMC layer significantly reduced; this is the same phenomenon that was observed for the laser braze welding.

Five types of fluxes (A1-A4, B2) were tested, including the non-corrosive fluoride based flux, NOCOLOK[5], used for the aluminum FCW for brazing (**Table 1**). The criteria for selecting the flux compositions were that the flux should dissolve the film of aluminum oxide, have no influence on corrosion resistance and be easy to fill into the sheath interior. As a result, the mixtures that were selected were based on potassium aluminum fluoride and contained either aluminum fluoride or cesium fluoride. The selected flux was filled into the sheath made of the new composition at an optimized flux-filling ratio to prepare aluminum FCW samples.

These aluminum FCW samples were used to form a lap fillet weld joint between an aluminum alloy sheet and the GA steel sheet. This dissimilar metal joining was performed by laser braze welding. Joint tensile tests were conducted for evaluation. The

Table 1 Combination ratio of flux[2]

Kind of Al. FCW	Combination ratio of flux (wt%)		
	K-Al-F	Al-F	Cs-F
A1	100		
A2	75	25	
A3	50	50	
A4	25	75	
B2	75		25

Fig. 4 Comparison of joint strength by the types of aluminum FCW[2]

Fig. 5 Fracture mode after peel test

Fig. 6 Appearance of welded part

Fig. 7 Relationship between the thickness of IMC layer and joint strength[2]

results are shown in **Fig. 4**. Specimens A3 and A4 exhibit no bonding. Specimens A1, A2 and B2 show similar tensile shear strength. Their peel strengths are B2>>A1>A2 in descending order. **Fig. 5** shows the failure mode of these specimens. Specimen B2 shows a favorable result with its interface remaining intact and the failure occurring in the aluminum alloy. Similar testing conducted on MIG braze welding has revealed that specimen A2 has the highest peel strength.
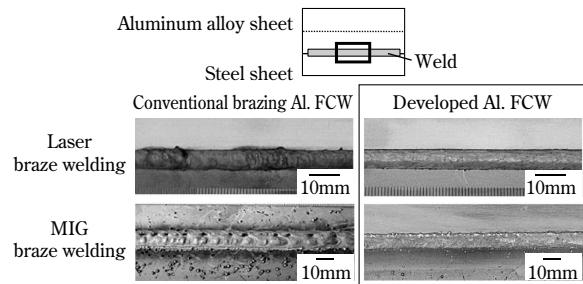
Fig. 6 shows the appearances of welds obtained by laser braze welding and MIG braze welding. The newly developed aluminum FCW exhibits a significantly improved bead appearance compared with the conventional aluminum FCW for brazing.

Fig. 7 summarizes the relation between the joint performance of the dissimilar metal weld joints (between the aluminum alloy and steel) and the thickness of the IMC layer at the joint interface. As shown, the newly developed aluminum FCW suppresses the growth of the IMC, yielding a thinner IMC layer. This suppression of the IMC formation over the entire area is considered to have caused the significant improvement, especially in the peel strength.
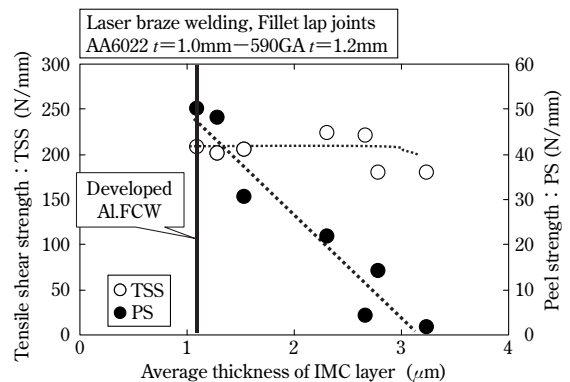
These results have clarified the concept of an aluminum FCW suitable for the dissimilar metal joining of aluminum alloy and steel by laser braze welding and MIG braze welding.

2. Corrosion resistance

In a dissimilar metal joint between an aluminum alloy and steel, the potential difference between the two materials causes a corrosion current to flow. This produces greater corrosion, or contact corrosion, than in the case of similar joints involving aluminum alloys[6].

Thus, the prevention of contact corrosion between dissimilar metals is an important issue in realizing hybrid structures. In the current practice, mechanically fastened joints are completely coated, for example, with paint, structural adhesive and waterproof sealant to secure corrosion resistance. This approach is considered to be effective in preventing the contact corrosion of the welded portions in the present study.

To prove this, a fundamental study was conducted to clarify the effect of painting on the contact corrosion of a joint between an aluminum alloy and steel. Butt welds were prepared for this purpose. The newly developed aluminum FCW was used to butt weld the AA6022P sheet (thickness 2mm) to the 590MPa class CR steel sheet (thickness 1.2mm) by MIG braze welding. The welding end zones, each having a width of 25mm, were cut to prepare test samples. The samples were phosphate treated before electro deposition. The evaluation was done according to the cyclic corrosion test (CCT), JASOM0609, set forth by the Japanese Automotive Standards Organization (JASO). The CCT is a type of acceleration test for evaluating corrosion, in which test cycles are repeated, each cycle consisting of salt spraying twice at 35 ± 1 degrees C, drying 4 times at 60 ± 1 degrees C and moistening twice at 50 ± 1 degrees C.

For a preliminary test, the butt weld sample was painted and subjected to 51 cycles of the test. The tested sample exhibited some red rust near the end of the steel sheet, with the weld portion remaining intact and almost no blistering in the coating. Then, considering harsher conditions, the coating was provided with cross-cuts for corrosion origin, and the sample was corrosion tested for up to 150 cycles. **Fig. 8** shows the appearance of a test sample with cross-cuts after 150 test cycles. The aluminum alloy, on the left side of the weld line in the photo, exhibited almost no blistering, nor white rust. On the other hand, the steel exhibited an increasing amount of blistering and red rust as the CCT proceeded. The welding bead exhibited neither rust nor blistering.

The blistering of the coating was evaluated by applying adhesive tape to the cross-cut portion and peeling it off and by measuring the width of the peeled portion (taping test). As a result, the aluminum alloy side (Fig. 8①) exhibited peeling neither in the vicinity of the weld (Fig. 8②), nor in the weld (Fig. 8③), and exhibited almost no corrosion under the coating. On the other hand, the steel side (Fig. 8④, ⑤) exhibited a significant amount of

corrosion; however, almost no difference was observed in the amount of blistering between portion ④ near the weld line and portion ⑤.

The above results indicate that the corrosion behavior near the joint between the aluminum alloy and steel is not different from that in the portions away from the weld line. In other words, no contact-corrosion occurred between the dissimilar metals in the butt weld joint of the present study. This means that no electrical circuit was created to allow current in the butt weld portion. The reason and mechanisms for this will be the subject of a further study.

3. Prototype examples of the hybrid structure

Dissimilar metal joining, using the newly developed aluminum FCW, was employed to prepare model members, having hybrid structures, for automobiles. The strength of the members was evaluated to study the applicability of the technology. The following introduces examples of the application, according to the results.

3.1 Hat shaped members with closed cross-sections

To simulate an axially loaded member, such as a B pillar, a sample was prepared for an offset axial compression test, as shown in **Fig. 9**[7]. This sample consists of an aluminum alloy shape and steel shape, each having a hat shaped cross-section. These shapes were put together with their open sides facing each other and were joined at their flanges by laser braze welding. The aluminum alloy material used was an A6061S-T6 extrusion (wall thickness of the weld; 2.2mm), and the steel material was a 980MPa class CR steel sheet (thickness 1.4mm). The test sample (total length 900mm) was welded together at three locations on each edge of the aluminum alloy hat by continuous beads, each having a length of 200mm. In the crush test, a hydraulic cylinder was used to apply an axial compressive load on the side plate shown in Fig.9.

Fig.10 shows the load-stroke diagram obtained from the test. The deformation proceeded for a while after the maximum load was reached, before a weld was fractured. The test result indicates that the present welding method is applicable to structural members that are not subject to large deformations.

3.2 Lid-shaped structural members and pipe fastening model members

The following describes an example of lid-shaped members, such as doors and trunk lids, utilizing the dissimilar metal joining between aluminum alloy and steel. Also described is a structural member
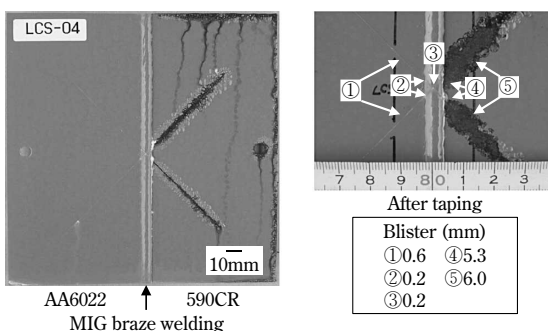

After taping

Blister (mm)	
①0.6	④5.3
②0.2	⑤6.0
③0.2	

AA6022   590CR
MIG braze welding

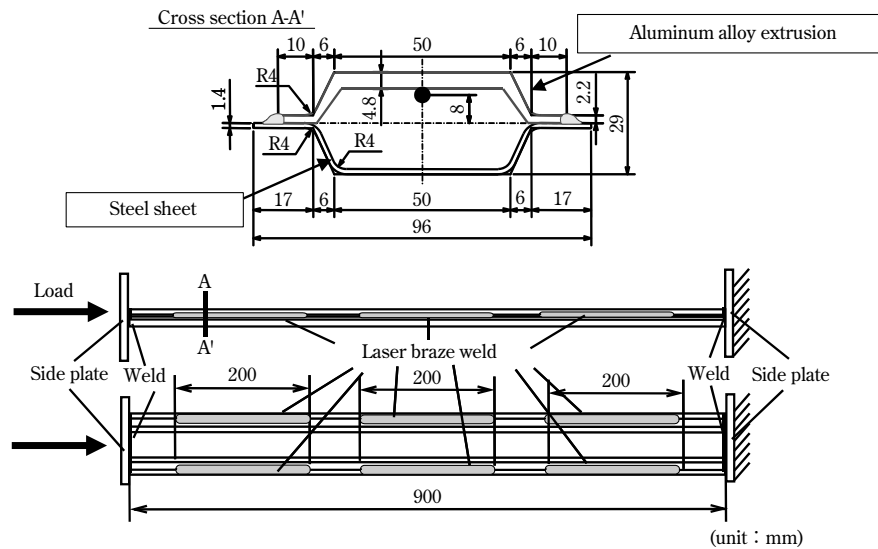**Fig. 8** Corrosion test specimen after 150 cycles[2]
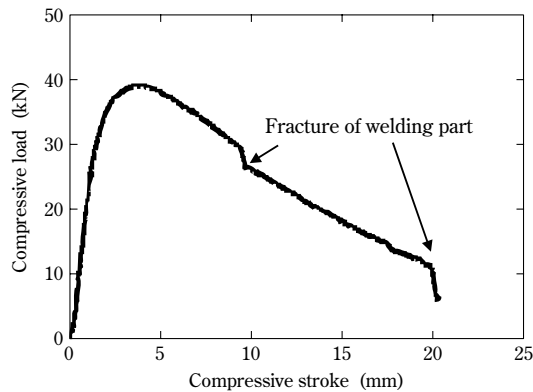
Fig. 9 Specimen for axial crush test[2]

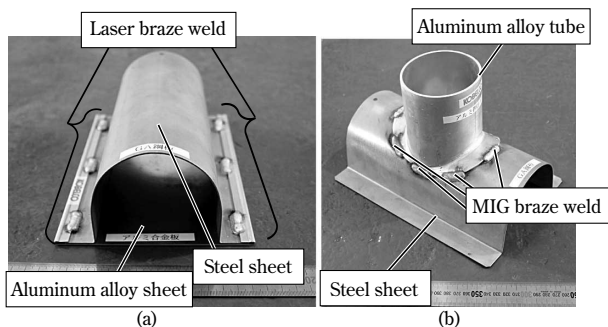Fig.10 Experimental result of the axial crush test[2]

Fig.11 Example of welded parts[8]

modeling a pipe fastener. **Fig.11** (a) shows a lid-shaped member using an AA6022P sheet (thickness 1.0mm) for the outer panel and a 980MPa class GA steel sheet (thickness 1.2mm) for the inner panel[8]. The hem was joined in a stitch-like manner by MIG braze welding.

Fig.11 (b) shows a member in which the flange formed on a A6063S pipe (thickness of the welded portion; 2.5mm) is joined to the center of a bent form made of a 980MPa class GA steel sheet (thickness 1.2mm) by MIG braze welding[8]. Weight reduction is expected in this structure, wherein one of the pipe faster members, both of which used to be steel, is replaced by an aluminum alloy. The members shown in Fig.11 (a), (b) are small samples, but provide examples of basic structures that can be developed into actual members, such as lid-shaped panels and pipe fasteners.

Conclusions

The fusion joining of the dissimilar metals of aluminum alloy and steel has conventionally been difficult. An aluminum FCW has been developed in order to realize this joining. The newly developed FCW was used for braze welding, such as MIG and laser, and achieved favorable joint performance. The corrosion resistance evaluation and the prototype manufacturing of hybrid structures have yielded promising results.

However, new issues may arise in the actual application of the technology. We will strive to bring it to a higher level of quality and expand its applicability so as to contribute to the weight reduction of automobiles.

References

1) New Energy and Industrial Technology Development Organization. *Toward the Prevention of Global Warming / Production & Fabrication Technology Development of Aluminum Useful for Automobile Lightweighting*. (2005-2006). 2007, p.113-227.
2) T. Matsumoto, et al. *Transactions of Society of Automotive Engineers of Japan (Transactions of JSAE)*. 2011, Vol.42, No.2, p.591-596.
3) M. Kinefuchi. *Engineering materials*. 2008, Vol.56, No.10, p.77-83.
4) T. Matsumoto, et al. *Preprints of the National Meeting of Japan Welding Society*. 2006, Vol.79, p.306-307.

5) Japan Light Metal Welding & Construction Association. *Aluminum brazing handbook (in Japanese)*, 2003, p.300.

6) T. Ishihara. *The current issue case histories in corrosion failures analysis and corrosion diagnostics*. 2008, p.169-170.

7) M. Kinefuchi, et al. *Transactions of Society of Automotive Engineers of Japan (Transactions of JSAE)*. 2011, Vol.42, No.2, p.597-602.

8) T. Matsumoto, et al. *Journal of light metal welding*. 2011, Vol.49, No.11, p.35-40.

A Basic Study of Dynamic Recrystallization in Cu-Sn-P Alloy for High Strength Copper

Dr. Masato WATANABE[*1], **Akihiko ISHIBASHI**[*2], **Dr. Hiromi MIURA**[*3]
[*1] Technical Department, Hatano Plant, KOBELCO & MATERIALS COPPER TUBE, LTD.
[*2] Kobelco & Materials Copper Tube (M) Sdn. Bhd
[*3] Department of Mechanical Engineering and Intelligent Systems, Graduate School of Informatics and Engineering, UEC Tokyo
   (The University of Electro-Communications)

Dynamic recrystallization (DRX) behavior in a newly developed Cu-Sn-P alloy was systematically investigated. Hot compression tests were performed on alloy samples having different crystalline conditions, i.e., as-cast coarse-grained polycrystalline and orientation-controlled bicrystals. Also tested were Cu-Sn-P alloys with varying Sn content. As a result of Sn addition, the Cu-Sn-P alloy was found to undergo DRX that is much delayed compared with that of a conventional Cu-P alloy. The delayed DRX is considered to have increased the flow stress and strain required for processing the Cu-Sn-P alloy. When compressed under conditions that are close to the conditions of the actual operation, the alloy was found to exhibit a significantly inhomogeneous microstructure. This structure seemed to be refined and homogenized as a result of static recrystallization during the subsequent cooling period after extrusion. It is concluded that the DRX in Cu-Sn-P alloy is dominated by discontinuous type DRX governed by the annealing twins formed behind the migrating grain boundaries.

Introduction

Phosphorous-deoxidized copper (JIS H3300 C1220) is widely used all over the world for room air conditioners, the heat exchangers of heat-pump water heaters and as a piping material. Lately, the application of a high pressure refrigerant, such as CO_2, and the increased need for cost reduction as a result of the rising price of copper have led to the development and production of high strength copper tubes[1), 2)].

The high-strength copper alloys are materials newly being used for copper tubes and contain elements such as Co and Sn. As a result, they are empirically known to be vastly different in terms of extrudability and the like from phosphorous-deoxidized copper, the pure-type copper in conventional use.

There are 3 types of high strength copper tubes. Among them, the solid solution strengthening type Cu-Sn-P (KHRT[®3)]) is the most difficult material to extrude. This material was selected for the present study and the following 3 types of samples were prepared:

(1) materials with coarse columnar grain structures machined from hot extrusion billets;
(2) bicrystals simulating the above coarse columnar grain structures; and
(3) materials with fine grains containing various amount of Sn.

These 3 types of samples were subjected to hot compression tests to study the details of their dynamic recrystallization behaviors. As a result, systematic and basic knowledge has been obtained on their deformation behavior during hot extrusion, crystal grain refinement by microstructure control, and so on, as reported below.

1. Dynamic recrystallization

We first describe dynamic recrystallization, a consistent theme of the present paper. When a material is deformed in a high temperature region, the dislocation density increases to initiate work hardening, increasing the flow stress. Dynamic recrystallization is a type of recrystallization that is driven by the strain energy and the decrease in dislocation density that occur during the deformation. Hence the dynamic recrystallization results in the formation of new grains containing neither dislocation nor strain, which results in a distinctive phenomenon of work softening.

Fig. 1 shows an example of the typical stress-strain curves associated with dynamic recrystallization during deformation at high temperatures. After an elastic deformation, the flow stress is increased by work hardening caused by the increase in dislocation density and strain energy that takes place during plastic deformation. Then the work hardening
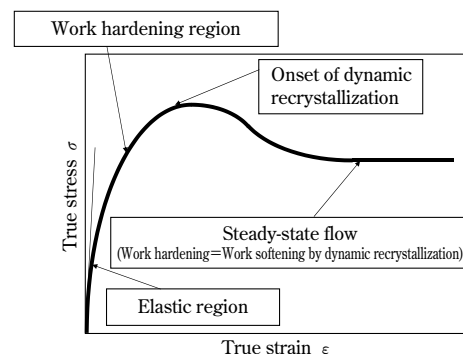
Fig. 1 Typical flow curve in dynamic recrystallization

reaches a peak stress, and an extensive dynamic recrystallization occurs to release the strain energy. This eventually leads to work softening, decreasing the flow stress. Under a yet higher strain, the work hardening balances with the work softening, resulting in a steady state deformation in which the flow stress becomes constant[4)-7)].

Analyzing the tress-strain curves obtained during hot compression and observing the resulting microstructure provide the basic knowledge of, for example, the deformation behavior and grain refinement necessary for tube production and microstructural control.

2. The dynamic recrystallization behavior of the material with coarse grains

2.1 The coarse grain material consisting of columnar crystals

The dynamic recrystallization behavior of a cast material consisting of coarse columnar crystals was studied in order to clarify the change in structure of high-strength copper KHRT during hot extrusion at an actual production site. The process for producing a copper tube includes hot-extruding a cast-billet to produce a mother tube. The cast material comprises chill crystals in the circumference, free crystals in the center and coarse columnar crystals in the major portion of the tube[8), 9)].

Dynamic recrystallization is less likely to occur when the crystal grain is coarser[10)]. This is due to the fact that coarser grains provide a smaller number of grain boundaries that serve as the preferential nucleation sites for recrystallization[11)]. Therefore, the coarse grains (columnar crystals) govern the dynamic recrystallization behavior of the cast structure.

2.2 Experimental method

Two types of samples were used: a phosphorous-deoxidized copper tube, having a composition of Cu-0.025mass% P (hereinafter referred to as "Cu-P"), which has been conventionally and widely used for heat exchanger applications; and a high strength copper tube, KHRT, having a composition of Cu-0.65 mass%Sn-0.025mass%P (hereinafter referred to as "Cu-0.65Sn-P"), which has been newly developed and used commercially. A square rod sample, having a dimension of $6 \times 9 \times 13$mm^3, was machined from the columnar crystal portion of each billet and was subjected to compression testing. The initial grain sizes, determined by a cutting method in accordance with JIS H0501, were 5.8mm for Cu-P and 5.3mm

for Cu-0.65Sn-P. A vacuum high-temperature compression testing machine (Instron type) was used for the compression tests at temperatures of $T = 1,023$ to $1,253$K and a strain rate of $\dot{\varepsilon} = 2.0 \times 10^{-4}$ to 2.0×10^{-1}s^{-1}. Each test was performed until the true strain reached $\varepsilon = 0.8$. As schematically shown in **Fig. 2**, the direction of the compression axis of the columnar crystal sample was set so as to be parallel to the casting direction. Each sample was water-cooled within 1s after the compression test such that the structure formed during the high-temperature working was quenched.

2.3 Experimental results and discussion

Fig. 3 shows the true stress-true strain curves of the Cu-P cast materials compressed at strain rates of $\dot{\varepsilon} = 2.0 \times 10^{-4}$ to 2.0×10^{-1}s^{-1} at a temperature of $T = 1,073$K. The stress-strain curves obtained have a shape resembling the one in Fig. 1, shown as a typical example of dynamic recrystallization. The phenomenon occurring during this time is as explained in Section 1.

Fig. 4 shows the true stress-true strain curves of the Cu-0.65Sn-P cast materials compressed at a temperature of $T = 1,153$K and at strain rates of $\dot{\varepsilon} = 2.0 \times 10^{-4} - 2.0 \times 10^{-1}$s^{-1}. The stress-strain curves have a shape that is different from the one for Cu-P. Firstly, these curves exhibit clear yielding in the initial deformation region, in the vicinity of true strain from 0.02 to 0.06, and subsequently exhibit
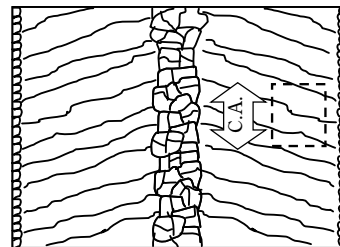

Fig. 2 Schematic illustration of billet in section
Rectangular area of dotted line : columnar structure, C.A. : compression axis
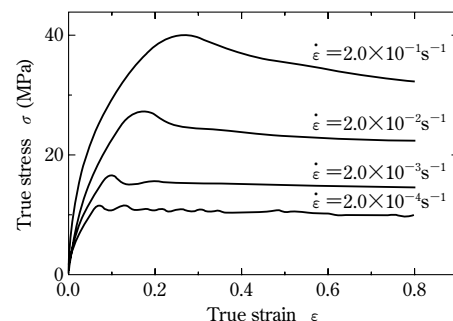

Fig. 3 Flow curves of Cu-P alloy billet samples compressed at 1,073K at various true strain rates
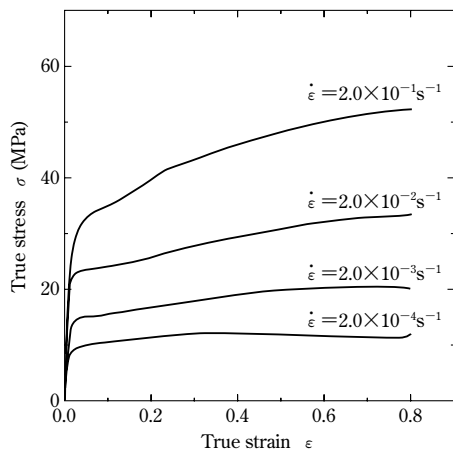
Fig. 4 Flow curves of Cu-0.65Sn-P alloy billet samples compressed at 1,153K at various true strain rates
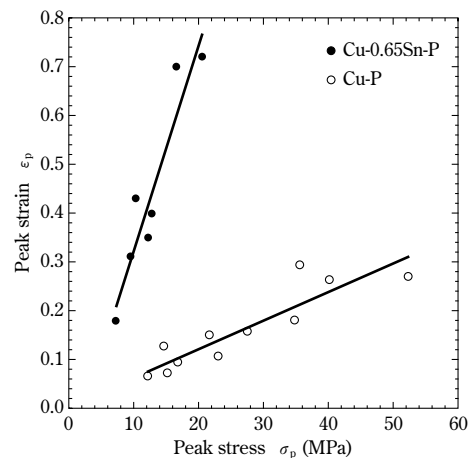

Fig. 5 Relationship between peak stress and peak strain of Cu-0.65Sn-P and Cu-P alloy billet samples
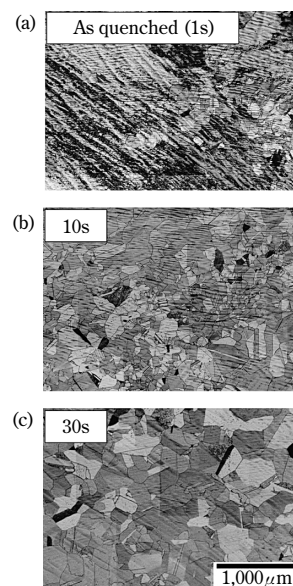

Fig. 6 Microstructure of Cu-0.65Sn-P alloy billet samples deformed to $\varepsilon = 0.8$ at 1,153K at strain rate of $\dot{\varepsilon} = 2.0 \times 10^{-1} s^{-1}$(a), followed by annealing at 1,153K for 10s(b) and 30s(c)

large and significant work hardening. This is considered to be caused by the solid-solution strengthening effect of Sn. Further increase in the strain makes the increase in flow stress moderate, which is considered to be attributable to dynamic recovery/recrystallization. In particular, when the strain rate is as large as $\dot{\varepsilon} = 2.0 \times 10^{-1} s^{-1}$ and $\dot{\varepsilon} = 2.0 \times 10^{-2} s^{-1}$, the results show neither the clear peak stress nor the work softening exhibited by the Cu-P.

Each of the Cu-P and Cu-0.65Sn-P samples was tested at three different temperatures and four different strain rates. **Fig. 5** shows the relationship between the peak stress and peak strain, both obtained from all the true stress-true strain curves. It should be noted that the Cu-0.65Sn-P materials, not showing any peak stress until $\varepsilon = 0.8$, are regarded as having no data for peak stress and peak strain. Furthermore, for the stress-strain curves of Cu-P, in which the curves show more than one peak stress, the value for the stress and strain of the first peak are taken as data.

For both the alloys, the peak stress and peak strain are found to be in a linear relationship regardless of the temperature and strain rate. However, there is a significant difference between the Cu-P and Cu-0.65Sn-P in the slope of the linearity. The slope for the Cu-0.65Sn-P is greater than that for the Cu-P, indicating that the amount of strain that initiates/ induces dynamic recrystallization for Cu-0.65Sn-P is greater than that for Cu-P. This is because the addition of Sn significantly delays the initiation of dynamic recrystallization. This agrees with the rule of thumb, empirically obtained at the manufacturing site, that the mother tube of the high-strength copper, KHRT, Cu-0.65Sn-P, is more difficult to extrude than the conventional phosphorous deoxidized copper, Cu-P.

The Cu-0.65Sn-P was subjected to a compression test at a high temperature of $T = 1,153K$ and $\dot{\varepsilon} = 2.0 \times$ $10^{-1} s^{-1}$ up to a strain of $\varepsilon = 0.8$. The test samples were annealed for either 10s or 30s. The resulting microstructures, as well as the as-quenched structure, are shown in **Fig. 6**. The structure immediately after the hot-working was quite inhomogeneous, showing many deformation zones formed inside the coarse un-recrystallized grains, as well as the development of necklace-like fine grains formed on the old grain boundaries. This structure, however, changed into a finer and almost homogeneous recrystallization structure as the subsequent annealing time was increased. This is considered to be a result of the high dislocation density and strain energy accumulated in the grains and on the grain boundaries serving as a driving force for static recrystallization and making the structure homogeneous. Considering actual extrusion, only certain regions are considered to have

a dynamically recrystallized structure immediately after the extrusion, but the structure is annealed during the subsequent cooling and changes into a perfectly recrystallized structure. These experimental facts provide extremely useful information for microstructure control, or the structural homogenization and refinement, of the actually extruded materials. The fact that the structure contains many annealing twins indicates the occurrence of discontinuous static recrystallization.

3. The dynamic recrystallization behavior of bicrystals

3.1 The bicrystal as a material, simulating cast material

Bicrystals were prepared as simple model materials simulating the cast materials with coarse columnar crystals described in Section 2. The bicrystals were used to study the basics of, for example, the dynamic recrystallization behavior in the vicinity of a grain boundary that is important as the formation site of dynamic new grains.

Grain boundaries and precipitates can serve as preferential formation sites for new grains geometrically and crystallographically. Dynamically recrystallized grains are reported to be formed preferentially on grain boundaries by a bulging mechanism[11), 12)]. The deformation behaviors of, and structural changes in, the grain boundaries and their vicinities, locations playing a very important role in dynamic recrystallization, were systematically studied using the orientation controlled twin crystals prepared to simulate the coarse grain columnar crystals.

3.2 The experimental method

The Cu-0.65Sn-P (high-strength copper tube, KHRT) was used as the base material for the Bridgman method (a method involving a seed crystal prepared by a pull-up method, on which material is sequentially solidified to produce a single crystal having a crystallographic orientation that is the same as that of the seed crystal) to prepare a bicrystal having a [011] twist grain boundary with a grain boundary misorientation of 18 degrees (hereinafter referred to as an "18° bicrystal"). Square rod specimens, each having a dimension of $6 \times 9 \times 12$mm, were machined from the bicrystal by an NC electric discharge machine, such that their grain boundaries became vertical to the compression axis (so as to simulate the columnar crystal being extruded). The specimens were subjected to the high temperature compression test. The test temperature

was set to be $T = 1,073$K and the strain rate to $\dot{\varepsilon} = 2.0 \times 10^{-3}$ to 2.0×10^{-1}s^{-1}, and the tests were conducted until the true strain reached $\varepsilon = 0.2$, 0.5 and 1.0. The specimens were water-cooled within 1s after the compression test so as to quench the structure formed during the high temperature working. Furthermore, the crystal orientations of the deformation microstructures in the vicinity of grain boundaries on the longitudinal section, parallel to the compression axis, were analyzed using a crystal orientation analysis apparatus (Orientation Imaging Microscopy, hereafter "OIM").

3.3 Experimental results and discussion

Fig. 7 shows the stress-strain curves of the 18° bicrystal samples compression tested at a high temperature. It is confirmed that the curve for the lowest strain rate, $\dot{\varepsilon} = 2.0 \times 10^{-3}$s^{-1}, exhibits a peak stress at around $\varepsilon = 0.5 - 0.6$ and subsequent work softening before exhibiting a steady state deformation. On the other hand, the curve for $\dot{\varepsilon} = 2.0 \times 10^{-2}$s^{-1} appears to reach the peak stress at a higher strain around $\varepsilon = 0.8$. The curve for $\dot{\varepsilon} = 2.0 \times 10^{-1}$s^{-1} at one point shows a steady state deformation, but subsequently exhibits work hardening. As the strain rate increases, the stress value becomes higher, implying that dynamic recrystallization is less likely to occur. Comparing Fig. 4 and Fig. 7, despite the 80K difference in testing temperature, the bicrystal exhibit greater stress value for a given strain rate, implying that dynamic recrystallization does not occur on a large scale. This is caused by the relation between crystal grains and dynamic recrystallization from the aspect of the occurrence point, as will be discussed in Section 4.3.

The 18° bicrystals of Cu-0.65Sn-0.025P were compressed at a high temperature under the
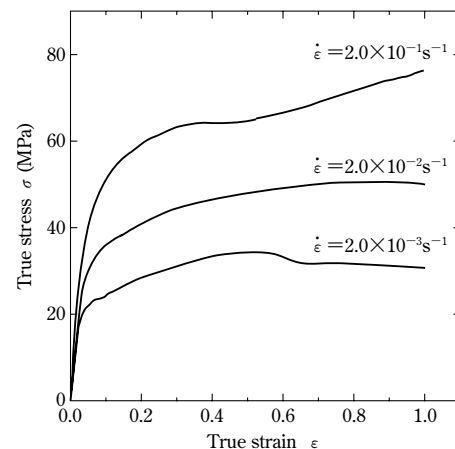

Fig. 7 Flow curves of Cu-0.65Sn-P alloy bicrystal with [011] twist 18° grain boundaries tested in compression at 1,073K at various true strain rates

conditions of strain rate $\dot{\varepsilon}=2.0\times10^{-3}\mathrm{s}^{-1}$ and $2.0\times10^{-1}\mathrm{s}^{-1}$, and a true strain of $\varepsilon=0.2$, 0.5 and 1.0. The samples were water quenched within 1s after the compression to freeze the microstructure. **Fig. 8**[13] shows the result of the OIM observations.

For the strain of $\varepsilon=0.2$, no new-grain was observed to have been formed for any strain rate; however, at a slow strain rate of $\dot{\varepsilon}=2.0\times10^{-3}\mathrm{s}^{-1}$, more significant grain boundary serration was observed to have occurred (Fig. 8 (d)). For the strain of $\varepsilon=0.5$, no dynamically recrystallized grain was observed at the strain rate of $\dot{\varepsilon}=2.0\times10^{-1}\mathrm{s}^{-1}$ (Fig. 8 (b)); however, at $\dot{\varepsilon}=2.0\times10^{-3}\mathrm{s}^{-1}$, dynamically recrystallized grains were observed in the vicinity of grain boundaries (Fig. 8 (e)). For the strain of $\varepsilon=1.0$, the entire region was dynamically recrystallized at $\dot{\varepsilon}=2.0\times10^{-3}\mathrm{s}^{-1}$ (Fig. 8 (f)). On the other hand, for $\dot{\varepsilon}=2.0\times10^{-1}\mathrm{s}^{-1}$, the grain boundary serration is still small, and the dynamic recrystallization has only partially occurred on the grain boundaries and within each grain, resulting in an inhomogeneous structure (Fig. 8 (c)). It is noteworthy that the new grains are formed both on the grain boundaries and inside the parent crystals. Grain boundaries are known to work as preferential formation sites for new grains. Within a grain, on the other hand, deformation zones and the peripheries of precipitates are known to work as preferential nucleation sites of dynamically recrystallizing grains[14), 15)]. It has turned out from the results shown in Fig. 8 that the new grains are formed preferentially on grain boundaries when the strain rate is low and are formed both within grains and on grain boundaries when the strain rate is high. It has also turned out that most of these dynamically recrystallized grains contain twins and multiple twins. This indicates that the dynamic recrystallization behavior is governed by the mechanism of annealing twins, regardless of the high/low strain rate and the difference in the nucleation sites of the dynamically recrystallized grains. In other words, the dynamic recrystallization mechanism is a discontinuous mechanism, in which the subgrain boundaries, formed within parent crystals by old grain boundaries or recovery, migrate, leaving behind twin crystals.

Fig. 9 shows the misorientation between the points shown in Fig. 8 (e) of the 18° bicrystal. From
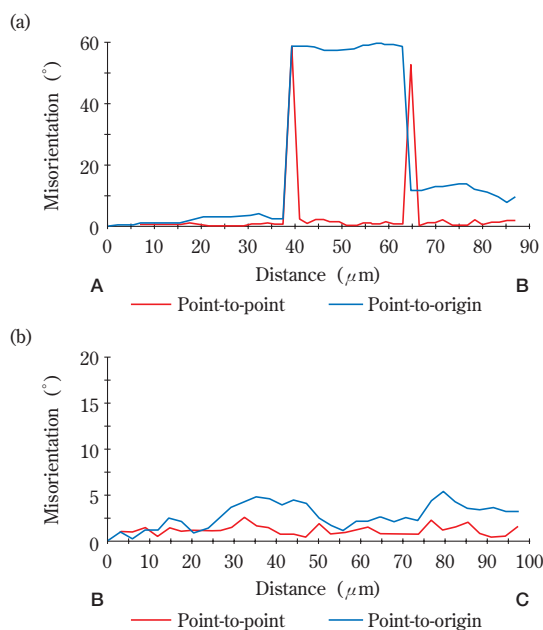

Fig. 9 Change in misorientation change between the points A-B (a) and B-C (b) shown in Fig.8(e)

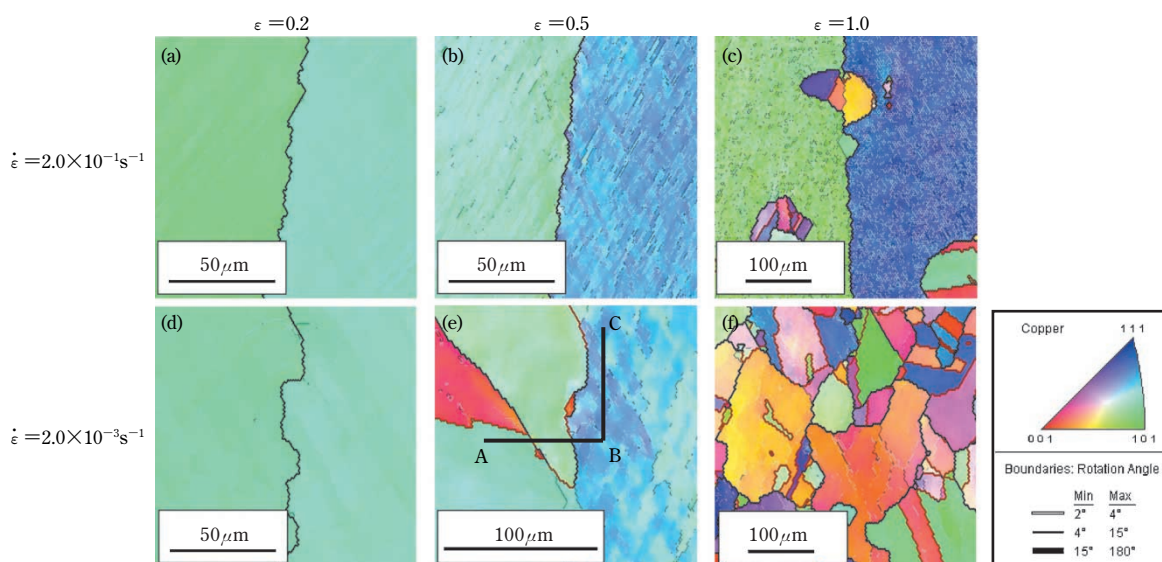
Fig. 8 OIM maps of microstructures in Cu-0.65Sn-P alloy bicrystals having [011] twist 18° grain boundaries deformed to various strains at 1,073K at strain rates of $\dot{\varepsilon}=2.0\times10^{-1}\mathrm{s}^{-1}$ and $\dot{\varepsilon}=2.0\times10^{-3}\mathrm{s}^{-1}$ [13]

the result of misorientation analysis along A-B, the new grains formed on grain boundaries are found to have a large misorientation of approximately 60 degree, indicating that the new grains have a twin crystal relationship with the parent crystal (Fig. 9 (a)). On the other hand, the misorientation in the parent crystal on the line A-B is approximately 5 degrees at maximum. This implies the formation of substructure by the deformation and recovery. In other words, the cross-slip and climb motion of dislocations during deformation causes the simultaneous generation and annihilation of dislocations. The intracellular dislocation structures are considered to indicate the intragranular formation of subgrains having more regular boundaries.

Similarly, the change in misorientation observed in the matrix along the line B-C was within approximately 5 degrees (Fig. 9 (b)). This implies that the gradual dynamic recovery and crystal rotation by slip deformation are induced continuously inside the parent crystals[16]. This is a feature of continuous dynamic recrystallization. The discontinuous dynamic recrystallization is the most important dynamic recrystallization mechanism that occurs in the present alloy and affects its structural change; however continuous dynamic recrystallization is considered to occur simultaneously, contributing to the formation of the substructure as described above.

4. The effect of the additive amount of Sn on the dynamic recrystallization behavior of materials with a fine grain

4.1 Fine grain polycrystalline material

From the results described in Sections 2 and 3, it has been clarified that the Cu-Sn-P alloy exhibits a dynamic recrystallization behavior almost the same as the one exhibited by the copper alloy most generally used[17]. It has been shown that the annealing twins, formed by grain boundary serrations and behind the migrating grain boundaries, causes the preferential formation of new grains on the grain boundaries and necklace recrystallization of the grains[18]. This fact indicates that the discontinuous dynamic recrystallization caused by the formation of annealing twins becomes the governing mechanism, despite the decrease in dislocation mobility and grain boundary migration brought on by the addition of Sn.

However, no systematic study has been conducted on the effect of the additive amount of Sn on the dynamic recrystallization behavior, in which the additive amount of Sn was as low as less than 1%, as in the case of Cu-Sn-P high strength copper, nor on

the effect of the initial grain size. Hence, we have conducted a detailed study as described below.

4.2 Experimental method

The samples tested were Cu-0.66mass%Sn-0.025 mass%P alloy (hereinafter, Cu-0.66Sn-0.025P), the same composition as that of the high strength copper KHRT, and alloys having a higher or lower additive amount of Sn, Cu-0.31mass%Sn-0.024mass%P (hereinafter, Cu-0.31Sn-0.024P) and Cu-1.02mass% Sn-0.025mass%P (hereinafter, Cu-1.02Sn-0.025P). A 99.99% pure copper (hereinafter, 4NCu) was also used as a reference material.

The Cu-Sn-P was melted, casted, hot-rolled and then machined into a round bar. Solid cylinder specimens, each having a diameter of 8mm and height of 12mm, were prepared from this round bar for compression tests. These specimens were vacuum annealed such that they had an equiaxial crystal grain structure with an average grain size of 200μm.

These specimens were compression tested at temperatures of $T = 1,073 - 1,213$K and strain rates of $\dot{\varepsilon} = 2.0 \times 10^{-4}\text{s}^{-1} - 2.0 \times 10^{-1}\text{s}^{-1}$, until the true strain became $\varepsilon = 1.0$. Each specimen was water-cooled within 1s after the compression test. A vacuum, high-temperature compression testing machine (Instron type) was used for the compression test.

4.3 Experimental results and discussion

The specimens of the three Cu-Sn-P alloys with different additive amounts of Sn and 4NCu were compression tested at a strain rate of $\dot{\varepsilon} = 2.0 \times 10^{-1}\text{s}^{-1}$ and a temperature of $T = 1,073$K. The results are shown in **Fig.10**. The 4NCu clearly exhibits work softening, indicating the occurrence of dynamic recrystallization. The work softening is indistinct for the Cu-Sn-P alloys and an increasing amount of Sn enhances this trend. An increasing amount of Sn increases the maximum value of the true stress, with both the peak strain and peak stress shifted towards the high strain side.

Fig.11 shows optical micrographs of the structures obtained by the high temperature compression up to a strain of $\varepsilon = 1.0$, each corresponding to each stress-strain curve in Fig.10. The 4NCu shows dynamically recrystallized coarse grains that are homogeneous and equiaxial, indicating that sufficient dynamic recrystallization occurred throughout the area. On the other hand, the Cu-Sn-P alloys show new grains that are finer than those of the 4NCu. Furthermore, a large portion of the Cu-1.02Sn-0.025P alloy, which contained the largest amount of Sn, remained unrecrystallized (Fig.11(d)). This result indicates an
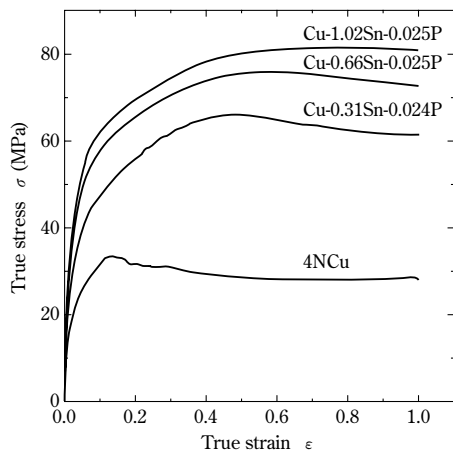
Fig.10 True stress vs. true strain curves of Cu-Sn-P alloys with different Sn content and 4NCu when compressed at $\dot{\varepsilon}=2.0\times10^{-1}\mathrm{s}^{-1}$ at 1,073K
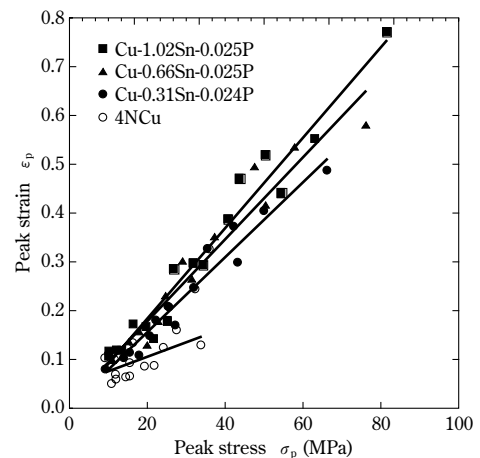

Fig.12 Relationship between peak flow stress and peak strain of Cu-Sn-P alloys and 4NCu
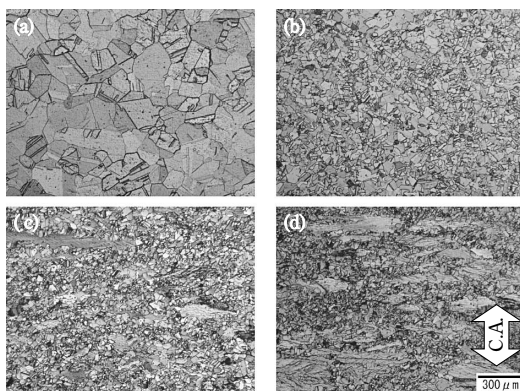

Fig.11 Microstructures in specimens deformed to $\varepsilon=1.0$ at a strain rate of $\dot{\varepsilon}=2.0\times10^{-1}\mathrm{s}^{-1}$ at 1,073K; (a) 4NCu, (b) Cu-0.31Sn-0.024P, (c) Cu-0.66Sn-0.025P, (d) Cu-1.02Sn-0.025P
C.A.：compression axis

insufficient occurrence of dynamic recrystallization. The area of the unrecrystallized region decreases with a decreasing additive amount of Sn. Now, Fig.11 is compared with Fig.6 (a). Despite the slight difference in conditions, it is clear that new grains are more widely generated when the initial structure is finer.

The relationships between the peak stress and peak strain for the Cu-Sn-P alloys and 4NCu reference material were obtained from all the stress-strain curves of the high temperature deformation (**Fig.12**). All of the Cu-Sn-P alloys and 4NCu exhibit almost linear relations regardless of the temperature and strain rate. The slope becomes steeper as the additive amount of Sn increases, with a vast difference between the 4NCu without Sn and the Cu-Sn-P alloys. This clearly shows that the addition of Sn delays the occurrence of dynamic recrystallization in relation to the peak strain. The addition of Sn is considered to have caused a solute drag effect (solute drag resistance) on the dislocation movement,

decreasing the recovery and the moving velocity of grain boundaries. This is judged to have caused the delay of dynamic recrystallization and the resulting crystal grain refinement.

As is clear from the comparison between Fig.5 and Fig.12, the crystal grain refinement facilitates dynamic recrystallization. In other words, the preferential formation of new grains at grain boundaries, clarified in Section 3, promotes the occurrence of dynamic recrystallization even more when the initial crystal grain is finer. This provides the extremely important insight that, by making the initial grain size of the billet material smaller, (1) the flow stress during hot extrusion can be decreased, (2) the extrusion in a lower temperature region at a higher strain rate becomes possible, and (3), as a result, a fine and more homogeneous fine grain structure is obtained.

Conclusions

The present study has clarified a part of the mechanism for dynamic recrystallization behavior in the high strength copper Cu-Sn-P. The following basic knowledge was obtained concerning the deformation behavior and microstructure control of the present alloys during working.

(1) The occurrence of dynamic recrystallization in the cast material of Cu-0.65Sn-P is delayed, compared with that of Cu-P cast material, by the solid solution of Sn, which results in an increase in the maximum value of true stress. This result matches the experience of the extrusion process at the production site.

(2) The dynamic recrystallization behavior of the bicrystal of the Cu-Sn-P alloy depends largely on the strain rate. In other words, when the strain rate is low, new grains are formed

preferentially on the grain boundaries that accompany grain boundary serrations, while, when the strain rate is high, the intragranular formation of new grains is induced by the formation of a slip/shear zone in addition to the formation of the new grains on the grain boundaries.

(3) The dynamic recrystallization behavior has turned out to be governed by the mechanism of annealing twins, regardless of whether the strain rate is high or low and the difference in the formation site of dynamically recrystallized new grains.

(4) The addition of Sn delays the occurrence of dynamic recrystallization and, as a result, increases the peak stress and peak strain of the stress-strain curve. The addition of Sn has caused the refinement of the new grains formed by dynamic recrystallization; however, a large amount of additional Sn limits the occurrence of dynamic recrystallization, which causes a unrecrystallized region to remain.

In areas such as hot extrusion, there is still room for improvement in the high strength copper, when compared with the conventional pure copper, phosphorous-deoxidized copper. It is important to determine the conditions for the process of tube making, with attention to the fundamental knowledge obtained by the present study, giving consideration to the aspects of both workability and microstructure control. It is, furthermore, important that these results be reflected in an improvement in material quality.

It is believed that the achievements of the present study will become an important asset in the alloy extrusion technology at KOBELCO&MATERIALS COPPER TUBE (THAILAND) CO., LTD.

References

1) M. Watanabe et al. *R&D Kobe Steel Engineering Reports.* 2008, Vol.58, No.3, p.74-77.
2) M. Watanabe. *Journal of Japan Research Institute for Advanced Copper-base Materials and Technologies.* 2008, Vol.47, p.7-10.
3) T. Shirai el al. *Journal of Japan Research Institute for Advanced Copper-base Materials and Technologies*, 2004, Vol.43, p.302-306.
4) Y. Watanabe el al. *Materials for mechanical engineering*, Corona Publishing, 2010, p.124-125.
5) S. Takagi et al. *Zairyo Soshiki-gaku, Asakura Pulishing Co., Ltd.*, 2009, p.88-89.
6) T. Sakai. *TETSU-TO-HAGANE.* 1995, Vol.81, p.1-9.
7) T. Sakai et al. *Bulletin of the University of Electro-Communications.* 1993, Vol.6, p.143-156.
8) *Chuzo Gijutu no Kiso.* THE NIKKAN KOGYO SHIMBUN, Ltd, 1968, p.65-86.
9) O. Miyagawa et al. *Kinzoku-gaku Gairon. Asakura Pulishing Co., Ltd.*, 2004, p.59-61.
10) T. Sakai et al. *Acta metal.* 1984, Vol.32, p.189-209.
11) H. Miura et al. *Phil. Mag.* 2007, Vol.87, p.4197-4209.
12) H. Miura et al. *Journal of the Japan Institute of Metals.* 1994, Vol.58, p.267-275.
13) M. Watanabe et al. *Journal of Japan Research Institute for Advanced Copper-base Materials and Technologies.* 2009, Vol.48, p.21-26.
14) L. Blaz et al. *Metal Sci.* 1983, Vol.17, p.609-616.
15) F. J. Humphreys et al. *RECRYSTALLIZATION and Related Annealing Phenomena. Second Edition, ELSEVIER*, 2004, p.1.
16) H. Miura et al. *Materials Science Forum. 2010*, Vol.654-656, p.1267-1270.
17) T. Sakai et al. *Journal of the Japan Institute of Metals.* 1993, Vol.57, p.1390-1396.
18) Iron and Steel Institute of Japan. *Recrystallization, Texture and Their Application to Structural Control.* 1999, p.106-115.